IMPROVED CONTROL OF SINGLE CYCLE PULSE GENERATION BY MOLECULAR MODULATION

A Dissertation

by

ANDREA MIHAELA BURZO

Submitted to the Office of Graduate Studies of
Texas A&M University
in partial fulfillment of the requirements for the degree of

DOCTOR OF PHILOSOPHY

December 2005

Major Subject: Physics

IMPROVED CONTROL OF SINGLE CYCLE PULSE GENERATION

BY MOLECULAR MODULATION

A Dissertation

by

ANDREA MIHAELA BURZO

Approved by:

Chair of Committee,	Alexei V. Sokolov
Committee Members,	Roland E. Allen
	George R. Welch
	Philip Hemmer
Head of Department,	Edward S. Fry

December 2005

Major Subject: Physics

ABSTRACT

Improved Control of Single Cycle Pulse Generation by Molecular Modulation.

(December 2005)

Andrea Mihaela Burzo, B.S., University of Bucharest;

M.S., Texas A&M University

Chair of Advisory Committee: Dr. A. V. Sokolov

Generation of reproducible attosecond (10^{-18}s) pulses is an exciting goal: in the same way as femtosecond pulses were used to make "movies" of the atomic motion in molecules, attosecond pulses could "uncover" the motion of electrons around nuclei. In this dissertation, we have suggested new ideas that will allow improving one scheme for obtaining such ultra-short pulses: the molecular modulation technique. In a theoretical proposal called Raman Additive technique, we have suggested a method that will allow (with a proper phase stabilization of generated sidebands) to obtain reproducible waveforms of arbitrary shape. An exciting range of possibilities could open up - not only for absolute phase control or sub-cycle shape control, but also for investigation of multiphoton ionization rates as a function of the sub-cycle shape. We have elaborated on the latter subject in another theoretical project, where we have exploited the unique feature of such ultrashort laser pulses, which is synchronization with molecular motion (rotational or vibrational), in order to investigate photoionization of molecules. From experimental point of view, a different construction of driving lasers than previously employed led to establishment of larger molecular coherences at higher operating pressure than in previous experiments. This resulted in simultaneous generation of rotational and vibrational sidebands with only two fields applied. In another experimental proposal using rotational transition in deuterium we have

iv

shown that employing a hollow waveguide instead of normal Raman cell improves the efficiency of the generation process. By optimizing gas pressure and waveguide geometry to compensate the dispersion, the method can be extended to efficiently generate Raman sidebands at a much lower energy of driving fields than previously employed. At the end, a very exciting possibility for controlling the molecular motion in a Raman driven system will be shown. Based on the interference effects (EIT-like) that take place inside of a molecule, selectivity of different degrees of freedom can be achieved (for example switching from rotational-vibrational motion to pure rotational).

To my dear family- my dad Emil, my brother Dan
and especially to my mother Virginia Burzo

ACKNOWLEDGMENTS

This is perhaps the easiest and the hardest chapter that I have to write. Even though it should be easy to simply name all the people that helped to get this work done, it is tough to thank them enough. I will try nonetheless...

I wish to express my gratitude to my advisor, Dr. A. V. Sokolov for giving me the chance of starting my new life as an experimentalist in one of the most exciting cutting edge research areas. Special thanks go to Dr. Igor Marienco, Miaochan Zhi, Jiahui Peng, for their support during this time; Dr. Alexey Chugreev, my work partner and friend for helping me with experiments in the lab; my committee members, for reading my thesis; and Dr. L. Keldish and Dr. Y. Rostovtsev for valuable discussions that have contributed to the success of this work. In addition, I would like to thank all my professors who have contributed to my formation as a physicist.

The joy I received from working on this thesis would have been meaningless without my relatives and friends. I would like to gratefully acknowledge the support of some very special individuals. They helped me immensely by giving me encouragement and friendship. They mirrored back my ideas so I heard them aloud, allowing me to further pursue them. I wish to thank Petr Anisimov for being a true friend and an extraordinary source of advice. There are many friends that I made as a graduate student whom I would like to thank for wonderful trips to the ocean, or simply hiking around College Station. Anatoly Svidzinsky, Anton Biryukov, Alexey Chugreev thank you for those moments.

Teri Gailey-Price, Randi Price thank you for being my family here. Teri, words cannot describe your thoughtful advice and constant support throughout the years that I spent here.

I feel a deep sense of gratitude for my family who taught me the things that

really matter in this life. The memory of my mother provides a persistent inspiration to my journey in life. I am grateful to my brother for rendering my life here better with many long emails and pictures from home.

Frede... I will always remember you.

TABLE OF CONTENTS

LIST OF TABLES

LIST OF FIGURES

xii

FIGURE   Page

FIGURE   Page

CHAPTER I

INTRODUCTION

A.   Methods for generation of attosecond laser pulses

Ever since the invention of laser in 1958 [1], the quest for shorter laser pulse durations opened the possibility to gain access to processes that occurred on a faster and faster time scale. This continuous search for attaining shorter, and at the same time, higher peak power laser pulses was achieved in small steps, with a starting point duration of just several hundreds of microseconds [2] by using a ruby laser. However, progress towards shorter pulse durations was not always made slowly. For example, just within one year from invention of ruby laser, a four order of magnitude decrease in time duration was reached through the invention of Q-switch [3]. Within next 5-10 years from this rapid decrease in pulse length, another four order of magnitude drop (to picosecond regime) was achieved by mode locking [4] and use of dye laser [5].

The basic idea of mode locking relies on locking of phases of different longitudinal modes of a resonator, in such a way that they interfere constructively, generating trains of discrete ultrashort laser pulses which are separated by the cavity round trip time. Mode locking can be employed to both continous wave (cw) and pulsed lasers. Two main techniques are used for mode locking: so called passive, and active mode locking, both of them being extensively studied in textbooks [6], [7], or in reviews such as [8]. In the passive method, one can place a saturable absorber such as a dye solution in the laser cavity in order to lock the relative phases of different modes. In the case of active mode locking, the locking is achieved by modulating the loss in the cavity with an acousto-optic device [6, 9, 10]. Using this method, pulse widths of

_____

The journal model is *Physical Review A.*

order of 30-150 ps can be achieved.

Further improvements in the mode locking techniques such as Kerr self-mode locking were developed [11], and soon dye lasers were replaced by solid state lasers, which benefit from longer period of operation compared to dye lasers, smaller size, and simpler construction. Titanium doped sapphire is currently the main solid state material for development of ultrashort laser pulses, due to a large bandwidth (approximately 220 nm in near IR), and a broad absorption centered around 490 nm, which corresponds to optimal pumping by argon-ion laser, or second harmonic of Nd:Yag laser [12].

The actual mechanism of Kerr self mode locking relies on the Kerr self-focusing effect - a mechanism that allows a nonlinear medium (crystal in the case of solid state lasers) to act as an intensity dependent lens, thus changing the intensity profile of the cavity mode. With the help of these techniques and chirped, ultra-broad band mirrors workers in this field [13], were able to reduce pulse length to about two cycles of oscillation.

Although significant, all the above improvements could not bring pulse duration below 5 femtoseconds.

New ideas for decreasing pulse duration even further have emerged at the beginning of 1990's, giving hope that the 5 femtosecond barrier could be broken soon. These ideas relied on Fourier synthesis and were proposed by different groups [14], [15]. The basic idea consists in generation of a large, equidistant spectral comb of frequencies with adjustable phases. The equivalent picture in time domain corresponds to trains of ultrashort pulses, with repetition rates given by the inverse separation frequency of generated comb. This idea of Fourier synthesis resembles the principle of laser mode locking described earlier in the chapter. Unlike the laser mode locking which is limited to about 10-100 THz frequency bandwidth, much larger bandwidth

needs to be generated in order to support attosecond (10^{18} s) pulses. To give a rough idea about needed bandwidth for generation of, for example 10 attoseconds long pulses, one will need to employ frequencies spanning over 15 10^3 THz, two orders of magnitude larger than in a mode locked laser.

Even though starting idea, namely Fourier synthesis was the same, two main approaches seemed to be distinguished clearly in achieving this goal. High harmonic generation HHG, and collinear Raman generation have proved in the past years to be effective methods for generation of attosecond laser pulses. Each method will be briefly discussed below.

In high harmonic generation, a laser pulse with frequency ω with intensity around 10^{14} W/cm^2 (comparable with field binding electrons in atoms) is focused into a jet of rare gas atoms. Light emission corresponding to odd harmonics at frequencies $n\omega$ are observed, with n being an odd integer. More than 200 such harmonics with almost equal amplitude could be generated, from a driving field wavelength 800 nm down to 20 nm [16].

The physical mechanism responsible for the vacuum ultraviolet VUV and soft X-ray emission is now well understood in terms of the "three step model", or Corkum' s model [17]. In the first step, the laser field modifies the Coulomb potential which binds the electron and atom, and as a consequence the electrons can tunnel through this barrier. In the second step, atomic electrons are accelerated by the strong electric field of the laser pulse. Due to oscillatory motion of the laser field, the electron can return to the parent atom and recombine (third step), thus emitting a high frequency photon (HHG process). Different electron trajectories corresponding to different kinetic energies result in different high harmonic frequencies.

The highest achievable photon energy is predicted by the Corkum' s model to

be:

$$E_{\max} = I_p + 3.2U_p, \tag{1.1}$$

where I_p represents the ionization potential of atom, and U_p is the ponderomotive energy which is described by the following equation:

$$U_p = \frac{e^2 E^2}{4m_e \omega^2}. \tag{1.2}$$

Here e, E, m_e, ω are the electron's charge, electric field amplitude, electron's mass and driving field laser frequency.

The second method for obtaining a broad frequency comb relies on generation of Raman sidebands. In stimulated Raman scattering (SRS), Stokes and anti-Stokes can be produced, resulting in an equidistant comb of frequencies separated by a frequency ν_0. Of particular pertinence is the work of Korn and colleagues, who have impulsively excited a vibrational mode of SF_6 and used the resulting time-varying refractive index to produce a sequence of compressed femtosecond pulses [18]. In another work, it was suggested [19] that phase locking of SRS components is feasible, and as a result trains of pulses separated by $1/\nu_0$ can be obtained. Harris and Sokolov [20] and [21] used the idea of molecular ensemble at maximum coherence to generate a wide spectrum consisting in equidistant, mutually coherent Raman sidebands.

The new scheme called molecular modulation differs from the standard SRS where only one field is applied. In addition, a low pressure gas is needed (lower than atmospheric pressure), as opposed to high pressure regimes exceeding few atmospheres in traditional SRS. The key idea of this technique is that in order to generate such broad spectrum of frequencies components (hence very short pulse in time domain), a large modulation index and/or a high modulation frequency is required.In order to achieve this modulation of the index of refraction with a very high frequency, a

coherent superposition between the ground state and the first excited vibrational state is created by driving (adiabatically) the Raman (dipole-forbidden) transition slightly off resonance. These states can be coupled through the intermediate electronic states far away detuned from the two lowest states. The coupling between two driven states is achieved by a pair of driving lasers of sufficient intensity such that the product of their Rabi frequencies exceeds the product of the detuning from the electronic states and the detuning from the Raman transition. These two fields drive an ensemble of molecules either in phase, or out of phase with their beat note frequency, depending on the sign of the small Raman detuning. When they are stretched apart, their index of refraction will increase (resembling more two independent atoms), while in the case when they are compressed index of refraction will decrease. This periodic change in the index of refraction results in the modulation of driving field frequencies, and hence generation of a broad spectrum of frequencies [22]. Total bandwidth generated through this method extends from infrared, visible into UV region i.e. spanning over more than 50,000 cm^{-1}.

The importance of preparing the ensemble at maximum coherence can be understood by looking at the propagation equation for the generated fields. The wave equation can be simplified by considering that the beam propagates in one direction and that the envelope of the electric field varies slowly in time and space compared to the period of optical cycle and wavelength of light (SVEA). For the case of negligible diffraction, the propagation equation for the qth sideband, in a time frame moving with the speed of light c is [22]:

$$\frac{\partial E_q}{\partial z} = -j\eta\hbar\omega_q N(a_q\rho_{aa}E_q + d_q\rho_{bb}E_q + b_q^*\rho_{ab}E_{q-M} + b_{q+M}\rho_{ab}^*E_{q+M}). \qquad (1.3)$$

The coefficient η represents the impedance of the free space $\eta = \mu/\epsilon_0$, with N representing the number of molecules per volume. Coefficients a_q, b_q, c_q, and d_q are
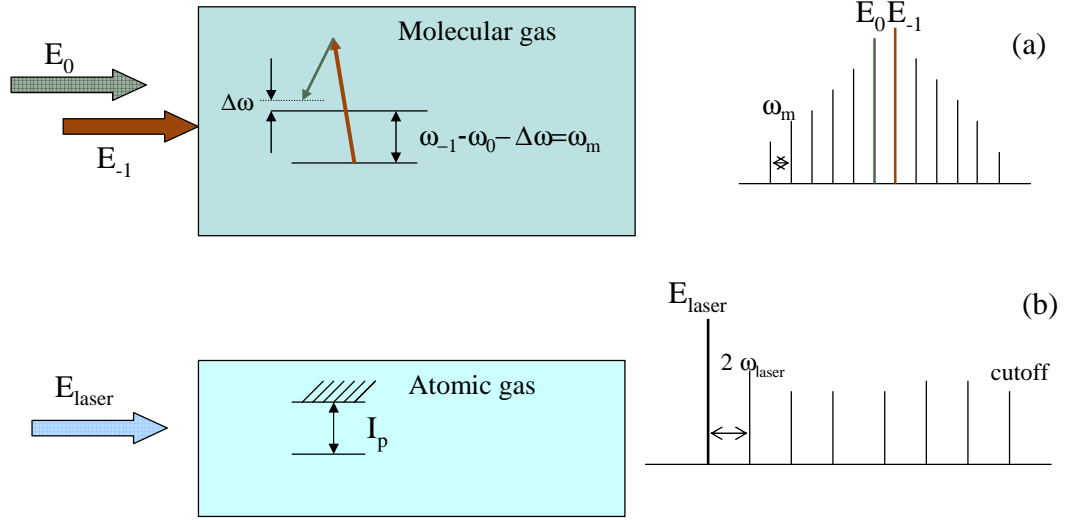
Fig. 1. Schematic of molecular modulation technique (a) and HHG (b). Generated frequency comb in (a) is spaced by approximately frequency difference of driving fields, while in (b) comb is spaced by twice the frequency of initial field.

of the same order, and with a coherence ρ_{ab} approaching its maximum value of 0.5, the driving terms in Eq. 1.3 are almost as big as the dispersive terms. This is why the coherence of the system is crucial in this technique.

Furthermore, it turns out that pulse generation and compression can occur in the same cell, with a pulse duration as short as 2 femtoseconds [22] .

A comparison of the two main methods for generation of attosecond pulses is presented in Fig. 1. By driving a Raman transition with two input fields, a wide comb of frequencies spaced by roughly the frequency difference of driving fields is generated. Figure (b) shows the schematics of HHG. An intense driving field is focused into a cell containing an atomic gas and high harmonics separated by twice the frequency of input field are generated at the cell's output. A cutoff frequency given by Eq. 1.1 limits the number of harmonics generated.

Both methods are capable of producing spectra that extend into deep UV. In the

molecular modulation technique, most generated frequencies lie in the visible region, thus making the adjustment of phases easier. However, higher carrier frequencies are produced in HHG method, but the efficiency of this process is very low (10^{-5}) as compared to molecular modulation technique where a 100% efficiency is possible [23].

B.   Pulse measurement

It is a very difficult task to characterize pulse durations of order of 10^{-18} s. All electronic devices fail to respond within this extremely short timescale. As an example, oscilloscopes and photo detectors can offer at best a resolution of 10 ps. Moreover, handling high harmonics in VUV and soft X ray region where there is a lack of necessary optics renders the characterization of pulse duration even harder.

The only fast enough option available for measurement remains then the pulse itself. Correlation methods rely on the measurement of convolution of the pulse to be measured either with itself (auto-correlation) or with a known pulse. Provided that there is enough intensity in the pulses to be measured, multiphoton ionization of a gas can be used [24]. By driving fundamental vibrational transition in deuterium, the authors demonstrated that all sidebands are generated mutually coherent (i.e. by controlling the relative phases of three sidebands, they showed that intensity of fourth sideband is a sinusoidal function of this phase). In addition, pulse characterization was realized indirectly by measurements of photo-ionization of xenon atoms, whose ionization is very sensitive to the pulse shape. Results showed that trains of 2 femtosecond pulses could be generated.

C. Dissertation organization

This dissertation is devoted to finding new methods, both theoretically and experimentally, that will result in improvements of the molecular modulation technique.

Generating few cycle pulses with reproducible evolution of electric fields requires achieving a full control over all parameters (temporal shape, phase, energy) of pulses. This control can be optimized by maximizing the number of frequency components which will allow synthesis of an arbitrary waveform.

A theoretical analysis will be carried out in Chapter II in order to investigate if it is possible to keep a large bandwidth (more than three octaves), while increasing the number of equidistant components. This theoretical work will be an extension of the Raman modulation technique, and its essential idea is based on applying more input fields to the molecular ensemble, as noted recently by other authors [25]. As a result, the total number of sidebands will be increased, simply because each individual applied field will produce sidebands that will add up (hence Raman additive technique name). Therefore, the spacing between adjacent sidebands could be in principle reduced (with proper conditions) to a fraction of the modulation frequency. A promising and attractive feature of this technique will be that the generated comb reaches zero frequency, as a consequence allowing for phase control of multiphoton ionization. As pointed out in previous work, photo ionization of molecules by intense laser pulses which consist only of few optical cycles of oscillations is very sensitive to the shape of the pulse itself [26, 27, 28, 29]. Since all effects generated by means of such ultrashort pulses are governed by the time dependence of the electric field rather then the envelope, absolute phase (or phase of the carrier wave at maximum of the envelope) becomes a crucial parameter to control. In the new proposed method (Raman additive technique), this control of absolute phase (through proper phase

stabilization of the generated sidebands) can be achieved.

It was shown previously [22, 30] that the molecular modulation technique allows the generation of not single (isolated) ultrashort pulses, but rather a train of such pulses with a very high repetition rate (molecular period of order of 10-100 fs). This unique feature of the generated pulses could be exploited in order to study molecular and electronics dynamics. A particular interest is studying photoionization of molecules by strong ultrashort laser pulses. Molecules exhibit a far richer range of phenomena in a strong field than do atoms, which means that strong field physics in molecules is less understood than in the atoms.

Chapter III will contain a theoretical study of ionization rates in a molecular gas which is subjected to this ultrashort train of pulses. The essential idea of this project is to generate a train of pulses in a molecular medium such as H_2 or D_2, which is synchronized with a molecular (vibrational or rotational) motion, and then using a delay line send these pulses into a second cell filled with same molecular gas. By changing the delay of the arrival of the pulses with respect to the molecular motion in the second cell, one can achieve different ionization rates. Numerical simulation results of this process will be provided, and future experimental results will be compared with theoretical ones.

The experimental setup necessary for demonstration of Raman modulation technique relies on construction of two tunable injection seeded pulsed Ti: Sapphire lasers that will allow driving of the different Raman transitions in molecules such as deuterium or hydrogen.

In Chapter IV, two different types of construction of such lasers will be shown : a novel short 6 cm linear cavity pumped from two sides by the second harmonic of a Nd:YAG laser, at a repetition rate of 10 Hz, and a more traditional ring cavity configuration with a length of 12 cm. Both lasers will be injection seeded by two

tunable laser diodes. Injection seeding is a well known method of controlling the properties of lasers, namely the spectral output, by using a low power output laser with a narrow spectral bandwidth-referred to as seed laser. Output power of seed laser is injected into of oscillator and serves as a seed from which the pulsed laser output grows. In competition, naturally occurring pulses begin from the zero point energy of the laser resonator or from spontaneous emission. If the injected seed is large enough, the pulse growing from the injected seed will deplete the gain of the laser material before the natural pulses become large. If so, the laser output will mimic the properties of the seed rather than the properties of the free running laser.

The construction of the new lasers is different than the ones used in the previous experimental setup [22]. By keeping the cavity length short to a minimum, and by maintaining pulse energy, shorter pulses will be achieved. Specifically, large atomic (or molecular) coherence can be established in a transient regime by a combination of narrow-line width (bandwidth-limited) laser pulses with duration shorter than the dephasing time [31]. Since the dephasing of a dipole-forbidden transition is often limited by the collisional decoherence rate (which in turn is proportional to the gas pressure), shorter pulses will allow us to work with larger ensemble densities, provided that the pulse energy is sufficiently high. Furthermore, the intensity of the two driving fields in molecular cell can be increased without a tight focusing, which will make the generation process less efficient. In addition to the construction of driving lasers, a vacuum setup will be build that will allow the connection of a 1 m long Raman cell filled with deuterium at pressures from 1 Torr to atmospheric pressure.

For generation of a broad spectrum of frequencies, several requirements have to be met. Among them, a high enough intensity of driving fields of order of several GW/cm^2 must be achieved. A good quality of transverse beam profiles of driving fields is also important for an efficient spatial overlap. In addition, the interaction

length has to be increased, since the generation process is proportional to the product of density length.

In Chapter V we describe an experimental method which will allow maintaining higher intensity of driving fields over a long interaction length, improving the spatial beam overlap, and reducing the required laser power. By using a hollow fiber filled with deuterium, the efficiency of Raman generation will be shown to be increased . This method can be extended to efficiently generate Raman sidebands with frequency spacing equal to vibrational frequency in other molecular gases. Possible improvement of phase matching condition by compensating the gas dispersion by the waveguide dispersion will be analyzed also.

While the previously proposed idea (use of hollow fiber) will allow a more efficient Raman generation, an increase in the spectral density of generated comb is desired for a better control over the electric field under the envelope, as mentioned before. Our theoretically proposed Raman additive technique can be implemented by applying two independent tunable lasers, together with additional fields obtained by harmonic generation and frequency mixing. A related idea of obtaining a multiplicative increase in the number of the sidebands has been investigated theoretically [23] and very recently experimentally [32]. That technique was based on the use of modulators in series that allowed generation of a large number of non-equidistant sidebands in a cell filled with different species.

The experiment that we describe in Chapter VI is in essence similar to the one described in Ref. [24]. In this experiment we have observed simultaneous rotational and vibrational Raman generation in deuterium gas, with only two laser pulses applied at the input of the molecular cell. Only the fundamental vibrational transition is driven strongly in this experiment. However, in addition to efficient vibrational Raman generation we observe generation of a large number of rotational sidebands.

This increase in number of sidebands (from 17 vibrational sidebands to more than 100 vibrational - rotational sidebands) could be used for a better control over the electric field as function of time.

Next Chapter VII will analyze at last a theoretical proposal that extends the electromagnetically induced transparency EIT ideas such as interference effects to control the molecular motion in a Raman gas medium. EIT has been demonstrated so far mostly in atoms, and only very recent experiments have shown that EIT is possible in a molecular system [33]. To our knowledge, no work has been done to study interference effects in a molecular Raman system. These interference effects do not result here in change of transmission of fields as in the standard EIT scheme, because our system does not exhibit absorption, but rather result in control of molecular motion for example switching from vibrational-rotational motion to pure rotational. We are planning to experimentally implement this scheme in future work.

CHAPTER II

RAMAN ADDITIVE TECHNIQUE

A. Introduction: frequency comb spaced by a fraction of the modulation frequency

With pulse widths approaching attosecond limits, for an accurate optical control of a process, it is necessary that the electric field of ultrashort laser is shaped as precisely as possible. Therefore, the goal will be not only to achieve a large bandwidth, but also a large number of frequency components to allow synthesis of an arbitrary waveform.

This theoretical work will be an extension of the Raman modulation technique, and its essential idea is based on applying more input fields to the molecular ensemble, as noted recently by other authors [25]. As a result, the total number of sidebands will be increased, simply because each individual applied field will produce sidebands that will add up (hence Raman additive technique name). Therefore, the spacing between adjacent sidebands could be in principle reduced (with proper conditions) to a fraction of the modulation frequency. Although this method works in principle for an arbitrary spacing between generated frequencies, in practice it will be restricted to a fraction of 1/4 or 1/9 of the modulation frequency, due to a limited choice of the available laser wavelengths and harmonic generation crystals necessary in this approach.

A promising and attractive feature of this technique will be that the generated comb reaches zero frequency, and as a consequence allowing for absolute phase control- provided that proper phase stabilization of generated sidebands is achieved.

To understand the meaning of the phase in the evolution of ultrashort laser pulses, let us describe the electric field of the laser pulse by the product of the pulse envelope $E_0(t)$ and carrier:

$$E\left(t\right) = E_o(t)\cos(\omega t + \varphi) \tag{2.1}$$

By convention, a pulse where the field is at maximum at $t = 0$ (i. e. absolute phase $\varphi = 0$) is called a "cosine" type of pulse, whereas zero field amplitude at time $t = 0$ corresponds to a "sine" pulse, with a $\frac{\pi}{2}$ phase. As pointed out in previous work, photo ionization of molecules by intense laser pulses is influenced by the time dependence of the electric field (and not the envelope), thus making the control of so called absolute phase a very important task [26, 27, 28, 29].

A related idea of obtaining a multiplicative increase in the number of the sidebands has been investigated theoretically [23] and very recently experimentally [32]. That technique was based on the use of modulators in series that allowed generation of a large number of non-equidistant sidebands.

B. Theory

Let us now begin by describing the system as follows: a coherent superposition between the ground state and the first excited molecular vibrational state is created by driving (adiabatically) the Raman (dipole-forbidden) transition slightly off resonance. These states can be coupled through the intermediate electronic states $|i\rangle$ far away detuned from the two lowest states. The coupling between the states $|a\rangle$ and $|b\rangle$ is achieved by a pair of driving lasers of sufficient intensity such that the product of their Rabi frequencies exceeds the product of the detuning $\delta\omega$ from the electronic states and the detuning from the Raman transition $\Delta\omega$ (Fig. 2 left).

The crucial point in this technique is the choice of the input fields. We start by considering a comb of frequencies, (numbered by a positive integer subscript q), for which the electric field (space and time dependent) is described in terms of the
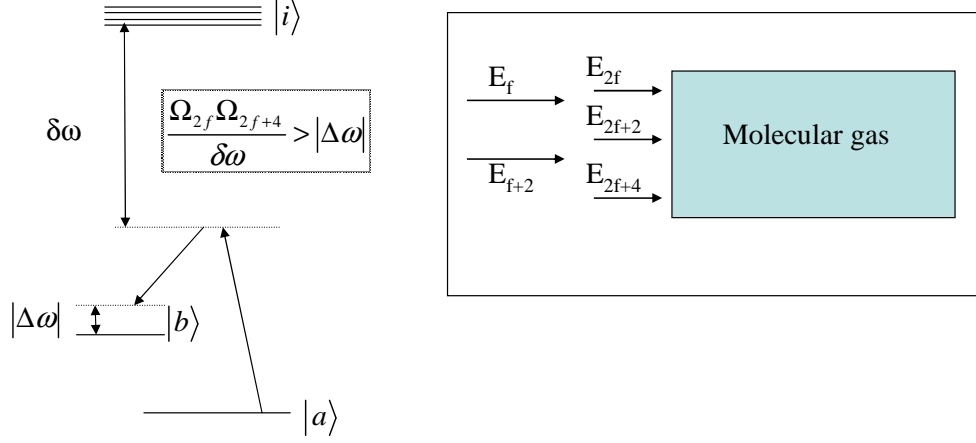
Fig. 2. Energy level schematic (left) for establishing coherence ρ_{ab} in a molecular system. $|a\rangle$ is the ground state and $|b\rangle$ is the excited molecular state. Here Ω_{2f} and Ω_{2f+4} are the Rabi frequencies for the particular case when $M = 4$. The Raman detuning $\Delta\omega$ is set by the driving laser frequencies. The detuning from the electronic states $|\imath\rangle$ is comparable to the applied laser frequencies. Right figure shows applied input fields for the case when M=4. The fields are numbered by an integer subscript which corresponds to their frequencies measured in units of $\frac{\omega_m}{4}$, where ω_m represents the frequency difference of the applied second harmonics fields. Here E_f is the electric field envelope at the applied fundamental frequency $\omega_f = \frac{f\omega_m}{4}$, and $f = 4n \pm 1$, with n a positive integer.

complex envelope quantity $\hat{E}_q(z,t)$:

$$\hat{E}_q(z,t) = \ Re\left\{E_q\left(z,t\right)\exp\left[j\left(\omega_q t - k_q t\right)\right]\right\}, \tag{2.2}$$

where $\omega_q = \frac{q\omega_m}{M}$ and $k_q = \frac{\omega_q}{c}$.

We denote by ω_m/M the separation frequency between generated sidebands, where M is a multiplicity constant (which can be 4 or 9). We consider a specific example where the separation frequency between the generated sidebands is decreased by a factor of 4 (i.e $M = 4$). We start by taking two fundamental fields separated by

one half of the molecular frequency [34]:

$$\omega_f = \frac{f\omega_m}{4}, \qquad \omega_{f+2} = \frac{(f+2)\omega_m}{4}, \tag{2.3}$$

then generating their sum frequency and their second harmonics:

$$\omega_{2f+2} = \frac{(2f+2)\omega_m}{4}, \qquad \omega_{2f} = \frac{2f\omega_m}{4}, \qquad \omega_{2f+4} = \frac{(2f+4)\omega_m}{4}. \tag{2.4}$$

Here f should be restricted to $f = 4n \pm 1$, where n is a positive integer. This condition is necessary in order to produce interleaving sidebands at intervals separated by exactly $\omega_m/M = \omega_m/4$, where the frequency ω_m is equal to the second harmonic frequency separation.

Fig. 2 (right) illustrates a typical case of the five input fields for $M = 4$ with the two fundamental fields being labeled by E_f and E_{f+2}. The idea can be extended to the case when the desired frequency spacing is one ninth of the modulation frequency ω_m ($M = 9$) [34].

We proceed further to analyze (in the dipole approximation), the Hamiltonian that describes the interaction of the field with a molecule. It can be shown that this Hamiltonian is reduced to an effective two-by-two Hamiltonian, provided that the derivatives of the probability amplitudes of the upper states $|i\rangle$ are small compared to the detunings from these states [20]:

$$H_{eff} = -\frac{\hbar}{2}\begin{bmatrix} \sum_q a_q \left|E_q\right|^2 & \sum_q b_q E_q E_{q-M}^* \\ \sum_q b_{q+M}^* E_q E_{q+M}^* & \sum_q d_q \left|E_q\right|^2 - 2\Delta\omega \end{bmatrix} = -\frac{\hbar}{2}\begin{bmatrix} A & B \\ B^* & D - 2\Delta\omega \end{bmatrix}. \tag{2.5}$$

The constants a_q and d_q determine the dispersion, while b_q describes the coupling between the two states $|a\rangle$ and $|b\rangle$. If the matrix elements from states $|a\rangle$ and $|b\rangle$ to (an arbitrary number of states) $|i\rangle$ are denoted by μ_{ai} and μ_{bi}, then the coefficients a_q, b_q and d_q read [21, 30, 35, 36, 37].

$$a_q = \frac{1}{2}\sum_i \left[\frac{|\mu_{ai}|^2}{(\omega_i - \omega_a) - \omega_q} + \frac{|\mu_{ai}|^2}{(\omega_i - \omega_a) + \omega_q} \right],$$

$$b_q = \frac{1}{2}\sum_i \left[\frac{\mu_{ai}\mu_{bi}^*}{(\omega_i - \omega_a) - \omega_q} + \frac{\mu_{ai}\mu_{bi}^*}{(\omega_i - \omega_b) + \omega_q} \right],$$

$$d_q = \frac{1}{2}\sum_i \left[\frac{|\mu_{bi}|^2}{(\omega_i - \omega_b) - \omega_q} + \frac{|\mu_{bi}|^2}{(\omega_i - \omega_b) + \omega_q} \right]. \tag{2.6}$$

Here the two photon detuning $\Delta\omega$ represents the difference between the Raman transition frequency and the modulation frequency. The next step is to derive a propagation equation for the generated fields. In this context, the wave equation can be simplified by considering that the beam propagates in one direction and that the envelope of the electric field varies slowly in time and space compared to the period of optical cycle and wavelength of light (SVEA). For the case of negligible diffraction, the propagation equation for the qth sideband, in a time frame moving with the speed of light c is

$$\frac{\partial E_q}{\partial z} = -j\eta\hbar\omega_q N \left(a_q \rho_{aa} E_q + d_q \rho_{bb} E_q + b_q^* \rho_{ab} E_{q-M} + b_{q+M} \rho_{ab}^* E_{q+M} \right). \tag{2.7}$$

The coefficient η represents the impedance of the free space $\eta = \mu/\epsilon_0$, with N representing the number of molecules per volume. It is evident that for efficient generation to occur, the magnitude of the molecular coherence should approach 0.5. This is why the coherence of the system is crucial in this technique.

An important issue here is taking in account the additional terms in the propagation equation that arise due to the 'reflection of zero frequency'. This is a parametric two photon down conversion process, which sometimes is said to result in 'negative frequency' sideband generation. The negative frequencies can be thought of as reflecting (or bouncing) DC, with a phase shift of 180 degrees to combine with their positive counterparts. At the end of simulation, conservation of the number of photons is

checked. The total number of photons may change slightly, due to the 'reflection of DC' parametric conversion process.

In the absence of dispersion, one can derive an approximate solution to the propagation equation, assuming a small modulation bandwidth. Let us take as an example the case for which the multiplicity constant $M = 4$ and $f = 9$. The fundamental fields are applied at sidebands $q = 9, 11$, their sum at $q = 20$, and the second harmonics at $q = 18, 22$. For this particular case, in the absence of dispersion, and in the limit of small modulation bandwidth, the solution for the electric field at each individual sideband is given by [34]:

$$
\begin{aligned}
\tilde{E}_{4n}(z) &= E_{20}(0)\exp\left[j\left(\varphi\left(0\right) - \frac{\pi}{2}\right)(n-5)\right]J_{n-5}\left(\gamma_{2f}z\right), \\
\tilde{E}_{4n-1}(z) &= E_{11}(0)\exp\left[j\left(\varphi\left(0\right) - \frac{\pi}{2}\right)(n-3)\right]J_{n-3}\left(\gamma_{f}z\right), \\
\tilde{E}_{4n-2}(z) &= E_{18}(0)\exp\left[j\left(\varphi\left(0\right) - \frac{\pi}{2}\right)(n-5)\right]J_{n-5}\left(\gamma_{2f}z\right) + \\
&\quad\quad E_{22}(0)\exp\left[j\left(\varphi\left(0\right) - \frac{\pi}{2}\right)(n-6)\right]J_{n-6}\left(\gamma_{2f}z\right), \\
\tilde{E}_{4n-3}(z) &= E_{9}(0)\exp\left[j\left(\varphi\left(0\right) - \frac{\pi}{2}\right)(n-3)\right]J_{n-3}\left(\gamma_{f}z\right), \quad\quad\quad (2.8)
\end{aligned}
$$

where n is a positive integer. Here $\tilde{E}_q = E_q \cdot exp(j\beta_q z)$, $\beta_q = \eta\hbar\omega_q N a_q$, $\gamma_f = \frac{b_f}{a_f}\beta_f \sin\left[\theta\left(0\right)\right]$, $\gamma_{2f} = \frac{b_{2f}}{a_{2f}}\beta_{2f} \sin\left[\theta\left(0\right)\right]$, where subscript f corresponds to the fundamental frequencies. We define $\tan\theta = \frac{2|B|}{2\Delta\omega - D + A}$ and $\varphi\left(0\right) = \arg\left[E_{22}(0)E_{18}^{*}(0)\right]$. In our case, for systems with large detunings, the angle θ becomes approximately equal to $\theta \cong \tan^{-1}\left(\frac{|B|}{\Delta\omega}\right)$. This solution for the electric field of generated sidebands satisfies both propagation and density matrix equations, subjected to the appropriate boundary conditions.

C.   Numerical simulation results

We model this process numerically for molecular hydrogen. The modulation frequency is $\omega_m = 4160$ cm^{-1}. We take the density of molecular hydrogen to be $N = 2.69 \cdot 10^{19}$ molecules/cm^3, a total cell length of 6.8 cm, and retain sixty sidebands between $q = 1$ and $q = 60$. The constants a_q, d_q, b_q include all the contributions from allowed vibrational transitions in Lyman and Werner bands. We choose a two-photon detuning $\Delta\omega = -0.5$ GHz. In solving the propagation equation for the q'th sideband we employ a forth order Runge-Kutta method, integrating it in space from $z = 0$ to the total length of the cell. We emphasize that in solving the propagation equation we do not make any assumptions about dispersion and bandwidth.

For comparison, we model this process first with two input fields that are applied at $q = 22$, and $q = 18$ with intensities of $8 \cdot 10^{10}$ W/cm^2. Fig. 3 shows spectral and temporal evolution for the case of two applied fields, at the input of the cell (top), in the middle of the cell, and at the output of the cell (bottom) [34]. After the phases of these sidebands are made equal, they synthesize a short train of single-cycle pulses, with a repetition rate equal to the molecular frequency. The same parameters (density, two-photon detuning, intensities of driving fields) are kept for the case of more input fields. This time the fundamental fields are applied at $q = 9$ (1068 nm), $q = 11$ (874 nm), their sum at $q = 20$ (480 nm) and their second harmonics at $q = 18$ (534 nm), and $q = 22$ (437 nm) respectively. In this simulation we take all the phases of the input fields equal to zero. We choose the intensities of the fundamental fields, their sum and their second harmonics in such a way that the generated comb of frequencies is as even as possible in amplitude. We believe that our choice of these intensities represents the optimum condition that is set by an interplay between the generation process and dispersion in such a wide comb.
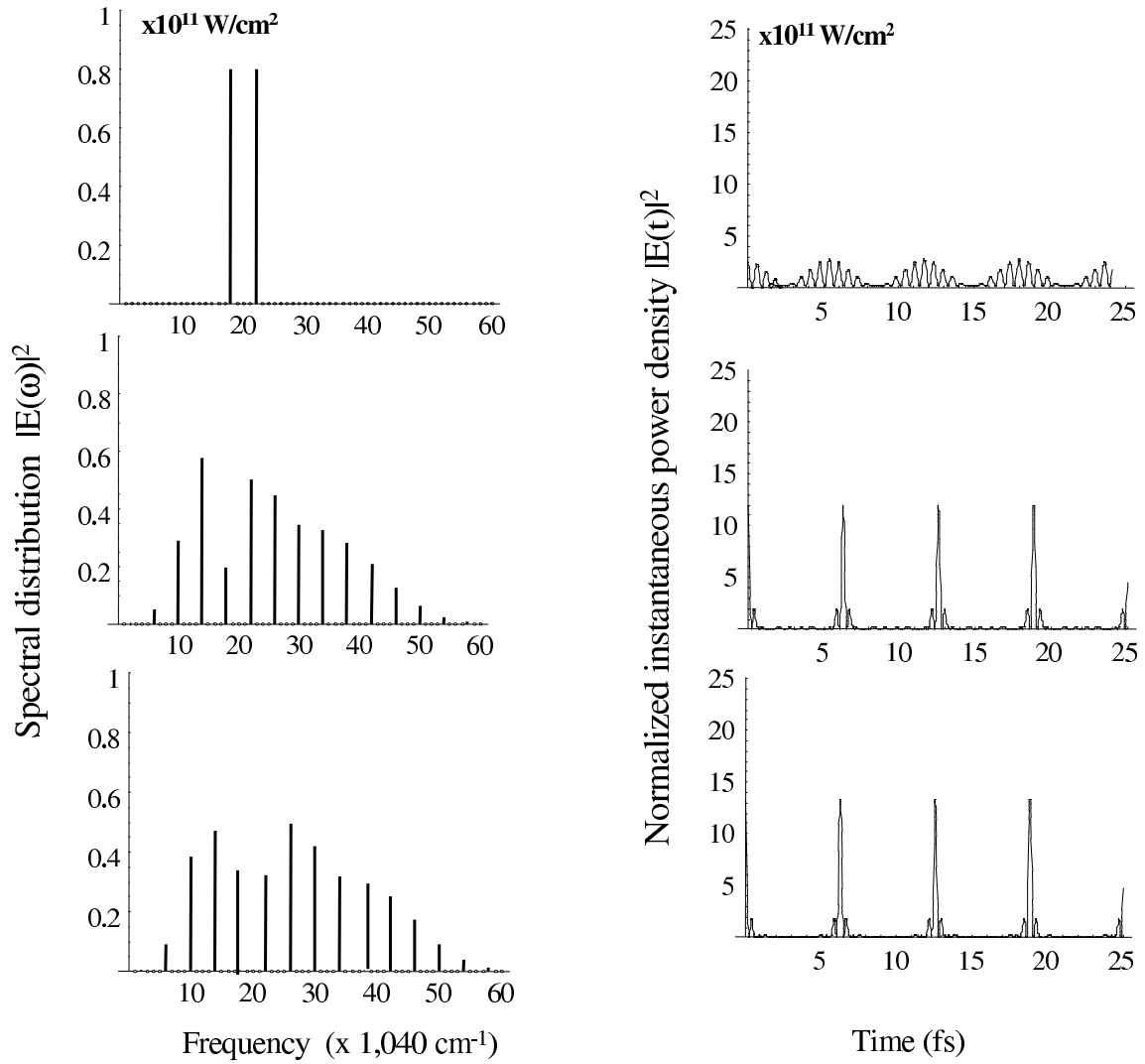
Fig. 3. Frequency spectrum (left) and instantaneous power density versus time (right) after phase correction in H_2 at 1 atm pressure with two input fields. The fields are shown at the input of the cell (top), in the middle of the cell, and at the output of the cell (bottom). This figure is similar to figure 7 from reference [22], which considered sideband generation in D_2.
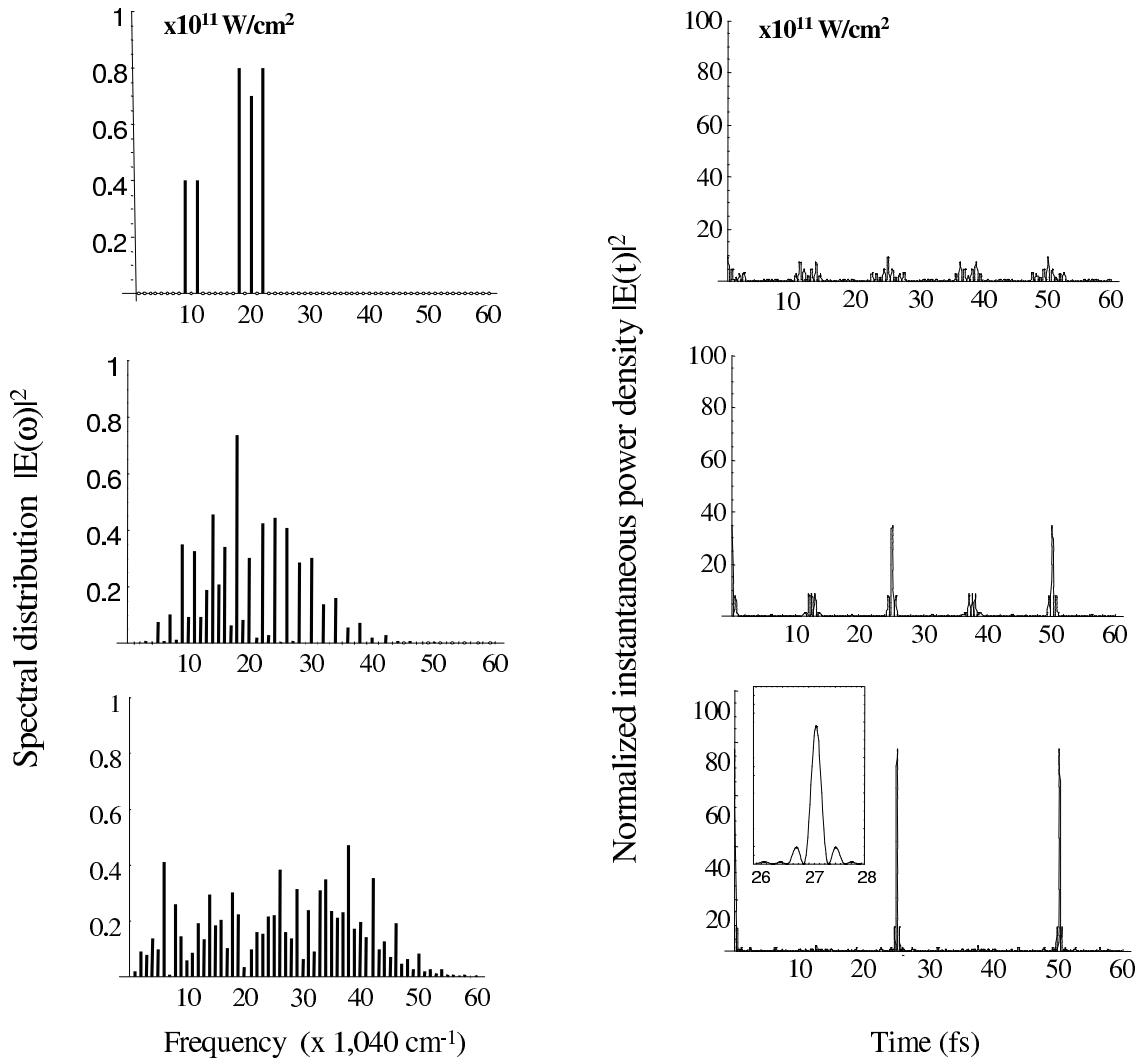
Fig. 4. Frequency spectrum (left) and instantaneous power density versus time (right) after phase correction in H_2 at 1 atm pressure with five input fields. The fields are shown at the input of the cell (top), in the middle of the cell, and at the output of the cell (bottom). The insert gives $|E(t)|^2$ on a finer time scale, showing an individual single-cycle pulse with a subfemtosecond duration.

22
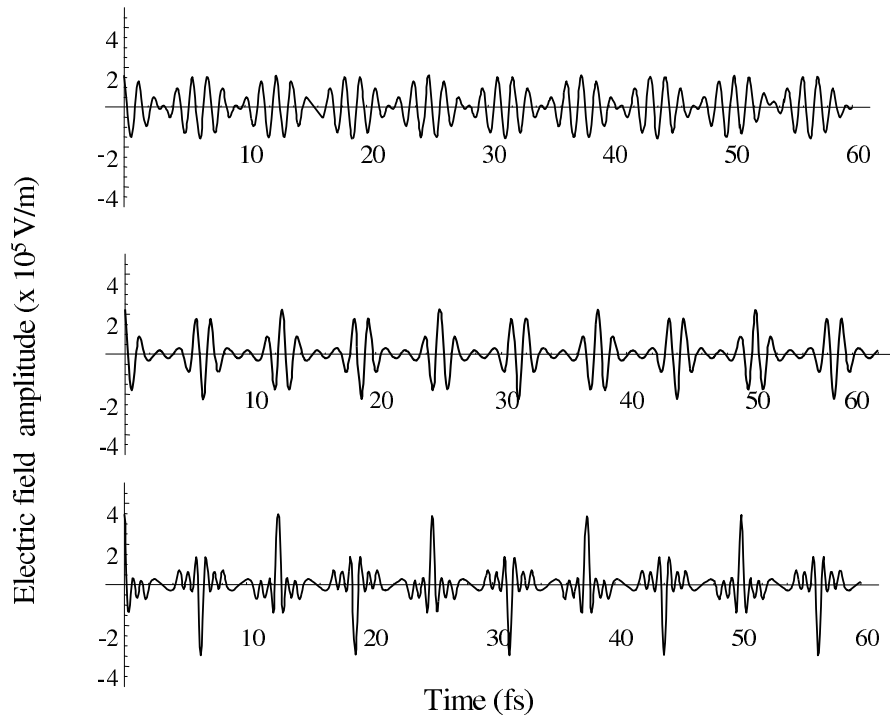
Fig. 5. Electric field obtained by old technique after adjusting the phase of the generated sidebands to zero. The waveforms correspond to different propagation distances inside the cell (input of the cell (top), in the middle of the cell, and at the output of the cell (bottom).

Fig. 4 shows the spectral (left) and temporal (right) evolution as a function of the distance for the case of more input fields [34]. In Fig. 4 (right) the vertical axis shows an increase in the intensity of about four times, while the horizontal axis represents a train of pulses spaced by an integer number (4) of the molecular periods.

In the present simulation, we allow for arbitrary phases of the generated sidebands, but assume that they are adjusted afterward by a spectral modification apparatus [38, 39, 40] and made equal to zero.

The waveforms synthesized by the individual sidebands after spectral adjustment,
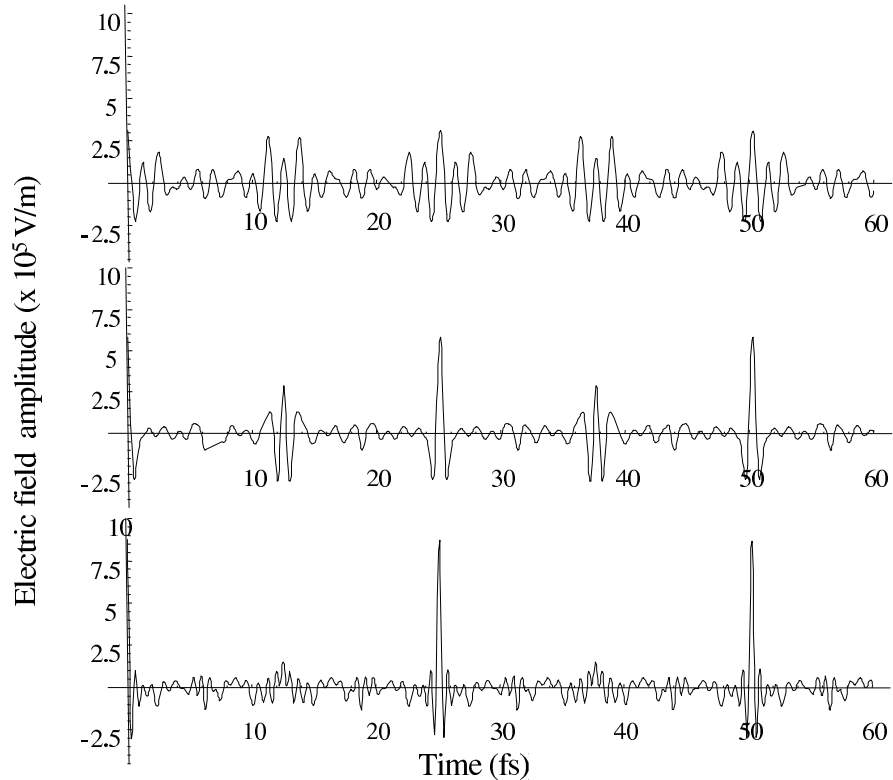
Fig. 6. Electric field obtained by additive technique after adjusting the phase of the generated sidebands to zero. The waveforms correspond to different propagation distances inside the cell (input of the cell (top), in the middle of the cell, and at the output of the cell (bottom).

are shown for comparison in Figs. 5 (old method) and 6 (new method). The major difference resides in the fact that, in the old method, the absolute phases of pulses within same train where different, whereas in the additive method, there is only one absolute phase for all pulses within same train. The explanation for this effect comes from the fact that in the additive technique, laser frequencies are multiples of their frequency difference.

To understand this, let us analyze what happens with the phase of the total
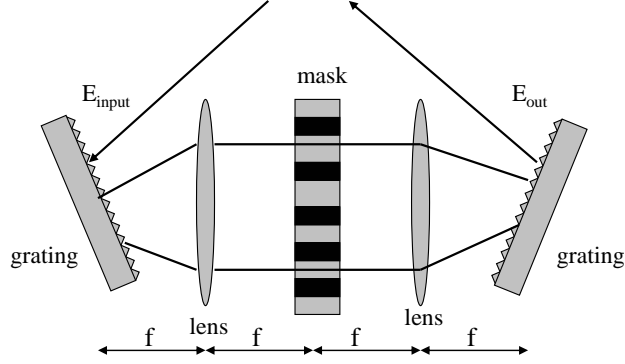
Fig. 7. Typical pulse shaping setup.

electric field as it propagates into cell. Recall that the total electric field is given by

$$E_q\left(t\right) = \text{Re} \sum_q \left|E_q(z)\right| e^{j\alpha} e^{j\omega_q t}, \tag{2.9}$$

where α represents a random phase, and $\omega_q = \omega_0 + q\omega_m$ [22]. As it propagates into the cell, this phase will change to $\alpha + j\beta q$, where β is an aquired phase during propagation. Then, Eq.(2.9) reads:

$$E_q\left(t\right) = \text{Re} \left(\sum_q \left|E_q\left(z\right)\right| e^{j(\alpha + q\beta)} e^{j(\omega_o + q\omega_m)t} \right). \tag{2.10}$$

By proper choosing the initial time, one can eliminate the additional phase β

$$E_q\left(t\right) = \text{Re} \left(\sum_q \left|E_q\left(z\right)\right| e^{j\alpha} e^{j\omega_o t + jq\omega_m(t-t_i)} \right). \tag{2.11}$$

One can see that in the case of Raman additive technique, input laser frequencies are integer multiple of their frequency difference (i.e. multiple of modulation frequency ω_m), and therefore no change of absolute phase of the total electric field occurs. However, this phase will change from shot to shot due to the change of the relative phase of the two fundamental fields.

Among applications of this technique one can list pulse shaping, waveform syn-
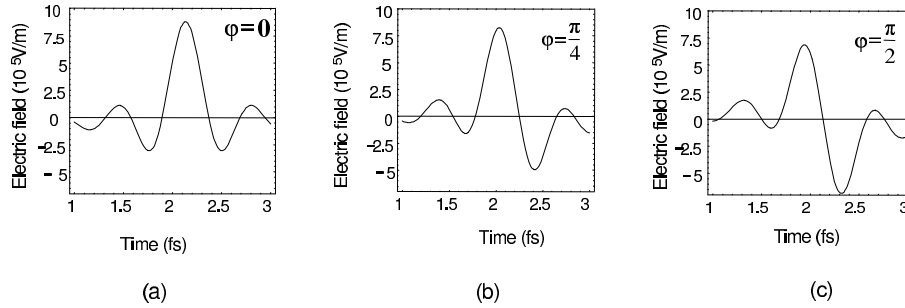
Fig. 8. Electric field obtained after adjusting all the phases of the generated sidebands to zero (a), $\frac{\pi}{4}$ (b) and $\frac{\pi}{2}$ (c).

thesis, or multiphoton ionization.

Using pulse shaping techniques, one can engineer subfemtosecond pulses into complex optical signals according to specifications. Many techniques have been developed that allow generation of such complicated optical waveforms. Their range of applications is quite large today, ranging from chirped pulse amplification [41] , coherent control in atomic processes [42], nonlinear optical processes in semiconductors [43], and chemical reactions [44].

A typical pulse shaping setup is shown in Fig. 7. The incident pulse is separated into its different frequencies components by diffraction gratings. With the aid of a telescope formed by a pair of lenses, and a programmable spatial light modulator SLM (which can be a liquid crystal or mask), the amplitude and phase of different components are adjusted accordingly. All the frequencies components are then recombined into a shaped pulse which is determined by the Fourier transform of the amplitude and phase imposed by the SLM [45, 46]. Commercially available liquid crystal spatial light modulator allow already independent control of both phase and /or amplitude of 1000 pixels, improving the possibility of precise shaping of electric field.
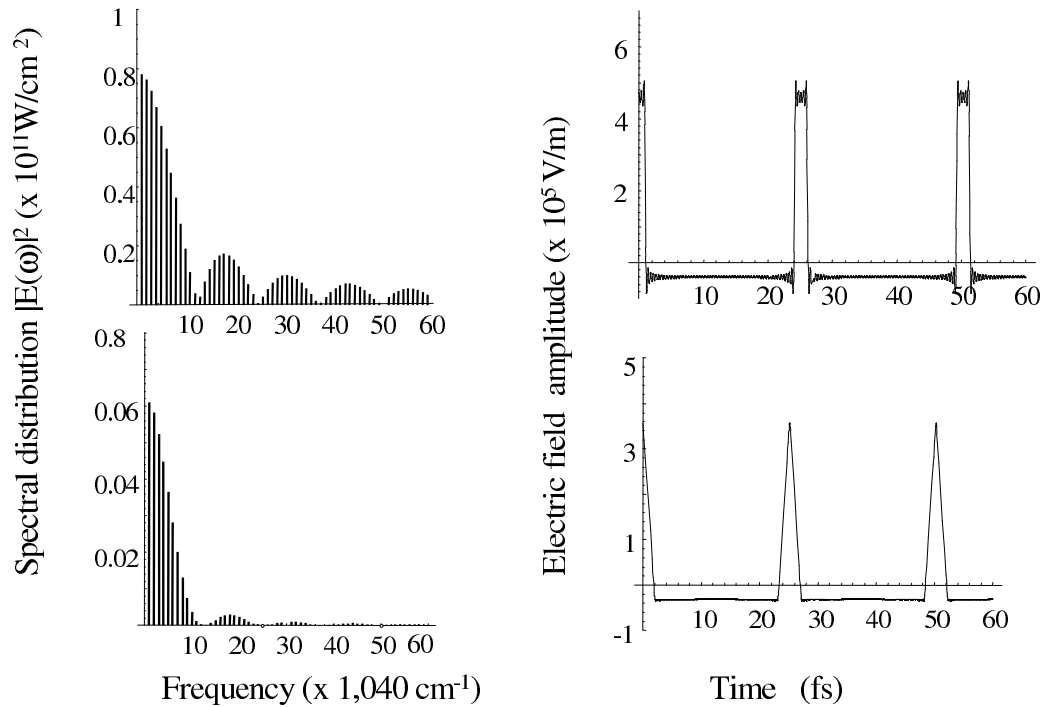
Fig. 9. Taylored amplitude spectrums for synthesis of "square" and "triangle " wave-
forms.

Fig. 8 alludes to the possibility of obtaining different waveforms by adjusting
only the value of the fixed, absolute phase, to (a) 0, (b) $\frac{\pi}{4}$, and (c) $\frac{\pi}{4}$. Furthermore,
the amplitude of the individual frequency components can be adjusted according to
a sinc-function to obtain square type of pulses (Fig. 9 top), or to triangle type of
waveforms (Fig. 9 bottom).

The creation of "designed" laser pulses and their use in attempts to control
molecular events is a current frontier research area, giving hopes for the ultimate goal
"bond selective chemistry". An example of such "sculpted" pulse is shown in Fig.
10, where both amplitude and phase of spectrum of Fig. 4 have been manipulated.
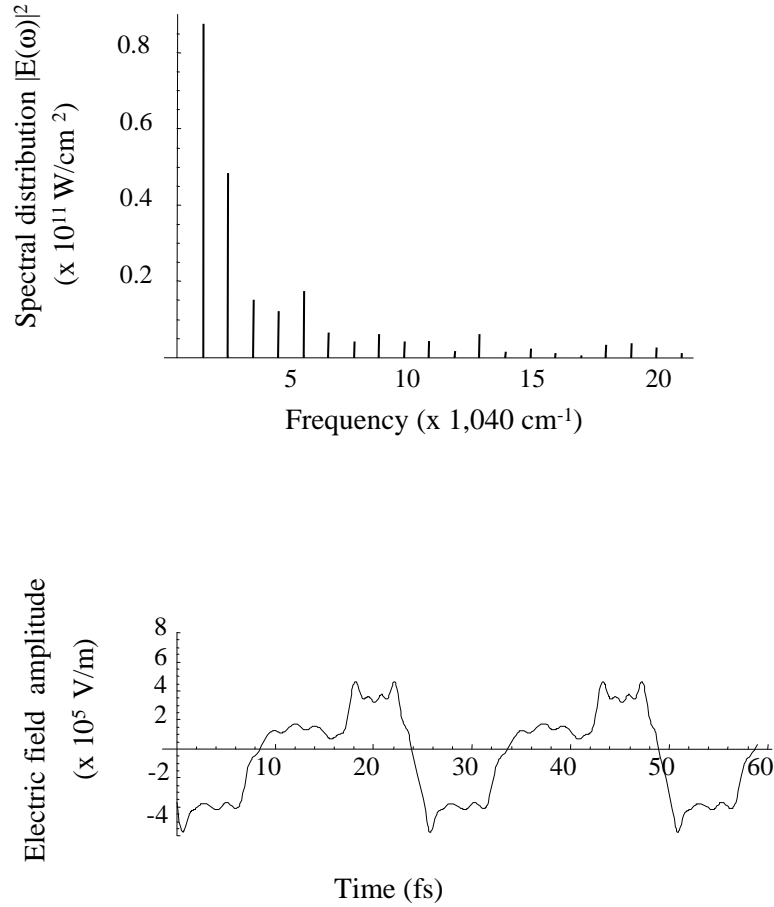
Fig. 10. Arbitrary waveform ("cat" pulse) obtained by adjusting amplitudes and phases of individual sidebands.

D.   Conclusions

In the proposed approach the resulting sidebands are equidistant and reach zero frequency. As a consequence, with proper phase stabilization of the generated sidebands we will be able to obtain reproducible waveforms of arbitrary shape. In our present method, the relative phase of the two fundamental fields changes from shot to shot, making reproducible phase correction of the generated sidebands more difficult. However, in the recent years, several methods showed that stabilization of the phase of

5 femtosecond duration pulses is possible [47]. Another possibility of stabilizing the phases of two laser oscillators could be by locking two external-cavity laser diodes to two longitudinal modes of an optical clock [48], and then using these diodes to injection-seed two Ti:Sapphire regenerative amplifiers. If these laser phases are stabilized on the time scale of minutes, one can in principle stabilize the carrier-envelope phase of the waveform synthesized by the Raman sidebands. Another difficult problem that arises from generation of such ultrashort laser pulses is the actual measurement of their duration. However, one could use multiphoton ionization of a dilute gas, as described in [49] and perform cross-correlation (or autocorrelation) measurements of the waveforms synthesized by a number of chosen sidebands. Despite of the difficult tasks mentioned above, we believe that this approach will open new exciting range of possibilities, not only for the absolute phase control, but also for other phenomena such as sub-cycle pulse shape control, or investigation of multiphoton ionization rates as a function of the sub-cycle shape.

CHAPTER III

MULTIPHOTON IONIZATION BY SINGLE CYCLE PULSES SYNCHRONIZED
WITH MOLECULAR MOTION

A.   Introduction

It was shown previously [22, 30] that molecular modulation technique allows the
generation of not single (isolated) ultrashort pulses, but rather a train of such pulses
with a very high repetition rate (equal to the molecular period, which is of order
of 10-100 fs).   This unique feature of the generated pulses could be exploited in
order to study molecular and electronics dynamics. Of particular interest is studying
photoionization of molecules by strong ultrashort laser pulses. Molecules exhibit a far
richer range of phenomena in a strong field than do atoms, which means that strong
field physics in molecules is less understood than in the atoms.

The essential idea of this project is to generate a train of pulses in a molecular
medium such as molecular hydrogen H_2 or molecular deuterium D_2, which is synchro-
nized with a molecular (vibrational or rotational) motion, and then use a delay line
to send these pulses into a second cell filled with same molecular gas. By changing
the delay δT of the arrival of the pulses with respect to the molecular motion in
the second cell (Fig.11), one can achieve different ionization rates. This picture can
be understood in terms of interference of different multiphoton paths (starting from
different levels of the molecules, with different phasing) constructive or destructive as
shown in Fig. 12. In the "traditional" Raman modulation technique, laser frequencies
are not a multiple integer of their frequency difference, only those multiphoton paths
that involve equal number of photons would reach same energy state in the ionization
continuum. Meanwhile, in the Raman additive technique this condition can be met,
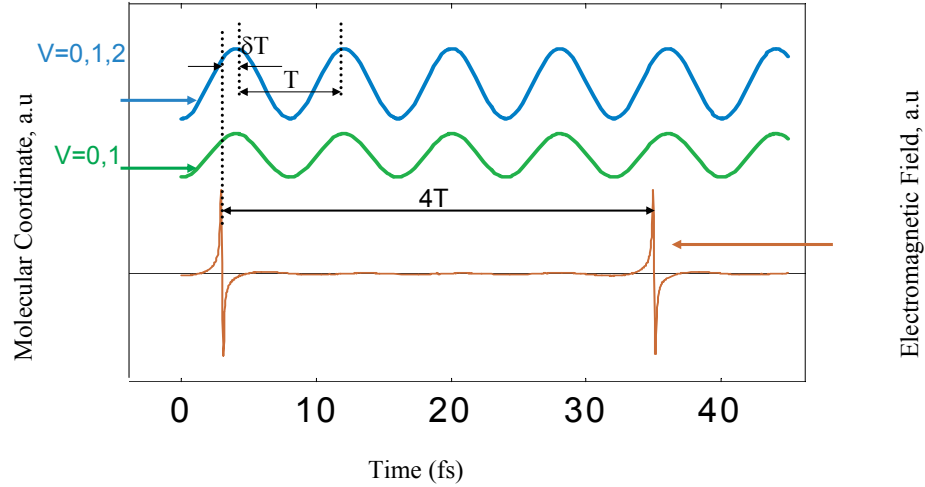
Fig. 11. Synchronization of a train of sin pulses with respect to the molecular motion. Top curve represents a coherent superposition of lowest three vibrational states in a diatomic molecular system $v = 0, 1, 2$, while the bottom curve corresponds to a coherent superposition of lowest two such vibrational states $v = 0, 1$.

which implies that there is a possibility of additional paths for multiphoton ionization (involving different number of photons), paths that can interfere in an EIT manner [50].

B.   Theory

We begin this section by restating the task ahead. We would like to calculate the ionization probability of a a hydrogen molecular gas subjected to trains of ultrashort laser pulse consisting of just one single cycle of oscillation and of moderate intensities 10^{11} W/cm^2 .

Initially, the molecular ensemble is prepared in a coherent superposition of ground and excited vibrational states as it is required by molecular modulation technique. The train of single cycle pulses is generated by compression of a large spectrum of
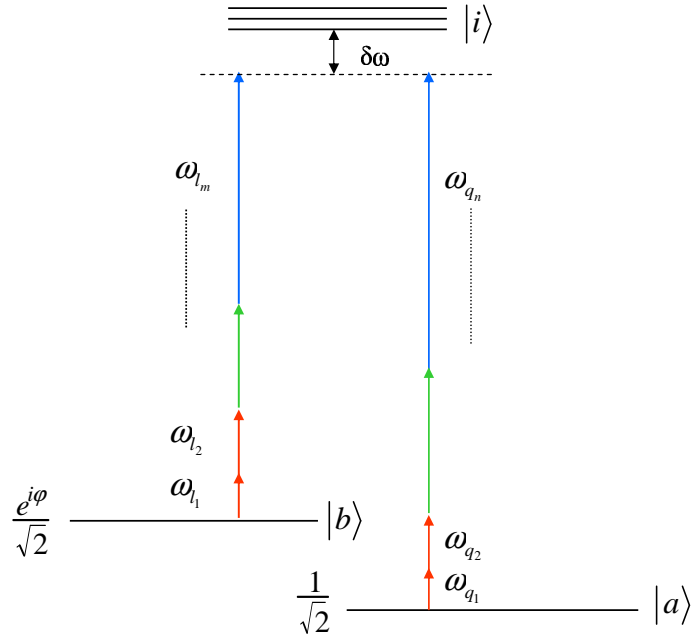
Fig. 12. Possibility of interference of different multiphoton paths starting from two different states $|a\rangle$ and $|b\rangle$ with different phasing.

frequencies using additive technique, a method described in previous chapter of this dissertation. Given such broad spectrum, we expect that nonlinear effects should play a considerable role. Interference effects of EIT type could govern the ionization through different channels [51]. As already demonstrated experimentally in [29] the photoionization of molecules by ultrashort laser pulses is influenced by the time dependence of the electric field (not the envelope), meaning that the shape of electric field will play a considerable role in ionization process.

The present approach is based on the Keldysh formalism, which assumes that the final free electron's state is much more sensitive to the pulse than the bound initial wavefunction [51]. The transition amplitude from an initial bound state i to a final

state f in continuum is given by S matrix element:

$$a_{if}(t) = -j \int_0^t \phi_i \, V(r, t') \, \phi_f dt' \tag{3.1}$$

Here ϕ_i is the unperturbed wave function of the initial state i, and ϕ is the exact wave function of the final state with fixed momentum p. It is difficult to write an analytical expression of the exact final wave function, therefore one can neglect the influence of the external electromagnetic field on the ejected electron, which can then be treated as a free electron [52]. Transition probability is calculated as a first order perturbation theory from the initial electronic ground state to this final free (Volkov type) electron state. The Volkov wave function is defined by [53]:

$$\psi_p(r, t) = \frac{1}{(2\pi)^{3/2}} e^{j\vec{p}\vec{r}/\hbar - j\int_0^t \frac{p^2(t')}{2m_e} dt'} \tag{3.2}$$

First part of this section can be universally applied to describe transition probability from a particular initial electronic state to the final free state under the influence of a ultrashort laser pulse. In the second part of this section, we will apply our results to a particular shape of the laser pulse corresponding to a sine pulse.

Let us start by considering that the time dependent electric field that describes a spatially uniform ultrashort laser pulse is given by:

$$E(t) = E_o \frac{df(\omega t)}{dt} \tag{3.3}$$

where E_0 represents the amplitude of the field, and f describes its time dependence.

Following the standard procedure for calculating transition probability in first order perturbation theory from an initial state $\psi_o(\vec{r}) \, e^{jIt/\hbar}$ to a final state (free electron in AC field) $\psi_p(\vec{r}, t)$, we obtain:

$$w_{ip} = \frac{e^2 E_0^2}{\hbar^2 \omega^3} \left| \int\limits_{-\infty}^{\infty} dt \left(\int e^{\frac{-j\left(\vec{p} + \frac{eE_0}{\omega} f(\omega t)\right)\vec{p}\vec{r}}{\hbar}} \vec{n}\vec{r}\psi_0\left(\vec{r}\right) d^3 r \right) e^{\frac{-jI\Phi(\omega t)}{\hbar \omega}} \right|^2. \tag{3.4}$$

Here I represents the ionization energy, $\vec{n}$ unit vector in the field direction, and $\Phi(\omega t)$ a phase function given by :

$$\Phi(\omega t) = \frac{\omega}{I} \int\limits_0^{\omega t} \left(\frac{p^2(\omega t')}{2m_e} + I \right) dt' - \frac{j\hbar\omega}{I} \ln f'(\omega t). \tag{3.5}$$

The initial state $\psi_0(\vec{r})$ is the electronic wavefunction which corresponds to a coherent superposition of the ground and excited vibrational states and details of its calculation will be given later in the chapter. To simplify our equations, one can introduce some dimensionless parameters given by $\Omega = \frac{\hbar\omega}{I}$, $q = \frac{p}{\sqrt{2m_e I}}$, and $\varepsilon = \frac{e\hbar E_0}{\sqrt{2m_e I^3}}$. Analyzing Eq. 3.4 one can see that $\int\limits_{-\infty}^{\infty} dt \left(\int e^{\frac{-j\left(\vec{p} + \frac{eE_0}{\omega} f(\omega t)\right)\vec{p}\vec{r}}{\hbar}} \vec{n}\vec{r}\psi_0(\vec{r}) d^3 r \right)$ slowly varies with time. Meanwhile, due to the fact that the average photon energy is smaller the ionization energy, (i.e $\Omega < 1$) the integral involving the phase function $\Phi(\omega t)$ is large and rapidly oscillating. These rapid oscillations over the range of integration mean that the integrand averages to zero, with exceptions given by points where the phase function is stationary. Therefore, the integral can be estimated by summing all the integration contributions that arise from zeros of the first derivative of the phase. These zeros can be found from equation:

$$\left. \frac{\partial \phi(x, \vec{q})}{\partial t} \right|_{x=x_s} = 1 + (\vec{q} + \vec{n}\lambda f(x_s))^2 - j\Omega \frac{f''(x_s)}{f'(x_s)} = 0, \tag{3.6}$$

where $x = \omega t$, and $\lambda = \frac{|\varepsilon|}{\Omega}$.

By adding all the contributions from different saddle points, the transition probability reduces to

$$w_{ip} = 2\pi\Omega\lambda^2 \left| \sum_s \frac{M(\vec{q} + \vec{n}\lambda f(x_s))}{\sqrt{|\phi''(x_s, \vec{q})|}} e^{-\frac{j\phi(x_s, \vec{q})}{\Omega}} \right|^2. \tag{3.7}$$
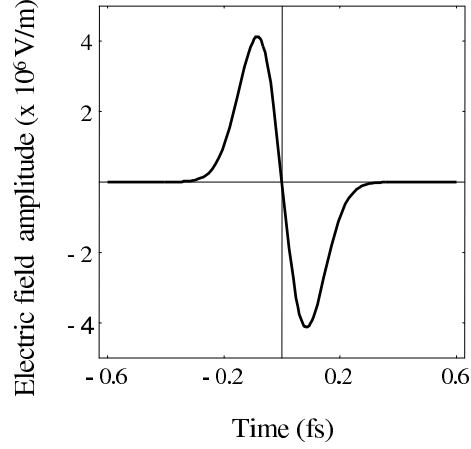
Fig. 13. Electric field of a single sin pulse versus time.

Here the matrix element $M(\vec{q})$ is given by the expression:

$$M(\vec{q}) = \left(\frac{\sqrt{2m_e I}}{\hbar}\right)^{5/2} \int e^{-\frac{i\vec{p}\vec{r}}{\hbar}} \vec{n}\vec{r}\psi_0(\vec{r})\, d^3r. \tag{3.8}$$

Depending on the symmetry of the function $f(x)$, the imaginary part of contributions from different saddle points can be the same, while their real parts differ. As a consequence, oscillations of the ionization probability can occur.

Let us consider now a particular example of the form of the electric field (exemplified in Fig.13) is given by

$$E(x) = -xE_0 e^{\left(\frac{1-x^2}{2}\right)}. \tag{3.9}$$

For this particular waveform, the phase function defined by Eq. 3.5 reduces to

$$\phi(x_s, \vec{q}) = \left(1 + q^2\right) x_s + 2\sqrt{e}\lambda q_{\|} Erf\left(x_s/\sqrt{2}\right) + e\lambda^2 Erf(x_s), \tag{3.10}$$

where $q_{\|}$ indicates the component parralel with the applied field, $Erf(x)$ is the error

function

$$Erf\left(x\right)=\int_{0}^{x}e^{-x^{2}}dx, \tag{3.11}$$

and the two complex saddle points x_s have the following expression:

$$x_{s}\left(q\right)=\sqrt{\ln\frac{e\lambda^{2}}{1+q^{2}}\mp2j\arccos\frac{-q_{||}}{1+q^{2}}}. \tag{3.12}$$

A useful parameter, called Keldysh parameter [52] $\gamma=\frac{\Omega}{|\varepsilon|}$ separates nonlinear multi-photon processes into two distinct regimes: multiphoton ionization, for which $\gamma>1$ and tunneling regime, defined by $\gamma<1$. This parameter γ is simply the inverse of our parameter λ. Therefore, in the multiphoton regime, we are looking for solution of Eq. 3.7 that satifies the approximation $\lambda<1$. Therefore, the matrix element $M\left(\vec{q}+\vec{n}\lambda f\left(x_{s}\right)\right)$ can then be expanded in a series solution in λ, which leads to a transition probability

$$\begin{aligned} w_{ip} &= 4\pi\Omega\frac{\lambda^{2}}{\lambda^{2}+\lambda_{c}^{2}}\mathrm{Im}\left(x_{sm}\right)\left(1+\cos\left(\frac{\pi-4q_{||}}{\mathrm{Im}\left(x_{sm}\right)\Omega}\right)\right)\\ &q_{||}^{2}e^{-\left(\frac{2}{\Omega}\left(1+q^{2}\right)\mathrm{Im}(x_{sm})+\frac{1}{2\mathrm{Im}(x_{sm})}\right)}\left|\int z^{2}\psi_{0}\left(r\right)d^{3}r\right|^{2}. \end{aligned} \tag{3.13}$$

Here $q_{||}$ represents the momentum in the direction parallel with the field applied, λ_{c} is a nonlinear threshold defined by

$$\lambda_{c}=-\frac{1}{2\Omega^{2}}, \tag{3.14}$$

and

$$\mathrm{Im}\left(x_{sm}\right)=\sqrt{\ln\frac{1}{\lambda^{2}+\lambda_{c}^{2}}}. \tag{3.15}$$

Total ionization probability can be found by integrating Eq. 3.13 over the momentum space. The result is given below:

$$
\begin{aligned}
W_i \;=\; & \left(\frac{\pi^{5/2} \lambda^2 \Omega^4 e^{\frac{1}{\mathrm{Im}(x_{sm})\Omega} - \frac{2\mathrm{Im}(x_{sm})}{\Omega}} \sqrt{\frac{x_{sm}}{\Omega}}}{2\sqrt{2}\mathrm{Im}\left(x_{sm}\right)^2 \left(\lambda^2 + \lambda_c^2\right)} \; - \right. \\
& - \frac{\pi^{5/2} \lambda^2 \sqrt{\frac{x_{sm}}{\Omega}} \Omega^3 e^{\frac{1}{\mathrm{Im}(x_{sm})\Omega} - \frac{2\mathrm{Im}(x_{sm})}{\Omega} - \frac{2}{\mathrm{Im}(x_{sm})^3\Omega}} \cos\left(\frac{\pi}{\mathrm{Im}(x_{sm})\Omega}\right)}{\mathrm{Im}\left(x_{sm}\right)^5 \left(\lambda^2 + \lambda_c^2\right)} \; - \\
& \left. - \frac{\pi^{5/2} \lambda^2 \sqrt{\frac{x_{sm}}{\Omega}} \Omega^4 e^{\frac{1}{\mathrm{Im}(x_{sm})\Omega} - \frac{2\mathrm{Im}(x_{sm})}{\Omega} - \frac{2}{\mathrm{Im}(x_{sm})^3\Omega}} \cos\left(\frac{\pi}{\mathrm{Im}(x_{sm})\Omega}\right)}{2\sqrt{2}\mathrm{Im}\left(x_{sm}\right)^2 \left(\lambda^2 + \lambda_c^2\right)} \right) \times \\
& \left| \int z^2 \psi_0\left(r\right) d^3 r \right|^2 . \hspace{4cm} (3.16)
\end{aligned}
$$

In order to calculate the total ionization probability, it is necessary to perform the integration over entire coordinate space $\left| \int z^2 \psi_0\left(r\right) d^3 r \right|^2$. Here $\psi_0\left(\vec{r}\right)$ represents our initial electronic state of molecular system, which corresponds to a coherent superposition of the ground and first excited vibrational state, or, in a more complicated case can correspond to an excitation of molecular wavepacket (i.e. coherent superposition of three or more vibrational states).

One of the difficult problems that arises here is finding a explicit expression of the ground and excited wavefunction of the hydrogen molecule. Molecular calculations are inherently more difficult than atomic calculations, and consequently result in not so accurate descriptions of wavefunctions. Diatomic molecule such as H_2 are the simplest of all molecules, and therefore their analysis, modeling and computation constitute the fundamental step of study of chemical bonds in molecular structures.

Description of covalent bond in diatomic molecules, based on the methods of Heitler-London and Hund-Mulliken represents one of the main achievements of quantum mechanics [54, 55].

New ideas were proposed to improve the numerical accuracy of the Heitler–London and Hund–Mulliken method. The first idea of configuration interaction (CI)

is to incorporate excited states into the wave function. The second idea of correlation introduces explicit dependence of the interelectronic distance in the wave function. The idea of correlation was first demonstrated by Hylleraas [56] in 1929 for the helium atom and by James and Coolidge [57] in 1933 for H_2. The use of configuration interaction and correlation are key evolutionary steps in improving the original ideas of Heitler–London and Hund–Mulliken.

However, the independent particle model remains a good approximation. In the case of H_2, a natural candidate is the orbital of the two-center one-electron molecular ion. The early (1930s) ansatz wave functions of James and Coolidge [57] are expressed in terms of prolate spheroidal coordinates of the two electrons with respect to the two centers of the diatomic nuclei. However, their wave functions are not diatomic orbitals (DOs) in that they are not expansions of the exact one electron H_2^+ states.

The other approach is the use of diatomic (H_2^+) orbitals. Historically, the original idea of using diatomic orbitals as basis for diatomic molecules seems to begin from the work of Wallis and Hulburt [58].

The calculation of H_2^+ wave function improved over the years, culminating in the extensive tabulations by Teller and Sahlin [59]. With such accurate description of the electronic wavefunctions of molecular hydrogen ion [60], we choose to restrict our analysis to molecular hydrogen ion. As the methods for calculation of wavefunctions of hydrogen molecule or other diatomic molecules will get better, our theoretical approach could be easily extended to incorporate such complicated systems.

Let us assume that the applied field is parallel with internuclear axis and oriented along z axis. The internuclear distance z is modulated at modulation frequency ω_m, with ω_m as defined for example in Ref.[22], implying that our initial wavefunction

given by :

$$\Psi_0\left(z,t\right) = \frac{1}{\sqrt{2}}\left(\Psi_0^{vib}\left(z\right) + e^{j\omega_m t}\Psi_1^{vib}\left(z\right)\right) \tag{3.17}$$

is also modulated at the same frequency. Ψ_0^{vib}, and Ψ_1^{vib} represent the well known normalized wavefunctions (ground and first excited) of a harmonic oscillator

$$\Psi_0^{vib}\left(z\right) = \left(\frac{\alpha}{\pi}\right)^{1/4} e^{-\frac{\alpha z^2}{2}} \tag{3.18}$$

$$\Psi_1^{vib}\left(z\right) = \left(\frac{\alpha}{\pi}\right)^{1/4} \sqrt{2\alpha}e^{-\frac{\alpha z^2}{2}} \tag{3.19}$$

Here $\alpha = \frac{\mu\omega}{\hbar}$, with μ being the reduced mass of the molecular hydrogen ion, and ω oscillation frequency. For the case of initial wavefunction coherent superposition of ground and first excited vibrational state, the nuclei execute an oscillatory motion around equilibrium position 1.997466 bohr [60], with a displacement given by

$$z\left(t\right) = \int z\left|\psi_0\left(z,t\right)\right|^2 dz. \tag{3.20}$$
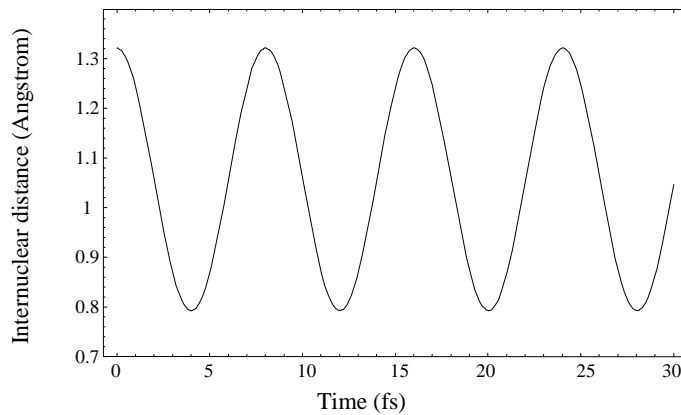
Fig. 14. Internuclear distance of H_2^+ modulated with a frequency of 7.8 fs corresponding to a coherent superposition of ground and first excited vibrational states

This motion is illustrated in Fig.14, and its expression will be used to take in account the response of electronic wavefunction to modulation frequency (i. e. account for response of electronic wavefunction to vibrational motion). It is important therefore that expression of electronic wavefunction of molecular hydrogen ion includes an explicit dependence of the internuclear distance. Following Ref. [60], one can write in elliptical coordinates the electronic part as

$$\psi\left(\xi,\eta,\varphi\right)=\frac{C}{\left(2\pi\right)^{1/2}}X\left(\xi\right)Y\left(\varphi\right). \tag{3.21}$$

C represents a normalization constant, with functions $X\left(\xi\right)$ and $Y\left(\varphi\right)$ satisfying the following differential equations:

$$\frac{d}{d\xi}\left(1-\eta^{2}\right)\frac{dY}{d\eta}+\left(\lambda^{2}\eta^{2}+\delta\right)Y=0, \tag{3.22}$$

$$\frac{d}{d\xi}\left(1-\xi^{2}\right)\frac{dX}{d\xi}+\left(\lambda^{2}\xi^{2}-2R\xi+\delta\right)X=0 \tag{3.23}$$

In the above equations, R indicates the internuclear distance, with parameters δ and λ expressed as:

$$\delta=-\frac{\lambda^{2}}{3}-\frac{2\lambda^{4}}{3^{3}\cdot5}-\frac{4\lambda^{6}}{3^{7}\cdot5^{3}\cdot7}+\frac{26\lambda^{8}}{3^{7}\cdot5^{3}\cdot7}+\frac{92\lambda^{10}}{3^{9}\cdot5^{2}\cdot7\cdot11}-..., \tag{3.24}$$

and

$$\lambda^{2}=-\frac{E'R^{2}}{2} \tag{3.25}$$

with E' being electronic part of energy. Equations 3.21 and 3.22 admit solutions

$$X\left(\xi\right)=e^{-\lambda\xi}\left(\frac{2}{\xi+1}\right)^{1-\frac{R}{\lambda}}\left[1+b_{1}\left(\lambda\right)\frac{\xi-1}{\xi+1}+b_{2}\left(\lambda\right)\left(\frac{\xi-1}{\xi+1}\right)^{2}+b_{3}\left(\lambda\right)\left(\frac{\xi-1}{\xi+1}\right)^{3}+...\right],$$

$$\tag{3.26}$$

Table I. Electronic wavefunction coefficients. Adapted after Ref. [60].

λ	R	a_2	a_4	a_6	b_1	b_2	b_3	C
1.0	1.214301	0.114518	0.001978	0.0000137	0.008496	0.0003706	0.0000411	3.612652
1.1	1.366077	0.139388	0.002919	0.0000243	0.010137	0.0003908	0.0000406	3.660361
1.2	1.523336	0.166929	0.004159	0.0000410	0.011831	0.0004032	0.0000392	3.723734
1.3	1.685909	0.197207	0.005770	0.0000663	0.013559	0.0004086	0.0000373	3.802924
1.4	1.853595	0.230283	0.007815	0.0001035	0.015301	0.0004077	0.0000348	3.898359
1.5	2.026162	0.266212	0.010364	0.0001565	0.017039	0.0004014	0.0000323	4.010611
1.6	2.203349	0.305038	0.013487	0.0002306	0.018757	0.0003906	0.0000294	4.140736
1.7	2.384868	0.346787	0.017253	0.0003317	0.020438	0.0003762	0.0000267	4.292105
1.8	2.570407	0.391465	0.021719	0.0004674	0.022068	0.0003590	0.0000239	4.459978

and

$$Y\left(\eta\right) = 1 + a_2\left(\lambda\right)P_2\left(\eta\right) + a_4\left(\lambda\right)P_4\left(\eta\right) + a_6\left(\lambda\right)P_6\left(\eta\right) + ..., \qquad (3.27)$$

with P_n $(n = 2, 4, 6)$ representing various order Legendre polynomials.

Coefficients $a_2\left(\lambda\right), a_4\left(\lambda\right), a_6\left(\lambda\right), b_1\left(\lambda\right), b_2\left(\lambda\right), b_3\left(\lambda\right)$ used are tabulated in Table I and were used in order to extract the dependence of parameter λ as a function of the internuclear distance R, and implicitly, the dependence of all the coefficients a and b with respect to R. Since internuclear distance changes as in Fig. 14, then all corresponding parameters a, b that enter in the electronic wavefunction will adjust accordingly to our initial conditions of vibrational motion. After the dependence of all coefficients has been established, we apply a transformation from elliptical coordinates to cartesian ones, obtaining the desired expression of wavefunction.

The qualitative dynamics of the molecular hydrogen's wavefunctions as a function of the internuclear distance R is illustrated in several figures. Both two dimensional wavefunction and tridimensional isosurface corresponding to equilibrium position are shown for example in Fig. 15, and Fig. 16 respectively. With increasing internuclear distance R, two dimensional wavefunction exhibit a distortion, shown in Fig. 17, 18, and 19.

Ionization probability can be calculated now according to Eq.3.16. When the electric field of the laser is applied parallel with internuclear axis, the ionization
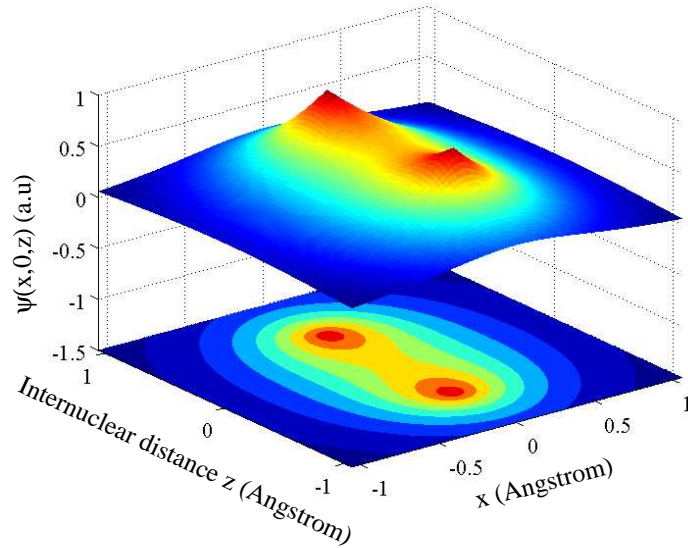
Fig. 15. Two dimensional H_2^+ wavefunction corresponding to an equilibrium distance $R = 1.99$ bohr.

probability is shown in Fig. 20 as a function of both applied field strength and delay time δT with respect to molecular oscillation. Because the internuclear distance is modulated with a frequency equal to the frequency difference of the second harmonics of fundamental fields [34, 61], as described in previous chapter, ionization probability exhibits the same type of oscillations. When electric field is applied in a perpendicular direction to the internuclear axis z, the ionization probability decreases, as shown in Fig. 21. This approach can be extended to the case when initial state is a coherent superposition of three lowest vibrational states. We investigated the same dependence of ionization probability of applied field strength and delay time, for both cases of direction of electric field. Fig. 22 illustrates ionization rates with field applied in the same direction as internuclear axis. For this case of molecular wavepacket excitation, we also observe a reduction of ionization rates for electric field applied perpendicular to internuclear distance as illustrated in Fig. 23.
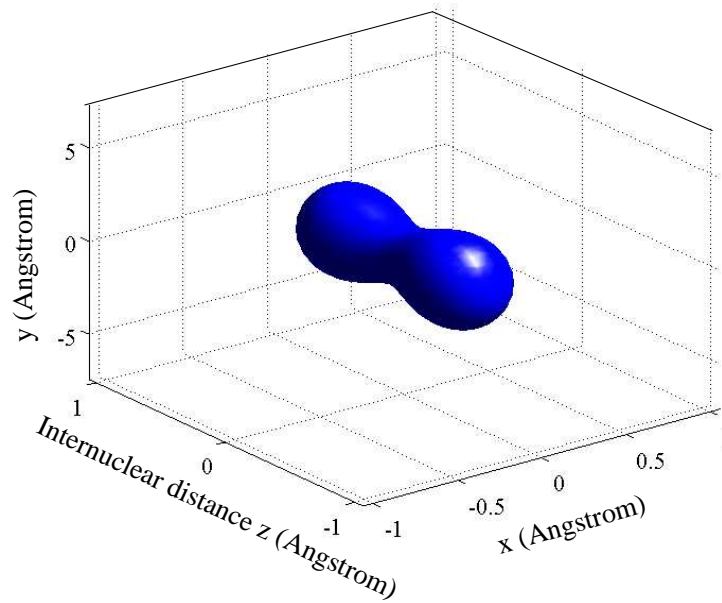
Fig. 16. 3D electronic H$_2^+$ isosurface corresponding to an equilibrium distance $R = 1.99$ bohr.

C. Conclusion

We investigated the multiphoton ionization of H$_2^+$ subjected to single cycle pulses synchronized with molecular motion. We see a difference in the ionization probability twice as big for field parallel with internuclear axis than for perpendicular case. Different ionization rates can be achieved by producing a coherent molecular oscillation in a target cell, and adjusting the time delay between this oscillation and the train of laser pulses. This method can be easily extended for more complicated molecules, or studying a coherent excitation of a large number of molecular vibrational states.

43
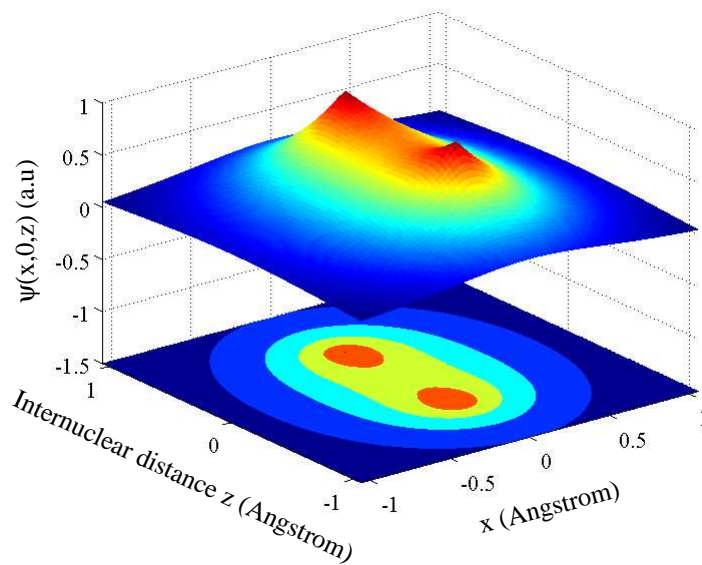
Fig. 17. Two dimensional H$_2^+$ wavefunction corresponding to an internuclear distance $R = 1.72$ bohr.
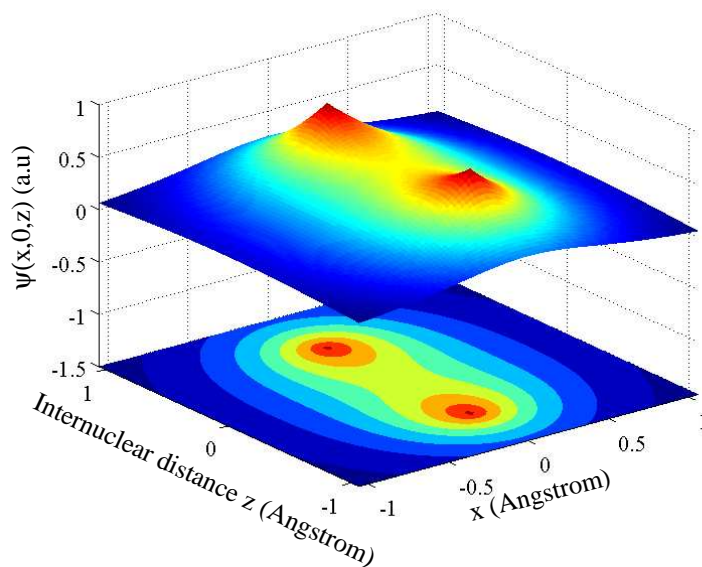
Fig. 18. Two dimensional H$_2^+$ wavefunction corresponding to an internuclear distance $R = 2.22$ bohr.
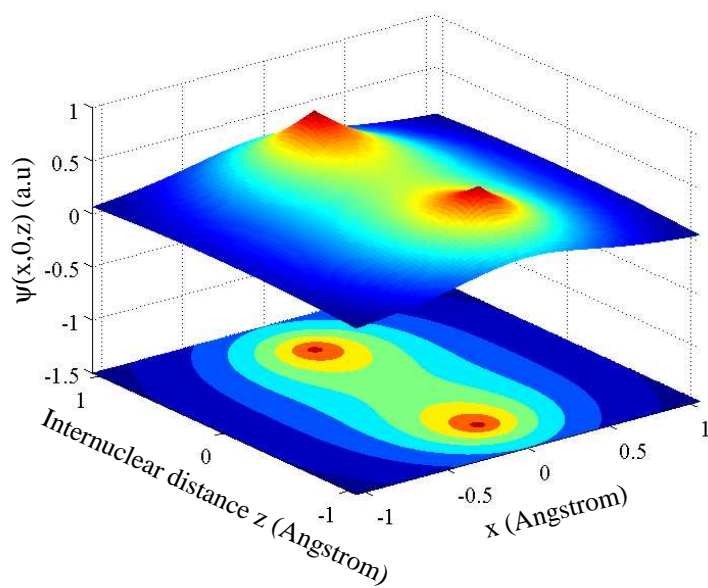
Fig. 19. Two dimensional H$_2^+$ wavefunction corresponding to an internuclear distance $R = 2.25$ bohr.
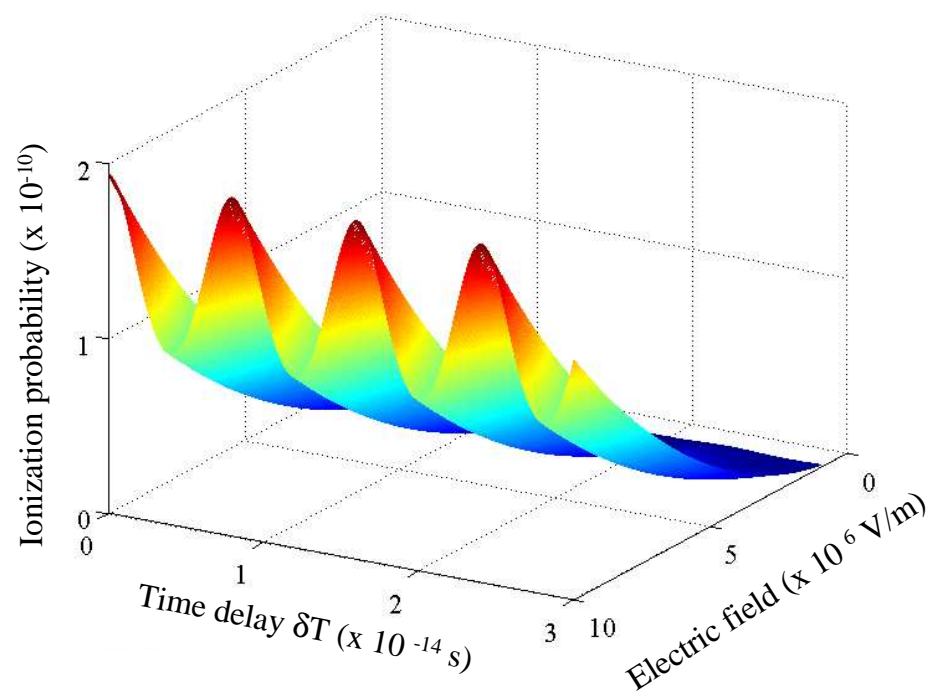
Fig. 20. Ionization probability of H$_2^+$ as a function of applied electric field and time delay δT. The initial state is a coherent superposition of the lowest two vibrational states. Here electric field is parallel with internuclear axis z. Oscillations in ionization probability are due to the response of electronic wavefunction to the modulation of internuclear distance R.
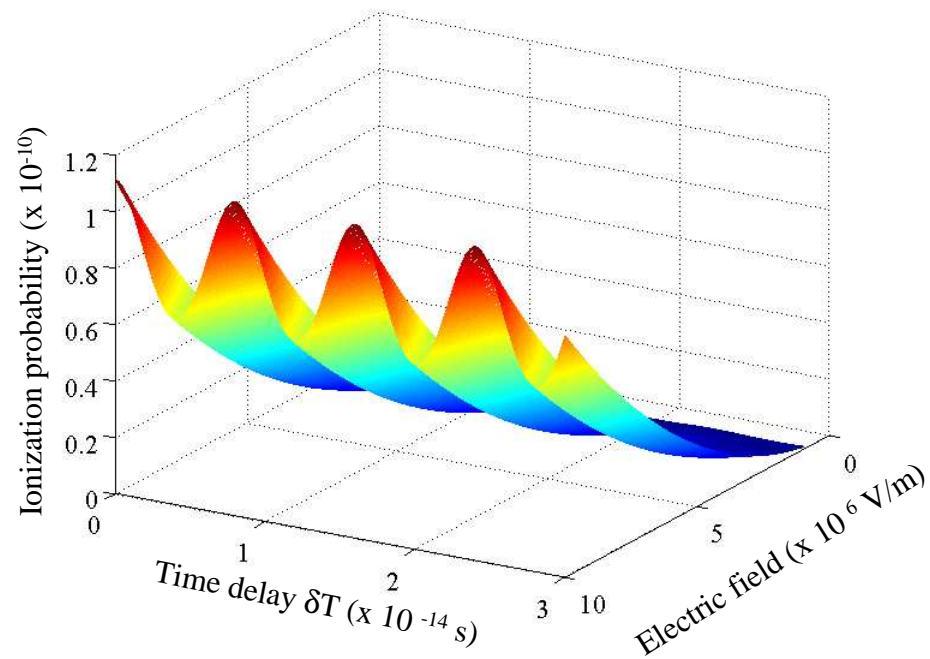
Fig. 21. Ionization probability of H_2^+ as a function of applied electric field and time delay δT. The initial state is a coherent superposition of the lowest two vibrational states. Here electric field is perpendicular to the internuclear axis z. Oscillations in ionization probability are due to the response of electronic wavefunction to the modulation of internuclear distance R. A reduction in the ionization rates is observed when compared to parallel field case.
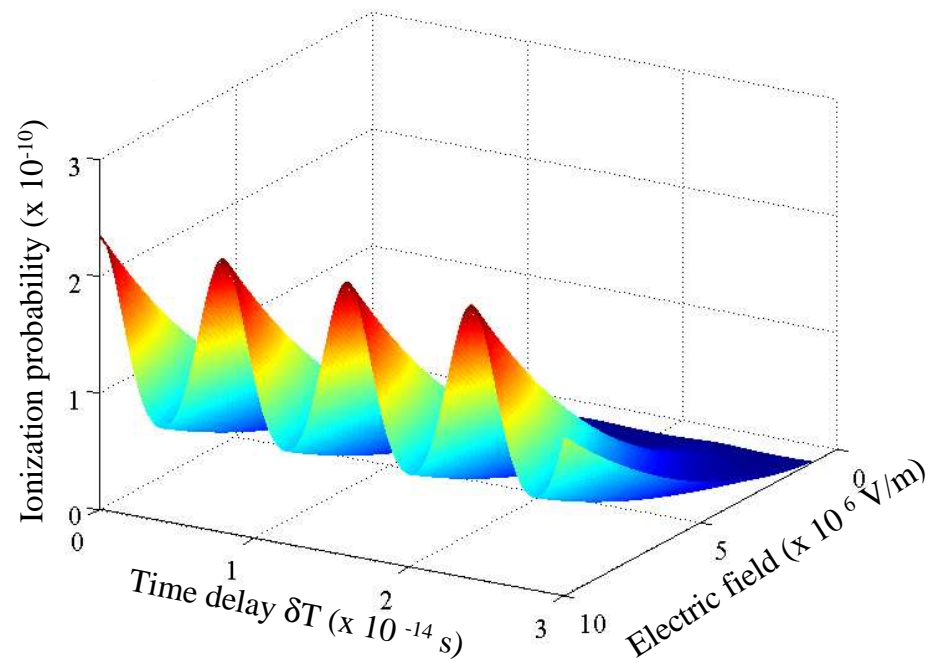
Fig. 22. Ionization probability of H$_2^+$ as a function of applied electric field and time delay δT. The initial state is a coherent superposition of the lowest three vibrational states, which indicates a molecular wavepacket excitation. Here electric field is parallel to the internuclear axis z. Oscillations in ionization probability are due to the response of electronic wavefunction to the modulation of internuclear distance R. Ionization probability increases as compared to the case when initial state is a coherent superposition of lowest two vibrational states. Ionization probability decreases as compared to the case corresponding to field parralel to internuclear axis.
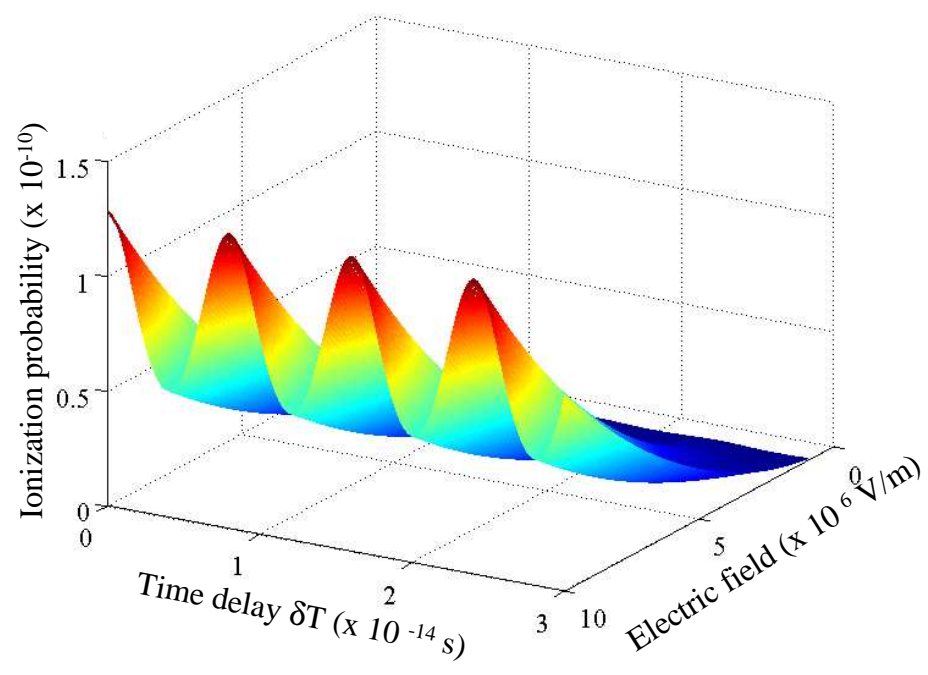
Fig. 23. Ionization probability of H$_2^+$ as a function of applied electric field and time delay δT. The initial state is a coherent superposition of the lowest three vibrational states. Here electric field is perpendicular to the internuclear axis z. Oscillations in ionization probability are due to the response of electronic wavefunction to the modulation of internuclear distance R.

CHAPTER IV

BUILDING EXPERIMENTAL SETUP

A. Introduction

The basic experimental setup for the molecular Raman modulation technique is presented in Fig. 49. Two synchronized nanosecond lasers are loosely focused to a spot size of 300-400 μm in a 1 m long cell filed with deuterium (from 1 Torr to 750 Torr). The white light produced in the Raman cell consisting of equally spaced frequencies is dispersed by a set of prisms and projected into a white screen.

The experimental setup necessary for demonstration of Raman modulation technique relies therefore on construction of two tunable injection - seeded pulsed Ti: Sapphire lasers that allows driving of different Raman transitions in molecules such as deuterium or hydrogen. Two different types of laser configurations eare build and shown in this project: a novel short 6 cm linear cavity pumped from two sides by the second harmonic of a Nd:YAG laser, at a repetition rate of 10 Hz, and a more traditional ring cavity configuration with a length of 12 cm. Both lasers are injection seeded by two tunable laser diodes (Littman, Sacher laser TEC 500) and (Litrow, Sacher laser TEC 100).

Injection seeding is a well known method of controlling the properties of lasers, namely the spectral output, by using a low power output laser with a narrow spectral bandwidth - sometimes referred to as the seed laser. Output power of the seed laser is injected into an oscillator and serves as a seed from which the pulsed laser output grows. In competition, naturally occurring pulses begin from the zero point energy of the laser resonator or from spontaneous emission. If the injected seed is large enough, the pulse growing from the injected seed will deplete the gain of the laser material be-
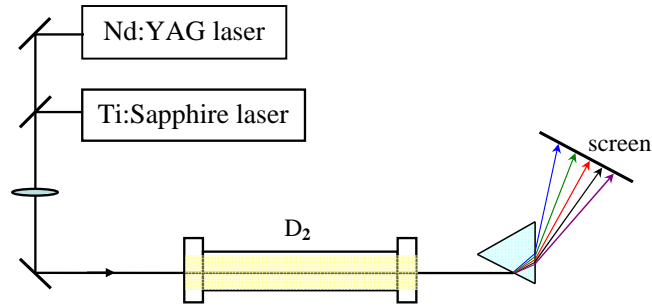
Fig. 24. Traditional Raman experimental setup

fore the natural pulses become large. If so, the laser output will mimic the properties of the seed rather than the properties of the free running laser. The construction of the new lasers is different than the ones used in the previous experimental setup [22]. By keeping the cavity length short to a minimum, and by maintaining pulse energy, shorter pulses are achieved. This will be a substantial benefit for Raman generation, since by employing shorter laser pulses, a larger dephasing of molecular gas can be tolerated. Specifically, large atomic (or molecular) coherence can be established in a transient regime by a combination of narrow line width (bandwidth-limited) laser pulses with duration shorter than the dephasing time [31]. Since the dephasing of a dipole-forbidden transition is often limited by the collisional decoherence rate (which in turn is proportional to the gas pressure), shorter pulses will allow us to work with larger ensemble densities, provided that the pulse energy is sufficiently high. Furthermore, the intensity of the two driving fields in a molecular cell can be increased without a tight focusing, which will make the generation process more efficient.

In addition to the construction of driving lasers, a vacuum setup was build that allowed the connection of a 1 m long Raman cell filled with deuterium at pressures from 1 Torr to atmospheric pressure.

B. Laser construction

1. Linear cavity

The absorption band of Ti:Sapphire is centered around 490 nm, and makes it suitable for pumping by a variety of lasers such as argon ion, frequency doubled Nd:YAG or YLF lasers. Its emission bandwidth allows for a broad tunability range from 650 nm to 1100 nm, making it a very good candidate for high power, tunable lasers. The operation of pulsed tunable single longitudinal mode Ti:Sapphire, tuned in the narrow vicinity of the Ti:Sapphire gain peak has been described in previous work [62, 63]. Another group of articles presents the construction of such tunable lasers in a broader tuning range, [64, 65] which was accomplished by employing intracavity frequency-selective elements. These lasers provide sufficient tunability, good transverse mode structure, high output energy, and pulse duration of several tens of nanosecond due to long laser cavity length. For our applications it is desirable that pulse duration is less than 10 ns, and that the Ti:Sapphire laser operates at wavelengths tuned away from its gain peak (in particular, we are interested to make it work at 807 nm, as required for the experiment described in [24]).

We have constructed a compact linear-cavity Ti:Sapphire laser optimized for generation of few-nanosecond Fourier-transform-limited pulses at a sufficiently high pulse energy. The laser is injection-seeded by a continuous-wave (CW) external-cavity laser diode, which produces single-mode radiation tunable around 810 nm wavelength. Linear cavity design allows for a large roundtrip gain and short roundtrip time. In combination with a large output coupling, this results in a short cavity lifetime and a correspondingly short output pulse duration.

A schematic diagram of our injection seeded linear Ti:Sapphire cavity is presented in Fig. 25. In this figure, the output of 20 mW external cavity diode laser(Sacher
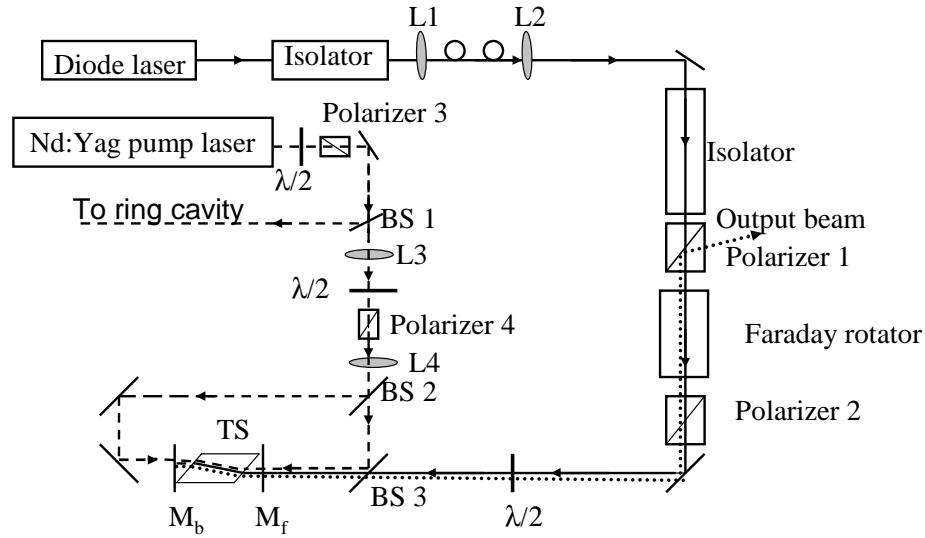
Fig. 25. Layout linear Ti:Sapphire cavity setup. Continuous line indicates direction of seed beam, short dashed line shows direction of the generated output pulse, and long dashed line gives pump direction.

Littman 820) is passed through an isolator1 with 82% transmission, then the beam is split into 5/95 ratio by a glass plate, with a small reflection send for measurement. The remaining transmitted part is then coupled into a single mode fiber with 45% percent efficiency. The purpose of coupling diode laser into fiber is manifold: to achieve a better beam profile- free of astigmatism and almost gaussian, and to make Ti:Sapphire alignment insensitive to the diode path beam changes. The diode laser can be tuned between 805 - 830 nm with a course tuning range of 20 nm, and a moderate piezoelectric fine tuning range of about 0.5 nm. Depending on the tuning wavelength, the output power of the laser changes from about 15 mW at the lower tuning border to 20 mW at maximum gain for 820 nm. Some typical output power curves for different piezo temperatures are shown in Fig. 26 at the wavelength of our interest 807 nm.

The wavelength is monitored by a Burleigh WA 1500 wavemeter with a 10 MHz
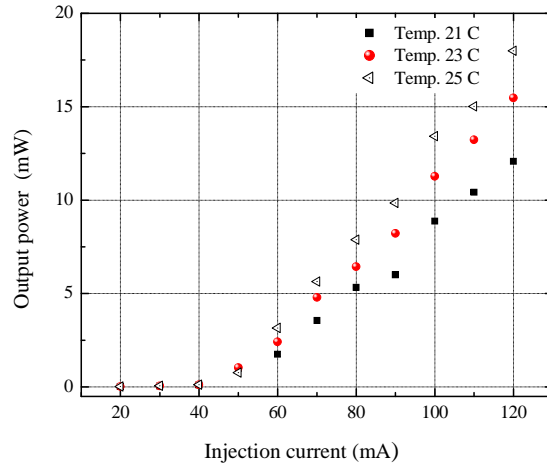
Fig. 26. Typical output power of the Littman diode laser for different control temperatures.

resolution, as shown in the setup of Fig. 27. Diode polarization is elliptical, with a ratio of 1:4. The Picosecond bias tee option allows the modulation of current from 3.5 KHz to 7 KHz and it can be used for lock in setup of the Ti:Sapphire cavity.

After being coupled and uncoupled by the two lenses L_1 and L_2 in Fig. 25, the injected diode signal passes through optical isolator OFR, and then through the half wave plate where polarization is changed to p. At the output of the fiber, the beam was collimated, and its size determined by knife-edge technique to be 1.4 mm diameter. A dichroic beamsplitter BS3, which reflects the green 532 nm pump beam and transmits infrared is used for combining the pump and seed beams together, and further send them to laser cavity. The generated laser beam is then separated from the incoming seed line by rotation of polarization by 90 degrees of an Faraday rotator, as shown in Fig. 25 by the thin dashed line.

The 12 cm long Ti:Al$_2$O$_3$ cavity consists of a 70 % reflectivity flat output coupler mirror and 100 % reflectivity back flat mirror. The cavity is pumped from both sides by the second harmonic of a Nd:YAG laser, therefore both cavity mirrors are
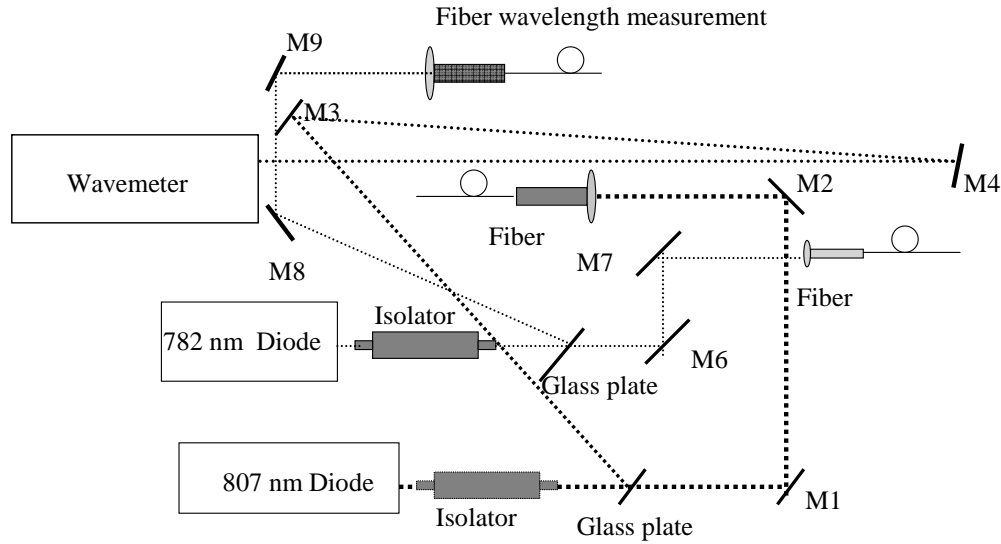
Fig. 27. Layout of the diode laser setup.

transparent at the 532 nm wavelength.

The Ti:Sapphire crystal used in our cavity is manufactured by Crystal Systems and grown by heat exchanger method HEM to achieve high efficiency of lasing. Its length was 10 mm, with a diameter of 9 mm. The crystals facets are cut at Brewster angles for minimizing reflections of the pump beam, and avoid reflection losses of circulating intensity. The absorption coefficient at the pump wavelength is 2.944/cm, with a figure of merit FOM greater than 150. In addition, the crystal was cooled by a Peltier thermal electric cooler mounted on the top of the crystal holder on a 2 cm copper block. The copper block was glued on top of the crystal holder with the aid of thermal conducting epoxy, and a heat sink placed on the hot side of the Peltier element was used to dissipate the heat. The temperature of the crystal was monitored with the aid of an thermocouple placed inside the copper block.

As a pump source for Ti:Sapphire cavity we used a commercial, Q-switched frequency doubled Nd:YAG laser (Quanta-Ray 6350) with of a pulse length of 8 ns

duration at a repetition rate of 10 Hz. The 532 nm pump beam was split by a 46/54 beamsplitter and used to pump two different cavities (ring cavity and linear cavity) with the smaller reflected energy going to the ring cavity. The remaining 60 % is directed to the linear cavity and collimated by a pair of lenses such that the spot size on the crystal is about 1.5 mm as measured by knife edge techniques. In order to increase the output energy of our laser, we choose to pump the cavity from two sides, with equal fractions (50/50 %) of the 532 nm energy being pumped from both back and front cavity mirrors.

In one of our experiments, it is necessary to achieve synchronization of two Ti:Sapphire systems that we build. The use of two pump lasers, the timing of which can be controlled independently is a quite effective method, but the jitter in the two Ti:Sapphire lasers could limit this stability. The other option is pumping both cavities by the same pump source, and achieving synchronization by simply changing the dividing ratio of the pump energy for the two cavities. For "fine" tuning of our synchronization, reduction of the pump intensity of one of the lasers can be employed such that its buildup time is delayed with respect of the other laser. A polarizer and a $\lambda/2$ waveplate are introduced in the path of the 532 nm pump beam that goes to the linear cavity for a better control of the syncronization of our lasers. In order to align the cavity with the seed beam, a Michelson interferometer was build to ensure that both cavity mirrors are perpendicular to the incident beam, and then the finesse of the cavity was maximized up to a value of 10, which corresponds to the theoretical value that we expected.

For single mode operation, the mode of the injection seed must match the mode of the power oscillator. This type of resonance matching involves a precise control of the cavity length. An option will be the use of feedback loop in order to keep the cavity roundtrip length matched by an integer multiple of the seed laser wavelength.

This control can be achieved for example, by mounting one of the cavity mirrors on a piezoelectric transducer, PZT, and keep seeding level constant by controlling the voltage of the PZT. A weak reflection of seed beam can be picked off from the Ti:Sapphire crystal and send to a detector, for monitoring of the circulationg power inside the cavity. We employed such detection scheme for our ring cavity laser. However, there is another possibility of keeping the cavity locked, namely to send the feedback signal to the diode's piezo voltage, thus controlling the seed wavelength electronically.

In our experiment, we chose the second method, adjusted the seed laser wavelength to stay in resonance with the Ti:Sapphire cavity, and obtained stable seeding. A feedback loop (servo loop) was build in order to adjust the seed wavelength. We find that once the cavity is locked near the peak of resonance using the home build electronics, tunability can be achieved by simply changing the temperature of the cavity with the aid of the cooler mounted of top of the crystal.

Spatial hole burning may occur during the periods when resonance cavity condition is established, which means that the output energy of the injected signal is lower than the unseeded oscillator energy. This is essentially an effect that occurs when counterpropagating narrow bandwidth light waves are superimposed in such a way that they create a standing wave pattern, the period of which is half of the wavelength. In gain media such as Ti:Sapphire, this results in a preferential saturated gain in the antinodes of the pattern. As a consequence, this may result in difficulty achieving single frequency operation, and potentially reduce output energy. However, the large output coupling gives us a hope for this effect to be small enough for our laser to produce a single-longitudinal-mode output.

Lasing threshold occurs at about 15 mJ/pulse pump energy. The output pulse energy reaches the highest value of 20 mJ/pulse (at 70 mJ/pulse pump), with the slope efficiency of 37 % as it is shown in Fig. 28. We measured the temporal pulse
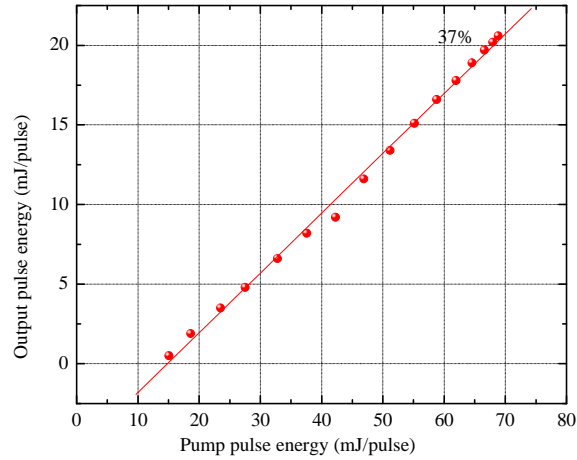
Fig. 28. The output energy of the Ti:Sapphire linear cavity as function of the pump energy. Continuous line indicates the slope efficiency of 37%.

shapes with a fast home-made photodiode detector and a 1 GHz (5 GS) Tektronix TDS 684C oscilloscope. A typical pulse profile for seeded operation is shown on Fig. 29. Figures 29 (a) and (c) correspond to seeded and unseeded operation for two different pumping energies, while figures (b) and (d) illustrate the average over four shots of temporal profile. The pulse duration is 4.9 ns FWHM. When seeding signal is switched off, generated pulse builds up slower: about 6 ns extra delay is measured, as represented in Fig. 29. Both seeded and unseeded pulses have similar shape: front slope is slightly steeper than the back one.

In a previous configuration which employed a dispersion element inside the cavity, it was determined that the laser operates in a single longitudinal mode regime. The spectrum of seeded generation was taken by a scanning confocal Fabry-Perot interferometer (finesse 300). Its free spectral range (FSR) is 2 GHz, which is larger than the laser cavity FSR of 1.86 GHz. Measurement of the spectrum is shown in Fig.30. The Fabry-Perot cavity length is scanned continuously, as the transmitted pulse energy is measured. Each data point represents one laser shot. Spectra "a"
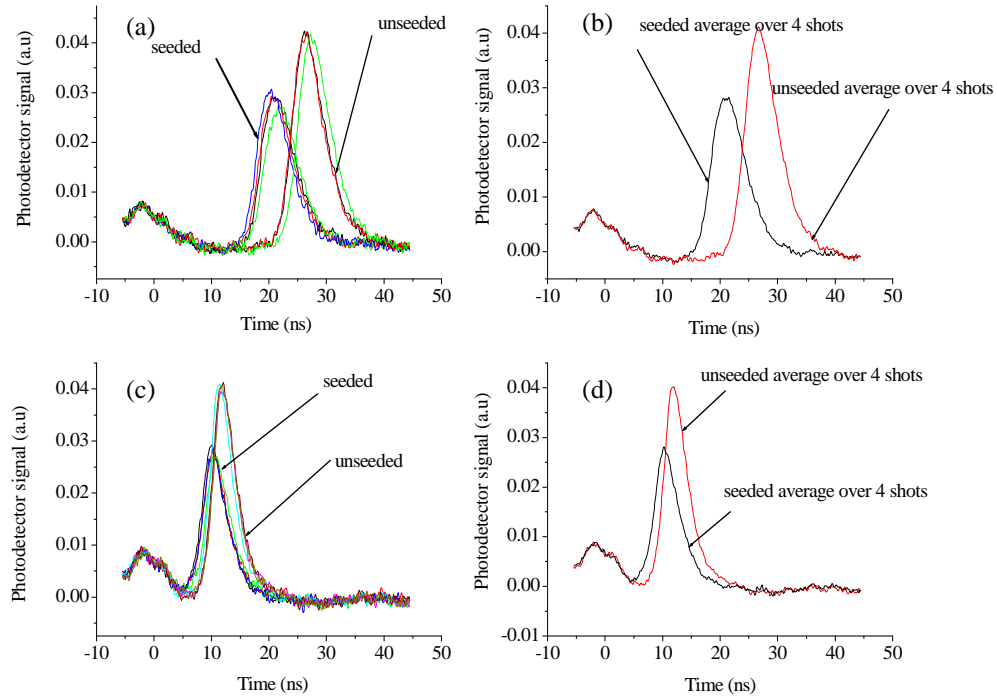
Fig. 29. Temporal profiles of Ti:Sapphire linear cavity output pulse in seeded and unseeded regime for two different pumping energies. In (a) and (b) pumping energy was 20.8 mJ/pulse, while the pump energy in (c) and (d) was set to 39 mJ/pulse. Nd:YAG pump oscillator was set to 100 %, with an amplifier level of 80 %. The small pulse to the left represents the 532 nm pump as seen by detector. One can notice that jitter of output Ti:Sapphire pulse is very small.

and "b" are independent measurements taken under the same operating conditions for the whole system. The cavity length as well as seed wavelength fluctuate during the measurement. This results in a noisy spectrum. However, the spectral width is reproducibly measured to be about 100 MHz. Fourier transformation of the temporal profile of the seeded pulse was calculated and shown by the solid curve on both graphs of Fig.30, which closely matches the experimental data. The calculated transform-limited spectral width is 87 MHz FWHM. For comparison, spectral width for a Gaussian temporal profile is calculated by $2 \ln 2/t$ where t is the pulse duration
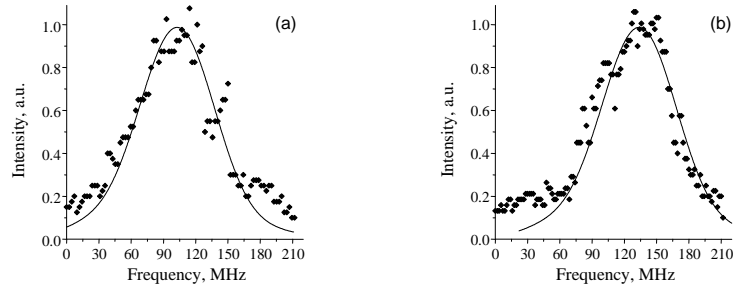
Fig. 30. The spectrum of the seeded generation as taken by a scanning confocal Fabry-Perot interferometer. Each point on the graphs corresponds to one laser shot, obtained with continuous scanning of the Fabry-Perot interferometer. "a" and "b" spectra are two independent measurements.

at FWHM; it gives 90 MHz for a 4.9 ns pulse.

Even though our cavity is a little bit shorter, the seeded pulse duration is about the same as in the previous configuration (4.6 ns as shown in Fig. 31). We expect that these pulses are also near transform-limited.

2. Ring cavity

We proceed further to describe the operation of the second Ti:Sapphire ring cavity that we build. The need of second tunable cavity is justified by the need of driving for example rotational transitions in deuterium using two Ti:Sapphire lasers, an experiment which will be shown in next chapter.

The new cavity was build in a ring configuration which is similar to configurations previously employed for example in [63]. The ring cavity consists of three mirrors, with Ti:Sapphire crystal being the only intracavity element. In contrast with linear configuration, the advantage of ring configuration is elimination of spatial hole burning, since cavity oscillates unidirectional with respect to seed beam [63]. The cavity length including the index of refraction of Ti:Sapphire, is about 8 cm. The output

Fig. 31. Linear cavity Ti:Sapphire linear laser pulse width as a function of pump energy. The solid line shows the empirical dependence $\tau_{pulse} \approx \tau_{cavity} \left(1 + \frac{E_p^{th}}{E_p - E_p^{th}} \right)$ and is given to guide the eye. τ_{cavity} is the cavity lifetime given by $\tau_{cavity} \approx \frac{2nL}{c(1-R_1 R_2)}$, and E_p^{th} is the threshold pump energy. Here n represents the index of refraction of the gain media, L is the length of the cavity, c speed of light, R_1, R_2 reflectivities of cavity mirrors. The fit parameters are $E_p^{th} = 14.54$ mJ/pulse, and cavity lifetime $\tau_{cavity} = 3.85$ ns. The agreement with experimental obtained parameter $E_p^{th} = 15$ mJ/pulse from Fig.28 is remarkably good.

coupler is a flat mirror with a reflectivity of 36 %. The other two mirrors are high reflectors over the range of 750-820 nm. One of the high reflectors is a dichroic beam-splitter, through which 532 nm pump beam is passed. The remaining third mirror is mounted on a piezoelectric translator (PZT) in order to achieve cavity and seed frequency matching.

The schematic of this cavity is shown in Fig.32. In a similar fashion as for linear cavity, the seed beam from a temperature stabilized 40 mW single mode laser diode operating at 782 nm (Sacher laser Littrow TEC 100) is passed through an isolator, then gets coupled into fiber with 52 % efficiency. After fiber, the injected seed signal
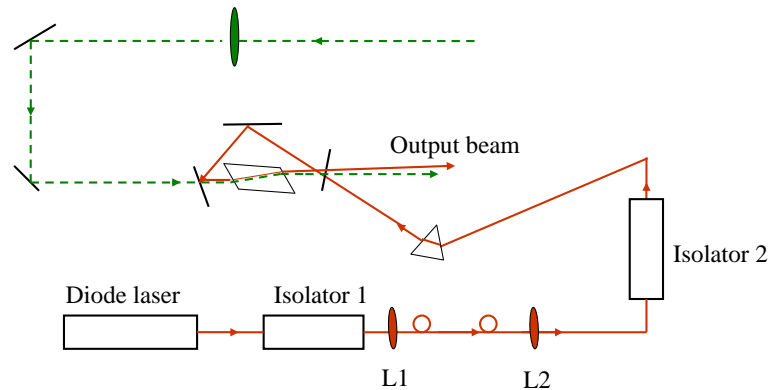
Fig. 32. Layout of the ring Ti:Sapphire cavity setup. Continuous line indicates direction of the seed beam, and dashed line gives pump direction.

goes through a second isolator, then is redirected into cavity by a fused silica prism. Here the prism is employed as en extra element of protection of laser diode against any feedback of the ring cavity. Due to power loss in the isolators, the power of the seed beam incident on the output coupler is about 15 mW.

The cavity is pumped by a 10-Hz frequency doubled Nd:YAG laser. The pump beam has a FWHM pulse duration of about 8 nanoseconds, and its direction is shown by dashed line in Fig. 32. A 100 cm focal length lens is used to reduce the 532 nm beam to a 1.5 mm diameter spot at the crystal, with focal point slightly behind the cavity.

The crystal itself is a rod of 1 cm long and 5 mm in diameter doped for 2.5 cm^{-1} absorption at the 490 nm, with C-axis aligned to be parallel to the polarization of circulating radiation (p polarized). We found that injection seeded operation of this laser is very sensitive to the temperature changes of the crystal, therefore we mounted a Peltier thermal electric cooler on top of the crystal holder on a 2 cm copper block. We employed essentially the same scheme as for cooling of linear cavity. The temperature of the crystal was monitored with the aid of an thermocouple placed

inside the copper block.

The length of the cavity is stabilized by matching a particular longitudinal mode of laser to the frequency of the seed beam, as described previously in the chapter. We chose to modulate diode's current at 102 KHz frequency. The modulated signal is picked off from Ti:Sapphire crystal face and send to the input of a commercial lock-in Stanford Research Systems, which then adjusts the dc bias on the PZT. In order to prevent the lock-in to be saturated during the time when the ring cavity is pulsed, the 532 nm pump reflection is blocked before reaching the detector. However, the infrared pumped pulse that overlaps with seeded pulse needs to be cutoff by a home build electronic circuit. This circuit employs several filters and amplifiers which filter out the pulses at 10 Hz repetition rate.

The output energy is shown in Fig.33, with an efficiency of 35%. The laser's efficiency decreases with increase in the crystal's temperature, and for a large enough temperature, the seeding operation ceases. Therefore, a careful monitoring of temperature of the cavity is required.

The pulses have a similar duration (4 ns) as the ones from the linear cavity and they are shown in Fig. 34.The solid line shows the empirical dependence $\tau_{pulse} \approx \tau_{cavity}\left(1 + \frac{E_p^{th}}{E_p - E_p^{th}}\right)$ and is given to guide the eye. τ_{cavity} is the cavity lifetime given by $\tau_{cavity} \approx \frac{nL}{c(1-R_1R_2R_3)}$, and E_p^{th} is the threshold pump energy. Here n represents the index of refraction of the gain media, L is the length of the cavity, c speed of light, R_1, R_2,R_3 reflectivities of cavity mirrors. The fit parameters are $E_p^{th} = 54.25$ mJ/pulse, and cavity lifetime $\tau_{cavity} = 1.9$ ns. The actual measured pump threshold is 48 mJ/ pulse, while the cavity lifetime has an estimated value of 1.3 ns. The buildup time of the ring oscillator (defined as the difference between the leading edges of the pump and output pulses) is reduced when the cavity is seeded. Fig. 35 shows the buildup time in the case of seeded operation. The solid line gives the empirical dependence
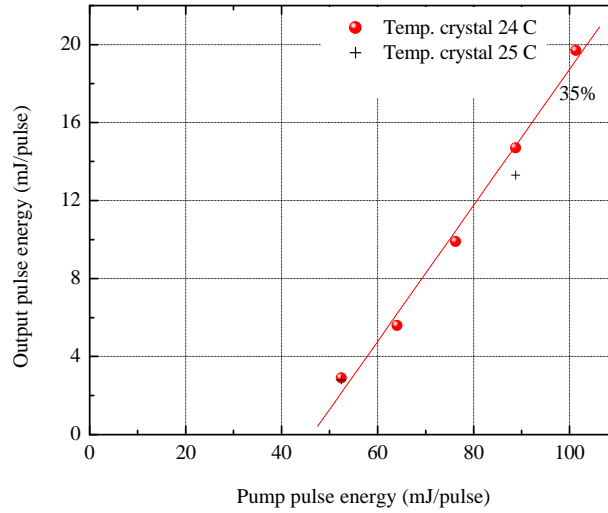
Fig. 33. Output energy of Ti:Sapphire ring cavity as function of pump energy. The crystal was initially cooled at 24 degrees Celsius, then the temperature increased to 25 degrees Celsius. The second set of data shows the output generated energy after the crystal has been heated by one degree Celsius. At low pump power, there is no change in the output energy, but this energy decreased at higher pump power. Here the Nd:YAG pump oscillator was set to 100 %, with an amplifier level of 80 %. Slope efficiency is illustrated by solid line and its value is 35%.

of buildup time $\tau_b \approx b\tau_{cavity}\frac{E_{th}}{E-E_{th}}$ where τ_{cavity} represents the lifetime of the cavity, and E_{th} represents the threshold energy [6]. Fitting parameters values are $E_p^{th} = 53$ mJ/pulse, cavity lifetime $\tau_{cavity} = 1.9$ ns, and $b = 5$.

The transverse intensity distribution of the laser shots was picked up with burn paper and was excellent. The beam profile was round and smooth, whereas in the unseeded operation, there were two distinct round spots.

C. Conclusion

Two injection seeded Ti:Sapphire lasers have been build in order to study and exploit coherent transient phenomena in atomic and molecular gases, and in particular ex-

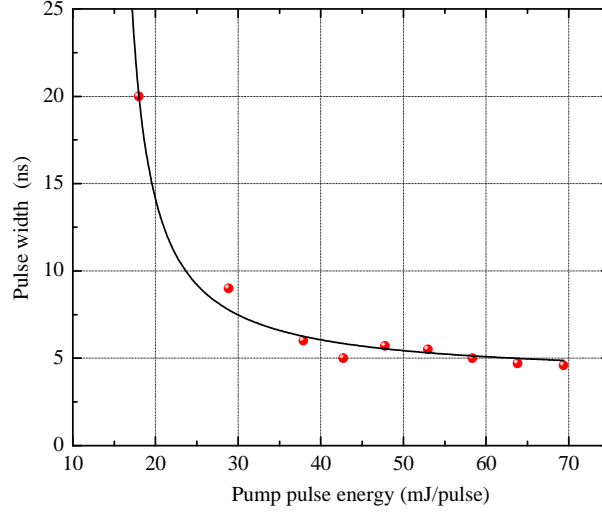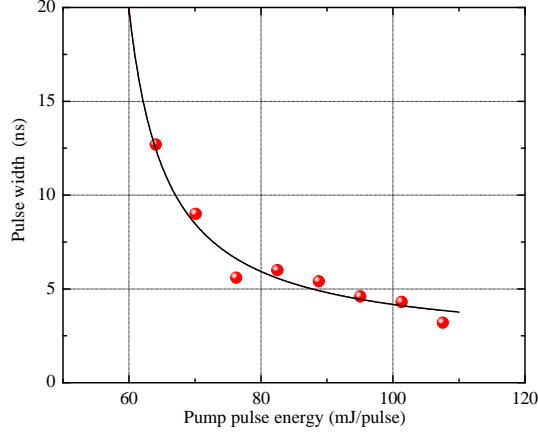Fig. 34. Ring cavity Ti:Sapphire pulse width as a function of pump power. The solid line shows the empirical dependence $\tau_{pulse} \approx \tau_{cavity}\left(1 + \frac{E_p^{th}}{E_p - E_p^{th}}\right)$ and is given to guide the eye. τ_{cavity} is the cavity lifetime given by $\tau_{cavity} \approx \frac{nL}{c(1 - R_1 R_2 R_3)}$, and E_p^{th} is the threshold pump energy. Here n represents the index of refraction of the gain media, L is the length of the cavity, c speed of light, R_1, R_2, R_3 reflectivities of cavity mirrors. The fit parameters are $E_p^{th} = 54.25$ mJ/pulse, and cavity lifetime $\tau_{cavity} = 1.9$ ns.

plore broad-band generation by molecular modulation [22]. The two injection seeded lasers demonstrate efficiencies of 37 %, and 35 % respectively. Their single frequency output is near diffraction limited and temporally smooth with pulse durations of around 5 ns.

D.   Vacuum system

A vacuum setup was build that allows the connection of a 1 m long Raman cell filled with deuterium at pressures from 1 Torr to atmospheric pressure. The vacuum system consists of a 1 m long cell with glued fused silica windows at Brewster angle, in order to avoid strong back reflections, a fore pump, one digital pressure reader that allows reading of pressures less than 1 atm, and a Bourdon manometer that allows

pressure readings above 1 atm. The system includes a mixing evacuation chamber for mixing of deuterium with nitrogen for safety reasons. The vacuum system allows the connection of different gas cylinders and different Raman cells (high pressure cell, or hollow fiber).
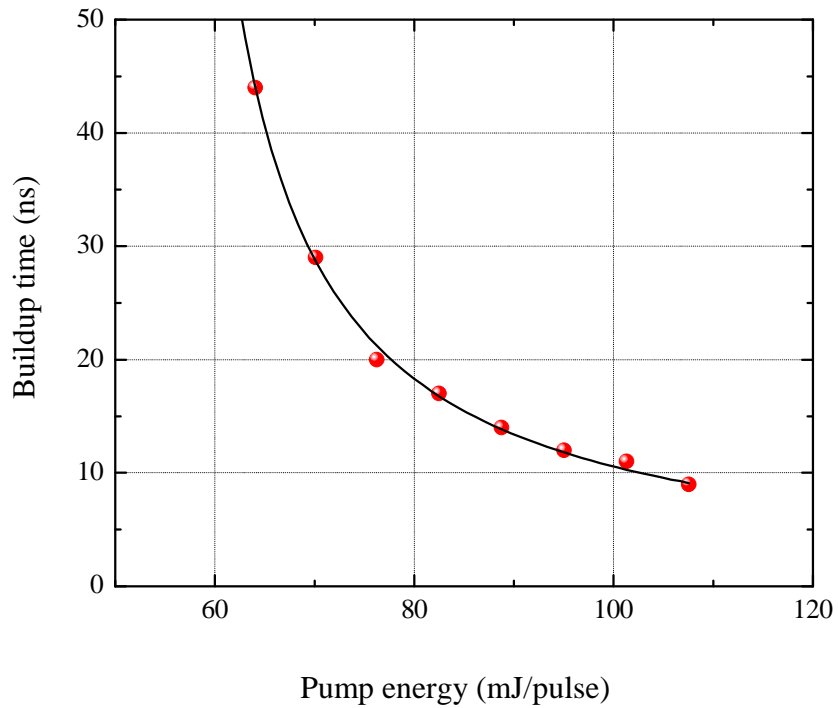
Fig. 35. Build-up time of seeded pulses Ti:Sapphire ring cavity as a function of pump power. The solid line gives the empirical dependence of buildup time $\tau_b \approx b\tau_{cavity}\frac{E_{th}}{E-E_{th}}$ where τ_{cavity} represents the lifetime of the cavity, and E_{th} represents the threshold energy [6]. Fitting parameters values are $E_p^{th} = 53$ mJ/pulse, cavity lifetime $\tau_{cavity} = 1.9$ ns, and $b = 5$.

CHAPTER V

RAMAN GENERATION IN HOLLOW FIBER

A. Introduction

As described in previous work [22], molecular modulation technique is essentially a technique in which it is possible, by adiabatically driving a Raman medium, to generate a wide, phase coherent, equidistant spectrum. Control of adiabaticity is achieved by detuning of the frequencies of driving lasers by a small two photon detuning. There are several requirements for efficient generate such broad spectrum. Among them, a high enough intensity of driving fields of order of several GW/cm^2 must be achieved. A good quality of transverse beam profiles of driving fields is also important for efficient spatial overlap. In addition, the interaction length has to be increased, since the generation process is proportional to the product of density and length.

It is well known that focusing of laser beams in free space is restricted by Rayleigh range [6]. For a laser beam with a spot size w_0 at the beam waist, Rayleigh range is defined as the distance z_R at which the diameter of the spot size increases by a factor $2^{1/2}$ and is given by:

$$z_R = \frac{\pi w_0^2}{\lambda} \tag{5.1}$$

with λ being wavelength in vacuum. The intensity of laser beam is approximately constant then over a range equal to twice Rayleigh range. For low energy of driving fields, focusing to a smaller size in order to maintain the necessary intensity will reduce interaction length, and in consequence will reduce the efficiency of the generation process.

One solution for achieving high intensity at lower power of input fields, while maintaining a long interaction length and a good quality of beam profile could be the

use of hollow waveguide.

Hollow waveguides are a good alternative to solid core fibers because the air filled core that allows a high laser threshold power, together with low insertion loss, no end refection and small beam divergence. However, there are limiting factors in using of hollow waveguides as shown by [66]. These limiting factors come from losses that occur in transmission of waveguides due to bending (proportional to $1/R$, where R represents the bending radius) and losses proportional to $1/a^3$, where a is the bore radius. Marcantili and Schmeltzer [67] showed that for fused silica hollow waveguide the lowest loss mode corresponds to H_{11} mode and that the attenuation coefficient α of this mode is given by:

$$\alpha = \left(\frac{2.405}{2\pi}\right)^2 \frac{\lambda^2}{a^3} \text{Re}\left(\frac{1}{2}\frac{\nu^2+1}{\sqrt{\nu^2-1}}\right), \tag{5.2}$$

where λ is the wavelength in the gas medium filling the waveguide, ν is the ratio of the refractive indices of the cladding and the core material. All other higher order modes HE_{nm} experience losses given by attenuation coefficient [68] :

$$\alpha_{nm} = \left(\frac{u_{nm}^2}{2\pi}\right)^2 \frac{\lambda^2}{a^3} \left(\frac{n}{n^2+k^2}\right) \left\{\frac{1}{2}\left(1+\frac{n_d^2}{(n_d^2-1)^{1/2}}\right)^2\right\}, \tag{5.3}$$

where u_{nm} is the mth root of zero order Bessel function, a bore radius, λ wavelength and n and k are the real and imaginary part of the complex index of refraction of the waveguide. It is easy to see that waveguide losses will increase as the bore radius is decreased, an effect which limits the bore size of the waveguide that can be efficiently used.

Despite of these deficiencies of waveguides, they still remain a better alternative for Raman generation than focusing in free space. This is clearly seen if one compares focusing in free space and focusing in hollow waveguides by using a figure of merit $F_{om} = \frac{\lambda L_{\text{int}}}{A_{eff}}$. Here A_{eff} and L_{int} are an effective interaction cross section and length.
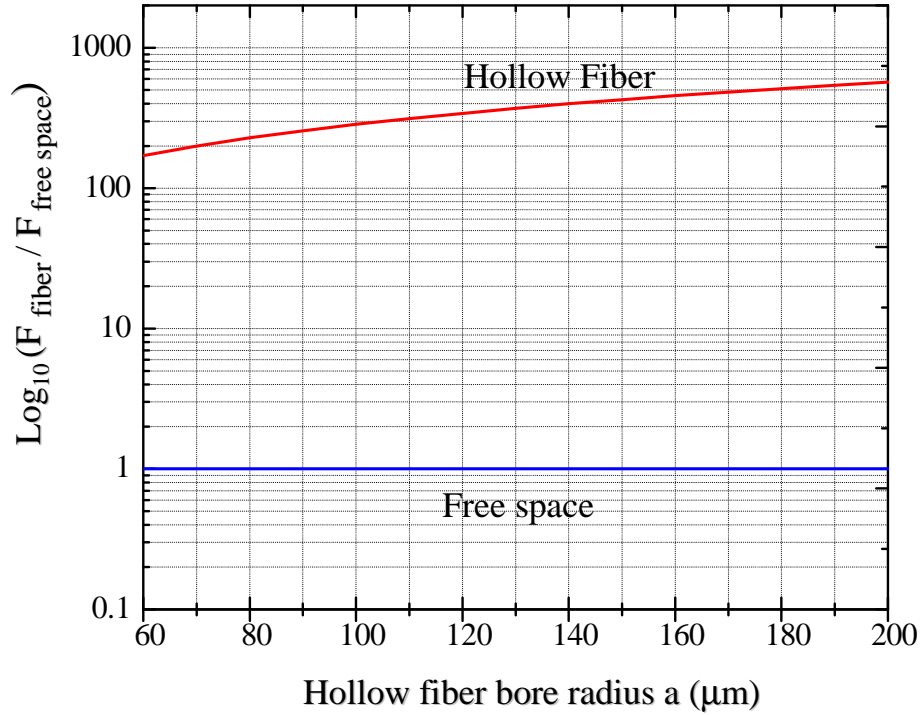
Fig. 36. Comparison of figure of merit for focusing in free space and hollow waveguide on a logarithmic scale, showing that use of hollow waveguides is 500 times more effective than use of free space beam.

For focusing in free space, this figure of merit is around 2, whereas for focusing in hollow waveguide this takes the value:

$$F_{om} = \frac{6.8a\left(n^2 - 1\right)}{\lambda\pi\sqrt{n^2 - 1}},\tag{5.4}$$

with a being the bore radius and n index of refraction of glass.

Figure 36 shows a comparison of focusing of laser beam in free space (bottom) and fused silica hollow waveguide (top) for a wavelength of 800 nm. It can be seen that for example, waveguides with bore radius of 160 μm are 300 times more effective than focusing in free space.

As shown previously [68], coupling into lowest order waveguide mode H_{11} is

desirable, since this gives the lowest loss. Transmission through a length z of fiber will be the result of coupling efficiency in a particular mode H_{1m} and attenuation and given by:

$$P_z = \sum_m \eta_{1m} Exp\left(-2\alpha_{1m}z\right),$$ (5.5)

where α_{1m} is the attenuation coefficient given in Eq. 5.3 for $n = 1$, and η_{1m} describes coupling efficiency in particular mode H_{1m}. This coupling efficiency can be described by the following expression [68]:

$$\eta_{1m} = \frac{\left(\int\limits_0^a Exp\left(-\frac{r^2}{\omega^2}\right) J_0\left(u_{1m}\frac{r}{a}\right) rdr\right)^2}{\int\limits_0^\infty Exp\left(-\frac{2r^2}{\omega^2}\right) rdr \int\limits_0^a J_0^2\left(u_{1m}\frac{r}{a}\right) rdr}.$$ (5.6)

Here ω is the beam waist at an intensity equal to $1/e^2$, and J_0 represents the zero order Bessel function. This equation allows to find optimal coupling efficiency for H_{1m} mode as a function of the beam waist to bore radius ratio ω/a. To achieve for example efficiencies $\eta_{11} = 98\%$ and $\eta_{12} = 0.5\%$, an optimum ratio $\omega/a = 0.64$ must be used.

Optimization of conditions for an efficient Raman generation involve also optimization of gas pressure, since group velocity dispersion of the medium may be different for frequencies of driving fields and generated comb. The idea is to minimize the combined dispersion of the gas and waveguide and reduce the group velocity dispersion of generated sidebands in the region of interest. Dispersion in a Raman gas media is given by

$$n_{gas} = 1 + \frac{1}{2\pi\varepsilon_0 c}\hbar N\omega_q a_q \lambda_0,$$ (5.7)

where ε_0 represents permittivity of vacuum, N number of molecules per volume, ω_q frequency of the qth sideband, λ_0 is wavelength in vacuum, a_q is dispersion coefficient for the generated qth sideband, and c is the speed of light in vacuum. For waveguide,
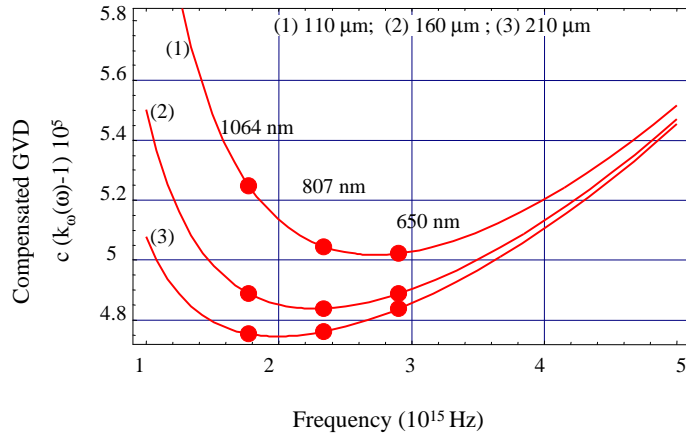
Fig. 37. Compensation of group velocity dispersion GVD between 650 nm and 1064 nm for three different bore radii of waveguide at a given pressure of 450 Torr. For waveguide radius of 160 μm, compensation is optimum.

dispersion depends on both propagating wavelength λ and bore radius a:

$$n_{WG} = 1 - \frac{1}{2}\left(\frac{1.2\lambda^2}{c\pi^2 a}\right)^2. \tag{5.8}$$

Ultimately, compensating the group velocities of media and waveguide reduces to adjusting the medium concentration for a given bore radius. In Fig. 37 compensation of group velocity dispersion in the region of our interest from 650 nm to 1064 nm is shown for three different bore radii (1) 110 μm, (2) 160 μm, (3) 210 μm at a given pressure of 450 Torr. GVD is approximally constant within our wavelength range for a bore radius of 160 μm. Once the geometry of the waveguide is fixed, optimum pressure (i.e gas concentration) can be calculated. Figure 38 shows three different group velocity curves in the region 650 nm to 1064 nm for three different pressures with a fixed waveguide geometry (bore radius) of 160 μm.

As it was previously shown in [69], use of collinear rotational Raman generation has significant advantages over vibrational generation. Among them, a smaller repetition rate of pulse trains could allow for single pulse selection. We are therefore
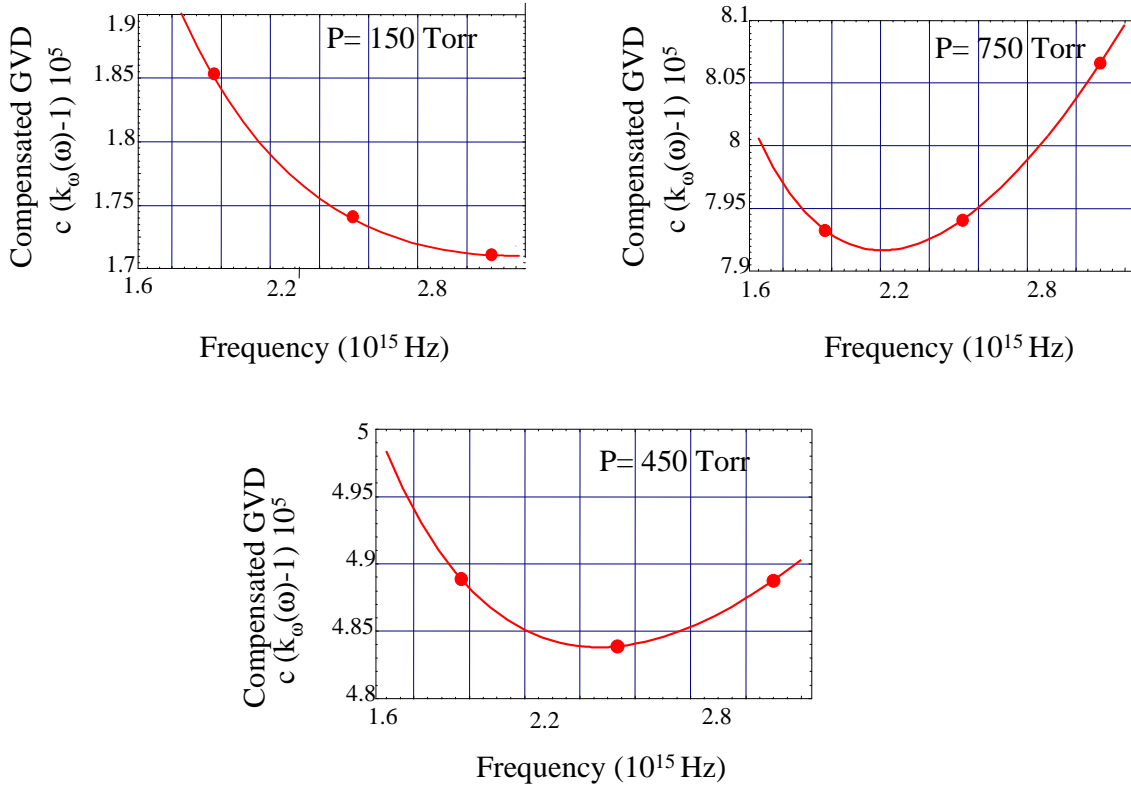
Fig. 38. For a fixed waveguide geometry, there is an optimum pressure that compensates for group velocity dispersion GVD. Here the waveguide radius is 160 μm and the optimum pressure corresponds to 450 Torr in the region of interest 650 nm to 1064 nm.

choosing to drive $v'' = 0, J'' = 2 \rightarrow v' = 0, J' = 4$ transition in molecular deuterium with two nanosecond transform limited Ti:Sapphire lasers at wavelengths 782.33 nm and 807.56 nm. Their tunable frequency difference is approximately equal to the transition from second excited rotational state of ground state to the fourth excited rotational state, as shown in Fig. 39. At room temperature, the population of $J = 2$ state is 42%, whereas 66% of population is found in $J = 0$ state at liquid nitrogen temperature, as it can be seen in Fig. 40.
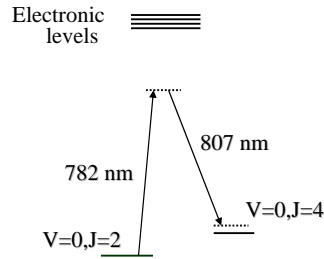
Fig. 39. Schematic of rotational energy levels in deuterium. A pair of lasers (807 nm and 782 nm) drive the $v'' = 0, J'' = 2 \rightarrow v' = 0, J' = 4$ transition. The frequency difference of the driving lasers is slightly detuned from Raman resonance to allow adiabatically preparation of molecules in a superposition state.

B. Hollow fiber experimental setup

Our experimental setup is shown in Fig. 41. Two Ti:sapphire lasers are synchronized and combined on a beam splitter and send into a deuterium filled hollow fiber at pressures between 300 - 750 Torr. The light produced in the cell is dispersed by a pair of fused silica prisms and projected onto white screen. Both lasers are home-build injection seeded from an external-cavity laser diode and pumped by the second harmonic of same Quanta Ray Q-switched Nd:YAG laser. Their output energies and pulse durations are comparable : 16-18 mJ/pulse with pulse durations of about 4.7 ns. As mentioned in previous chapter, a larger molecular coherence can be established by driving a Raman transition with narrow line-width (bandwidth-limited) laser pulses with duration shorter than the dephasing time. To demonstrate the advantages of using shorter pulse durations, we illustrate in Fig. 42 the collisional dephasing time of $S_0(2)$ transition. Using driving fields with pulse durations of 5 ns allows us to work at larger pressures, (where generation process is more efficient), and at the same time to maintain a large molecular coherence.
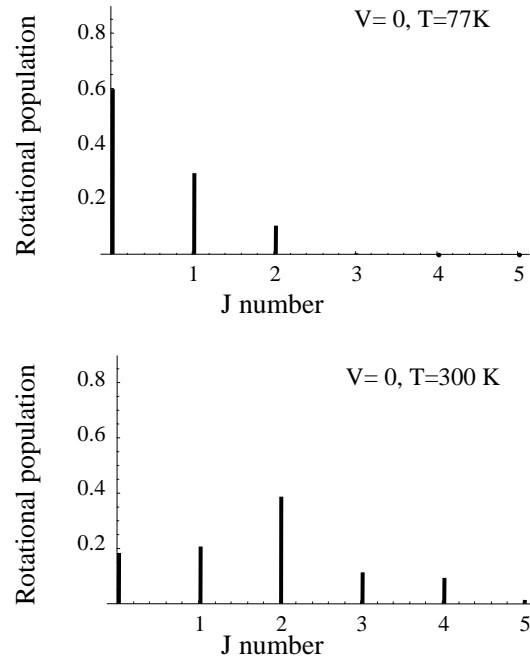
Fig. 40. Population distribution of different rotational levels indicated by J number for ground vibrational state $v = 0$ at room temperature 300 K (bottom) and liquid nitrogen temperature (top) of 77 K in deuterium. At room temperature 42 % of the population is the $J = 2$.

The two lasers are synchronized by building a delay line for 807 nm laser and "fine tuned" by adjustment of pumping power of linear cavity, hence adjustment of buildup time of pulses from linear cavity. The temporal overlap of beams was monitored with a home made fast photo detector and 1 GHz (5 GS) Tektronix TDS 684C oscilloscope.

All beams are linearly polarized, with polarizations in the horizontal plane. At the output of linear cavity, polarization of output beam is rotated by 90 degrees from vertical to horizontal by a $\lambda/2$ plate.

Since their wavelengths are so close (807 nm and 782 nm), there are no commercially available dichroic beam splitters that will allow simultaneously good transmis-
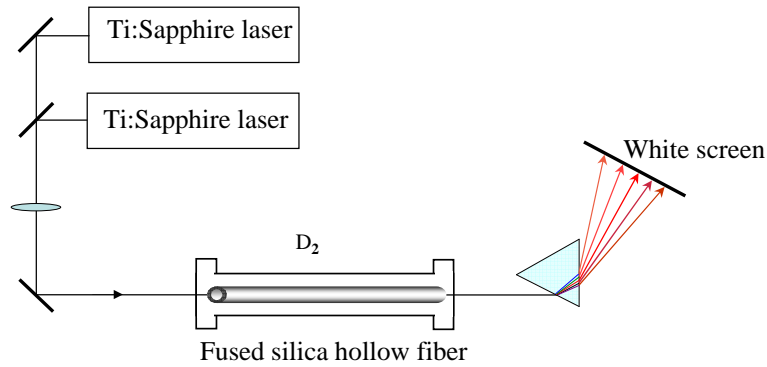
Fig. 41. Experimental setup for Raman generation in hollow fiber with two Ti:sapphire lasers.

sion and reflection of both beams without significant losses. However, we found that using an Alexandrite CVI mirror CVI ALX-1037 allows us to reflect 90 % of 782 nm laser and transmit 85 % of the 807 nm beam.

A 500 mm IR coated lens was used for focusing of both beams to a spot size of 117 μm for 807 nm beam, while size of 782 nm beam was measured to be 139 μm. Both beams were measured by knife edge technique. Due to the long delay line of the 807 nm beam, an extra pair of lenses with focal lenses of 500 and -200 mm were used in order to adjust the focal point and divergences of the two beams at the entrance in the fiber.

The fused silica waveguide was laying on a steel V groove, and metal weights were placed on top on it in order to prevent fiber from bending, thus introducing losses. The V groove was incorporated into a steel chamber with Brewster angle fused silica windows and viewports at the entrance and exit of fiber, for monitoring of the steering of two beams into fiber. Positioning of the V groove with the fiber was done by placing the whole system on two translation stages that allowed translation in both vertical and horizontal directions.

Special care had to be taken of fiber cleaving. Bending or twisting the fiber
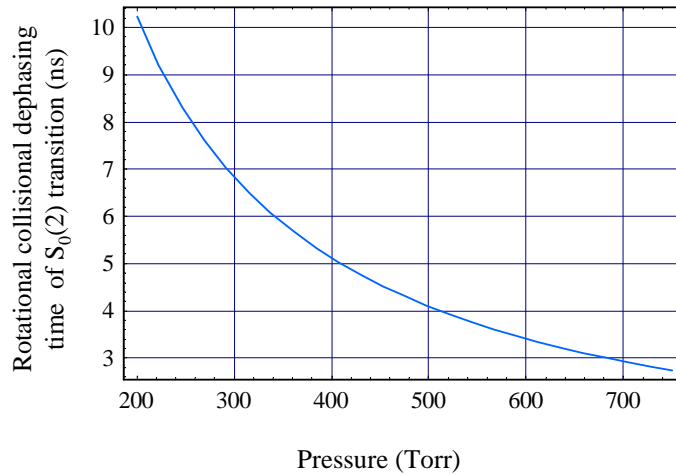
Fig. 42. Calculated rotational dephasing of $S_0(2)$ transition in deuterium using data from Ref. [70]. Using driving fields with pulse durations of 5 ns allows us to work at larger pressures, (where generation process is more efficient), and at the same time to maintain a large molecular coherence.

during cutting could induce fracture that could propagate along the length of the waveguide. In addition, crushing the ends of fiber results in poor coupling and poor propagation of beams in the waveguide. The polymicro coating that protects the fiber was removed by burning over a length of 1 cm at the front end of fiber for better steering of beams. It is important that the fiber is kept as clean as possible from any dust, since small pieces of dust will burn and destroy the waveguide when high intensity laser beams are coupled in. The two lasers where coupled into waveguide by coupling first their seed beams, and maximizing the output with a powermeter. Coupled seed beam profile was monitored at the output so that it corresponds to the lowest order mode H_{11}. Coupling of 782 nm laser was done by using the two translation stages, while 807 nm was steered into fiber by two mirrors placed before the combining beam splitter. Coupling efficiencies of seed beams were 70 %, and 64 %. In Q switch, the energies of transmitted beams were 2.8 mJ/pulse for 782 nm
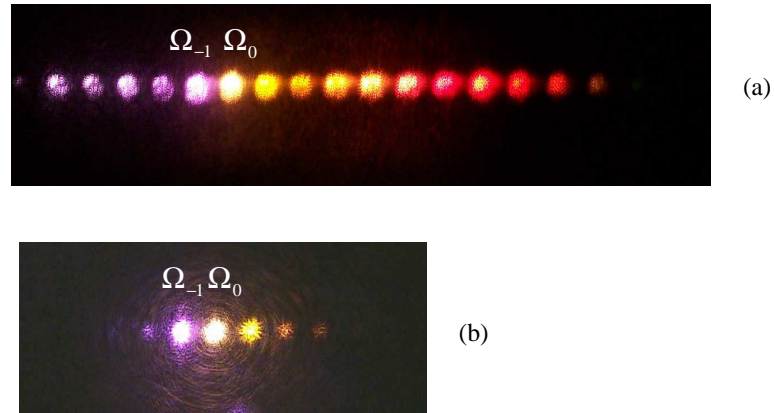
Fig. 43. Rotational spectrum in deuterium. Figure (a) shows the spectrum generated in a hollow fiber, while picture (b) indicates Raman spectrum generated in free space. Driving fields are indicated in both (a) and (b) by Ω_0 and Ω_{-1} respectively.

beam, and 1.6 mJ/pulse for 807 nm. Pulsed coupling efficiencies were lower than those for the corresponding seed beams, due to a worse beam profile in this regime. Assuming that the coupling was into lowest order mode, the intensities of two beams inside the waveguide were 1.72 GW/cm^2 for 782 laser, and 1.1 GW/cm^2 for 807 laser. For comparison, the same experiment was repeated by focusing the two beams in free space using a Raman cell of same length at the same pressure. Focused beam sizes were measured to be 230 μm for 782 laser with an energy of 5.5 mJ/pulse and 265 μm for 807 nm laser, with a corresponding energy of 8.6 mJ/pulse. Focusing in free space gives an intensity of 0.66 GW/cm^2 for 782 laser, and 0.77 GW/cm^2 for 807 nm laser. It is easy to see that the use of hollow fiber improves the efficiency of Raman process.

Dispersed output of the fiber is presented in Fig.43. For comparison, we present in Figure (a) rotational spectrum generated in hollow fiber, and in free space (Figure(b)). Driving fields are indicated by Ω_{-1}, and Ω_0, where we kept the same notation as in,

for example Ref.[22]. Pressure was set to 704 Torr.

Figure 44 indicates rotational spectrum in deuterium as taken by an Ocean Optics SAS HR4C527 spectrometer. The range of this spectrometer corresponds to a region between 650 nm-900nm, and due to its limited range some of the generated sidebands are not shown. As shown previously [22], subfemtosecond pulse compression by rotational modulation can be achieved. The repetition rate of such trains will be equal to the modulation frequency, or difference between driven energy levels plus or minus a small detuning. In our case, pulse trains with repetition rate 12.4 THz can be achieved by tuning below Raman resonance.

C. Conclusion

We have demonstrated a new method of improving the efficiency of Raman generation by molecular modulation in a hollow waveguide. Using the hollow fiber we were able to extend the interaction length to more than twice Rayleigh range, while keeping a low power of driving fields. This method can be extended to efficient generation of Raman sidebands with frequency spacing equal to vibrational frequency in other molecular gases.
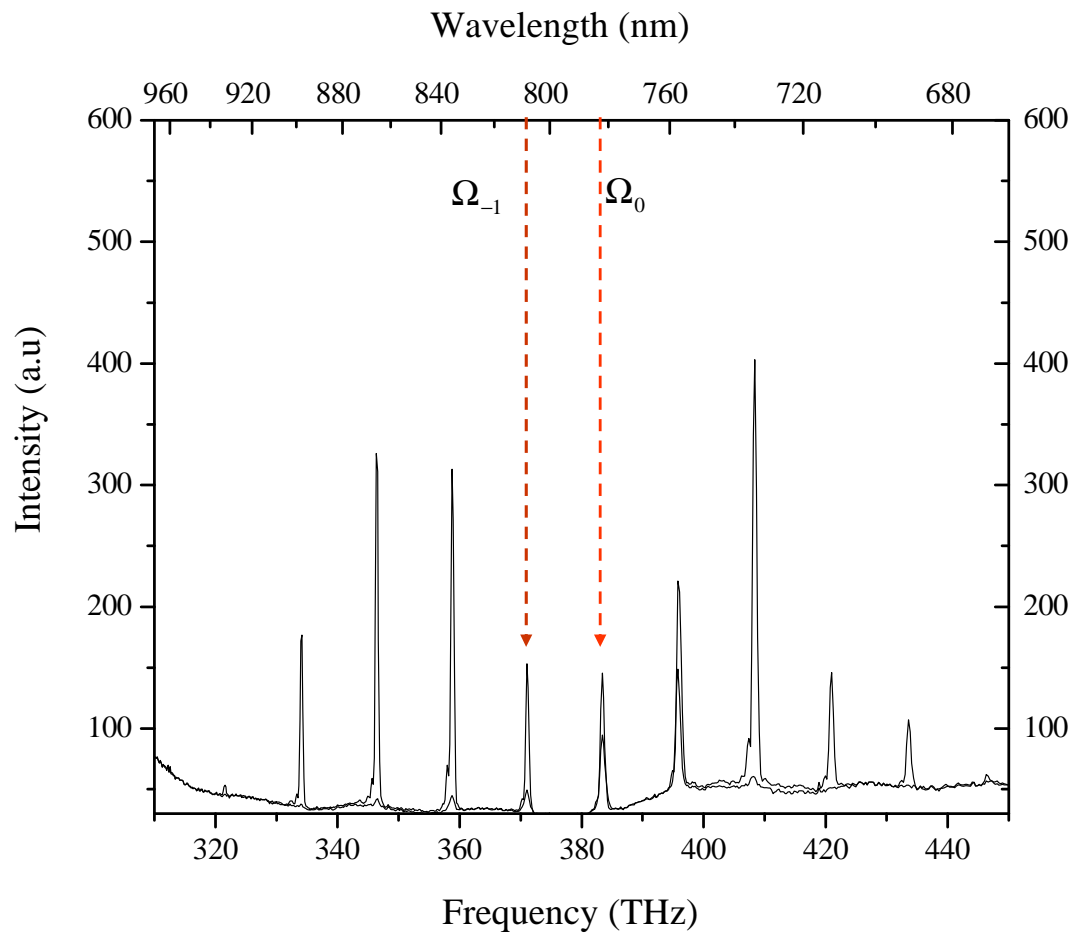
Fig. 44. Rotational Raman generation in deuterium. Driving fields are indicated by Ω_{-1}, and Ω_0. Due to limited range of the spectrometer not all the generated sidebands are displayed.

CHAPTER VI

ROTATIONAL AND VIBRATIONAL RAMAN GENERATION WITH TWO FIELDS

While the previous proposed idea (use of hollow fiber) will allow a more efficient Raman generation, an increase in the spectral density of generated comb is desired for a better control over the electric field under the envelope. Our theoretically proposed Raman additive technique can be implemented by applying two independent tunable lasers, together with additional fields obtained by harmonic generation and frequency mixing. A related idea of obtaining a multiplicative increase in the number of the sidebands has been investigated theoretically [23] and very recently experimentally [32]. That technique was based on the use of modulators in series that allowed generation of a large number of non-equidistant sidebands in a cell filled with different species.

The experiment that we describe in this chapter is essentially the same as one described in Ref. [24]. We have observed simultaneous rotational and vibrational Raman generation in deuterium gas, with only two laser pulses applied at the input of the molecular cell. Only the fundamental vibrational transition $Q_1(0)$ is driven strongly in this experiment. (For a better understanding of spectroscopic notation of different Raman transitions, we illustrate in Fig. 45 standard notation of different Raman transitions). However, in addition to efficient vibrational Raman generation we observe generation of a large number of rotational sidebands corresponding to $S_0(0)$ transition. We have investigated the temporal, spatial, and angular beam overlaps, on generation efficiency and transverse beam quality. To our surprise we observed that under certain conditions strong vibrational Raman generation leads to efficient rotational generation, while under different conditions the vibrational Raman
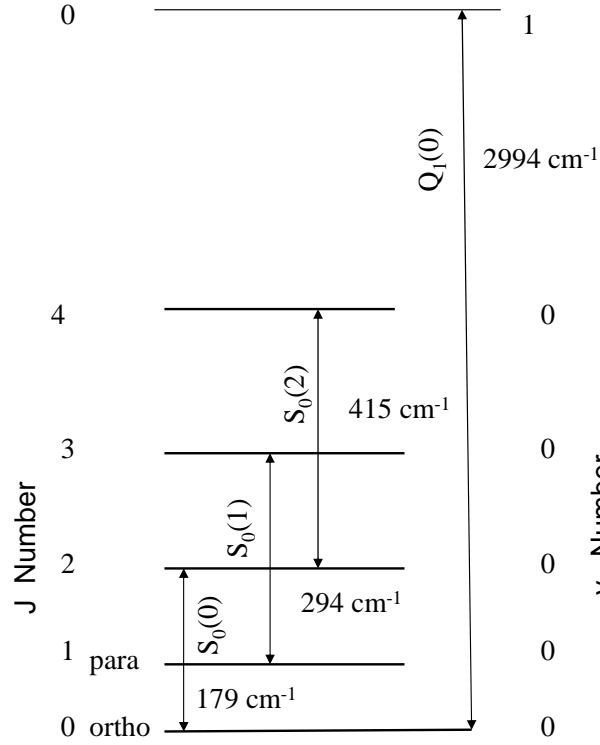
Fig. 45. Energy diagram of different Raman transitions in deuterium. The only transition driven in our experiment is $Q_1(0)$. In addition, numerous lines corresponding to $S_0(2)$ transition are seen around the generated vibrational lines.

generation may suppress a self-starting stimulated rotational Raman generation.

A.   Previous work

Stimulated Raman scattering SRS has been an extensively studied subject due to its potential applications such as frequency conversions or multiple wavelength generation. Raman scattering can be described by inelastic scattering of a laser beam in a medium which results in either up converted frequencies (anti-Stokes lines) or down converted frequencies (Stokes lines) shifted by a rotational or vibrational energy amount in a molecule. If the intensity of the laser beam is sufficiently high, then this leads to an exponential growth of the total scattered light [71], and consequently to

stimulated Raman scattering.

Different media (gas, solids, or liquids) in different time regimes of laser pulses have been employed to investigate this effect [72, 73, 74, 75]. Particularly interesting for our work is the generation of rotational SRS arising from $S_0(0)$ transition in deuterium at liquid nitrogen temperatures by the second harmonic of a Nd:Yag laser [76]. However, the pressure used in this experiment is very high (8 atm), which is consistent with normal conditions in which stimulated Raman scattering occurs.

Other work reported the use of single dye laser operating at two different wavelengths separated by roughly the energy difference between two rotational lines in hydrogen [77] for generation of around 40 lines through a two color induced stimulated Raman effect. By introducing the two color laser beam, the threshold of rotational generation was greatly reduced. In further work, the same team maximized the number generated lines by tuning this time the frequencies of two lasers to match exactly the frequency difference of rotational transition in hydrogen [78]. The Stokes and anti-Stokes lines were generated by the combined effects of stimulated Raman scattering and four wave mixing (FWM) in a phenomenon called Stokes cascading. Since the two color induced Raman spectra consisted of equidistant lines, a mechanism of generating ultrashort laser pulses was suggested later [79]. As a first step towards achieving this goal, Imasaka' s group [80] generated a pure rotational comb, effectively suppressing vibrational generation by optimizing gas pressure, focusing conditions and polarization of their two lasers. Enhancement of rotational SRS was shown by operating at low pressure of Raman medium while larger pressures favored vibrational generation. In addition, the use of circularly polarized pump beams was found beneficial for rotational stimulated Raman scattering.

A vast literature covers various theoretical aspects of SRS since the original description of this process in the early 1960' s [72]. Relevant aspects to our experiment

are presented below.

There are two different time regimes in which stimulated Raman scattering can take place. One is the transient regime, in which pump pulse duration is less or roughly equal to the lifetime of the coherent state phonons (optical for SRS) and the other one is so called steady state regime, where pulse duration is larger than the dephasing time $1/(\pi\Gamma)$ with Γ being the line width of Raman transition.

It is common to define the threshold of SRS as the point where the exponential gain reaches the value of $G = e^{30}$ or when intensity of generated Stokes represents 1% of intensity of pump light [81].

For gases, the plain wave gain coefficient is given in steady state regime by:

$$g = \frac{2\lambda_s^2}{h\nu_s} \frac{\Delta N}{\pi\Delta\nu} \frac{\partial\sigma}{\partial\Omega},$$ (6.1)

where ΔN is the population difference between the two states given by $\Delta N = N(0, J) - \frac{2J+1}{2J'+1} N(v, J')$ with N number density in an individual vibrational rotational state, ν_s is Stokes frequency, $\frac{\partial\sigma}{\partial\Omega}$ is Raman differential cross section for a particular polarization used in the experiment, and $\Delta\nu$ is full width at half maximum (FWHM) Raman line-width in Hertz. The wavelength dependence of this gain coefficient comes from the Raman cross section, while the temperature and pressure dependence (density) comes from changes in the Raman line-width. Dependence of Raman gain on pump wavelength is quite substantial. As it was shown in [82], as much as 20 times larger Raman gain in hydrogen gas results when the fourth harmonic of a Nd:Yag is used as pump as opposed to the fundamental beam 1064 nm. The estimated plane wave steady state gain coefficient for SRS in our experiments is 9.6 10^{-9} cm/W at a pressure of 300 Torr and temperature of 77 K, and pump wavelength corresponding to 1064 nm. In transient regime, transient Stokes gain can be approximated by:
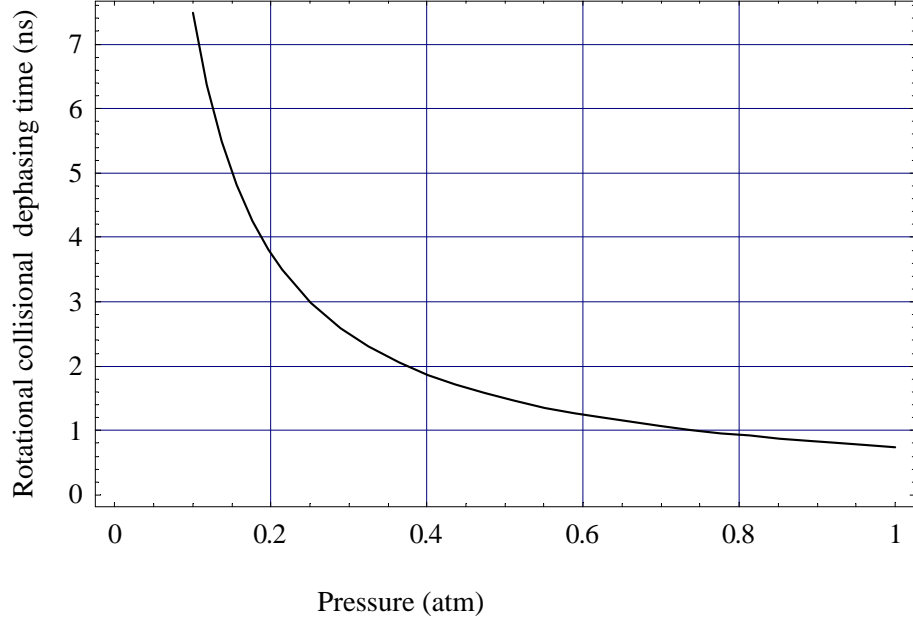
Fig. 46. Dephasing time of $S_0(0)$ for D_2 at 77 K as a function of gas pressure, as calculated using data from Ref. [70].

$$\frac{G(l,t)}{G(0,t)} = \exp\left[\left(\frac{gI_llt}{\tau}\right)^{1/2} - \frac{t}{2\tau}\right], \tag{6.2}$$

where g is the steady gain coefficient defined above, I_l is the laser pump intensity and τ is the phonon lifetime.

From data available in literature, the optical phonon lifetime for example is 8 ns for hydrogen at 100 K temperatures and pressure of 0.1 atmosphere for $Q_1(1)$ Raman transition, experiencing a decrease of about 1 ns around 0.6 atm due to Dicke narrowing for the same temperature [83]. The line widths for rotational Raman lines in hydrogen and deuterium are Doppler limited below 0.01 atm pressure, with collisional narrowing occurring between 0.01 atm and 1 atm and pressure broadened above 1 atm [84]. For $S_0(0)$ we have calculated the collisional linewidth in deuterium at 77 K in our pressure range from 0.1 and 1 atm and temperature 77 K using the
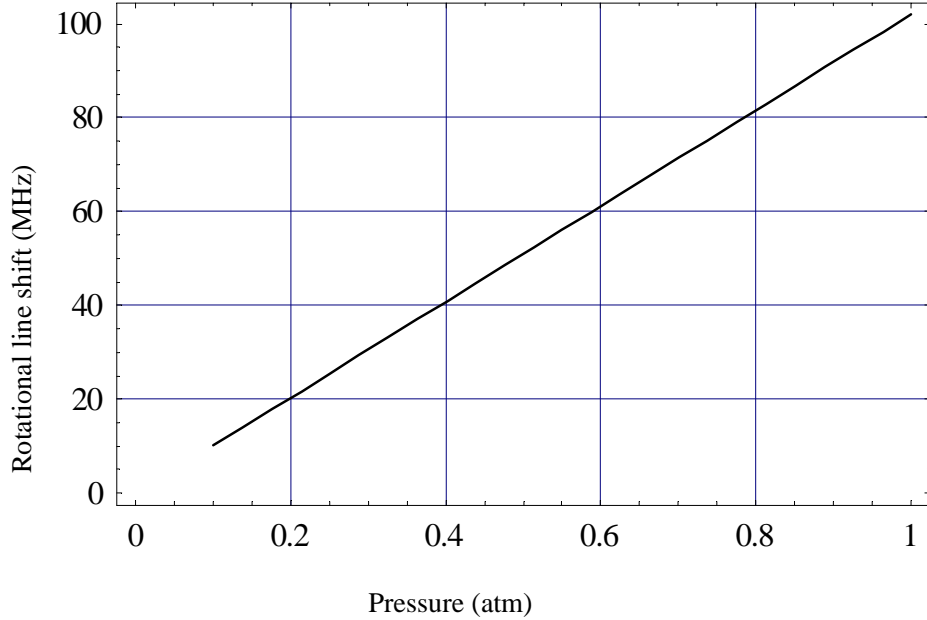
Fig. 47. Calculated line shift of $S_0(0)$ for D_2 at 77 K as a function of gas pressure using data from Ref. [70].

data from [70]. Fig. 46 shows the corresponding dephasing time of this transition as a function of pressure. In addition, line shifts of same transition are shown in Fig. 47 as a function of pressure. The lineshift is taken as the difference between the central line frequency at density ρ and frequency at zero density, with negative line shifts occurring in the case when Raman line moves away from the exciting frequency with increasing density [70].

To establish the time regime of our experimental conditions, one can compare the lifetime of optical photon for $S_0(0)$ (dephasing time) with pump pulse duration. From Fig. 46 one can conclude that our pump pulse durations of less than 10 ns are comparable with dephasing time, and therefore transient time regime should be applied.

The Raman gain in the transient regime is lower than steady state gain by a
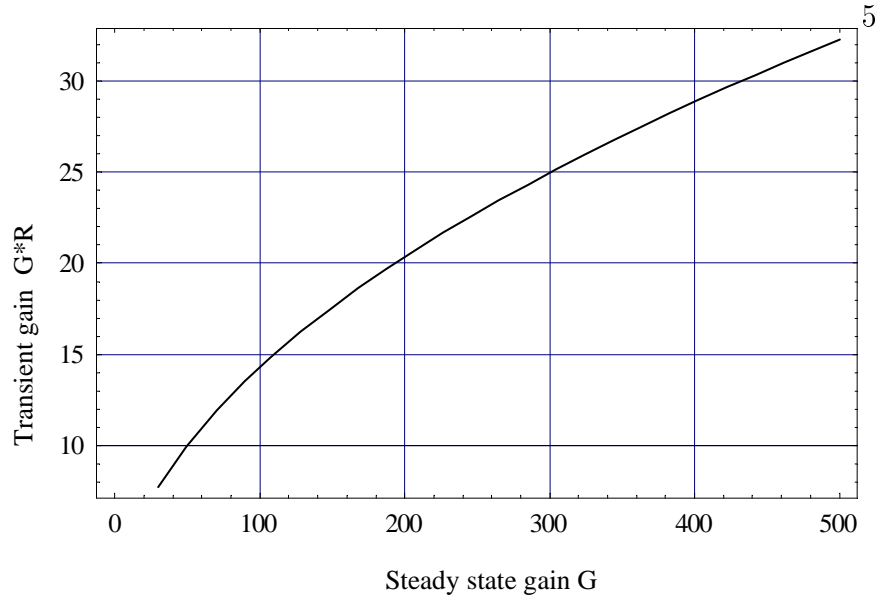
Fig. 48. Transient gain $G \times R$ as a function of steady state gain G for rotational transition $S_0\,(0)$ in D_2 at 77 K and 1 atm pressure with pump pulse duration of 10 ns.

reduction factor R [85], but this gain can be increased with pressure. Following [82], the reduction coefficient R is described by:

$$R = \frac{1}{\sqrt{G}} \left(\sqrt{t_p \Gamma} - \frac{1}{4\sqrt{G}} \right), \qquad (6.3)$$

where t_p is pump pulse duration and Γ is the linewidth of Raman transition. We illustrate in Fig. 48 behaviour of transient gain $G \times R$ versus steady state gain G for rotational transition $S_0\,(0)$ in D_2 at 77 K and 1 atm pressure with pump pulse duration of 10 ns.

Focusing geometry influences greatly the SRS process. In steady state regime and for a laser beam with an M^2 factor greater than one, gain depends on the focusing geometry [86], as:

$$G \cong \frac{4g \frac{P_p}{M^2} ArcTan\left(\frac{l}{b}\right)}{\lambda_s + \lambda_p}, \qquad (6.4)$$

where l is length of the gain medium, b confocal parameter of the focused laser beam (twice the Rayleigh range), λ_p and λ_s wavelengths of Stokes and pump beam, and g plane wave gain coefficient. According to the above expression, a tight focusing will be desired, since the value of $ArcTan\left(\frac{l}{b}\right)$ approaches $\pi/2$. Despite of this, much lower thresholds of SRS were found [87] using a looser focusing by a longer focal length lens. This effect was attributed to a gain suppression due to stronger Stokes and antiStokes coupling with a tight focusing geometry [88]. The gain suppression in the case of non-resonant SRS occurred when the angles of exact phase matching condition for Stokes and antiStokes were maintained within confocal volume of pump beam [89]. Furthermore, same group [89] demonstrated experimentally that it is possible to enhance either pure rotational or pure vibrational SRS in hydrogen at the same pump energy and pressure of Raman gas. The enhancement of one transition or another was realized by proper focusing conditions which lead to parametric gain suppression of rival process.

As mentioned previously in the chapter, Stokes cascading can occur due to FWM. Several authors studied the FWM efficiency, and correspondingly the efficiency of Stokes cascading as well as ratio of Stokes to antiStokes energy. In Ref. [90] for example, efficiency of FWM was shown not only to increase proportionally with a tighter focusing, but also proportionally with FWM dephasing length $L_d = \pi/_{\Delta k}$, with Δk representing FWM wavevector mismatch. The significance of molecular population dynamics and transient effects was also studied in Ref. [91] in the case when pulse width is comparable with dephasing time of transition. Particularly interesting is the investigation of high pass single gain SRS and FWM in a focused geometry [82] for three different Raman gases: hydrogen, deuterium, and methane. It was pointed out that FWM makes the quality of Stokes beam profile worst, and that this effect becomes stronger for higher order Stokes lines due to increase in the number of FWM

processes necessary to create that particular Stokes line. It was also suggested that addition of a buffer gas such as He or Ar could result in an improvement of Stokes beam quality by increasing the wavevector mismatch.

At the same time, it was observed that parametric gain suppression does not take place when pump and Stokes beams are circularly polarized in opposite senses [92].

Lastly, but not least, one mechanism that tends to reduce the Raman gain is laser induced breakdown of the Raman active gas or buffer molecules [93]. The actual mechanism responsible for gas breakdown at pressures above 100 Torr and pulse durations greater or equal to nanosecond is electron avalanche generated by repeated inverse bremsstrahlung absorption [94]. Laser induced breakdown was studied in deuterium with 4 ns pulse durations for a pressure range of 100- 800Torr [95]. From dependence of threshold breakdown intensity versus pressure it was inferred that breakdown occurs due to to growth of inverse bremsstrahlung absorption which is unaffected by recombination or diffusion processes.

B. Experimental setup

The experimental setup is similar with the one in Ref. [24] and is presented in Fig. 49. Two lasers with a tunable frequency difference equal to vibrational frequency corresponding to $Q_1(0)$ transition in deuterium are send into a cooled Raman cell at pressures between 50 and 750 Torr at 77 K.

First laser is a transform limited Q-switched injection seeded Nd:YAG laser (Quanta-Ray 6350) with pulse duration of 12 ns. The output energy was attenuated by a pinhole to a maximum value of 240 mJ/ pulse at a repetition rate of 10 Hz. Line width of Nd:Yag laser was calculated to be $\delta\omega_{ND:Yag} \approx \frac{2Log(2)}{\pi t_p} \approx 36.7$
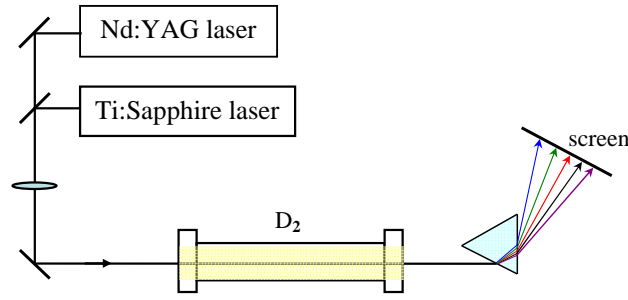
Fig. 49. Experimental setup for Raman generation in deuterium. $Q_1(0)$ vibrational transition is driven by two transform limited lasers with wavelengths 1064 nm and 807 nm. Their tunable frequency difference is approximately equal to vibrational frequency of 2994.6 cm^{-1}.

MHz. Second laser is a Q-switched injection seeded tunable Ti:Sapphire laser and its operation was discussed in Chapter V. When pumped 2.5 times about threshold, its output energy reaches 18 mJ/pulse with a pulse duration of about 5 ns and a linewidth $\delta\omega_{Ti:S}$ of about 90 MHz.

Both lasers are linearly p polarized, but the polarization of Ti:sapphire laser can be changed with the help of a $\lambda/2$ waveplate. Monitoring of wavelength is done with a WA 1500 Burleigh wavemeter (resolution of 10 MHz). Temporal syncronization of the two driving fields is achieved by building a delay line for 1064 nm laser. The two pulses are combined on a dichroic beamsplitter and focused by a 75 cm lens to spot sizes of 275 μm (807 nm laser) and 265 μm (1064 nm laser). Two extra pairs of lenses were used for 1064 nm and 807 nm beam for better adjustment of focusing points and beam sizes. Divergence of Ti:Sapphire laser was estimated to be 7.3 mrad, with a 2.7 mrad divergence corresponding to Nd:YAG laser. The two lasers are focused in the middle of a 1 m long Raman cell filled with deuterium at 300 Torr which is cooled to a temperature of 77 K. By cooling the cell to liquid nitrogen temperatures, we increase the population in the $J = 0$ state to 66 %, thus improving the Raman

generation process.

C. Experimental results

A bright white beam of light is observed to the output of the cell when the frequency difference of the two lasers is tuned to within 2 GHz from Raman resonance. When we disperse the beam by a pair of fused silica prisms, we observe that the spectrum does not consist only of lines corresponding to the pure vibrational transition that we are driving (as expected [22]), but rather numerous less intense lines appear around the main vibrational lines. This spectrum was recorded by an Ocean Optics HR 4000 with a resolution of 0.7 nm FWHM.

A typical spectrum is presented in Fig.50. The generated spectrum consists of lines corresponding to pure fundamental vibrational transition separated by 2994.6 cm^{-1} and rotational lines corresponding to lowest rotational transition $S_0(0)$ with separation frequency of 179 cm^{-1}. Rotational lines are obtained from stimulated Raman scattering from 1064 nm laser. We observe the onset of SRS with Nd:Yag laser only at pressures above 250 Torr, and energies above 180 mJ/pulse. As the pressure is increased further, a reduction in the energy of the pump beam is observed. This behavior is in agreement with Eq. 6.1, which predicts an increase of the plane wave steady gain coefficient with density.

We measured the intensities of Stokes (1084 nm) and anti-Stokes (1044 nm) at a 300 Torr pressure as a function of the applied pump 1064 nm pulse energy. These intensities are presented in Fig. 51, as measured by HR 4000 spectrometer, with background subtracted from plot. Filled circle points denote the first Stokes (1084 nm), while triangle points indicate the behavior of anti-Stokes lines. One can observe an exponential increase behavior indicated by solid line $y = Ae^{\frac{x}{x_1}}$ with
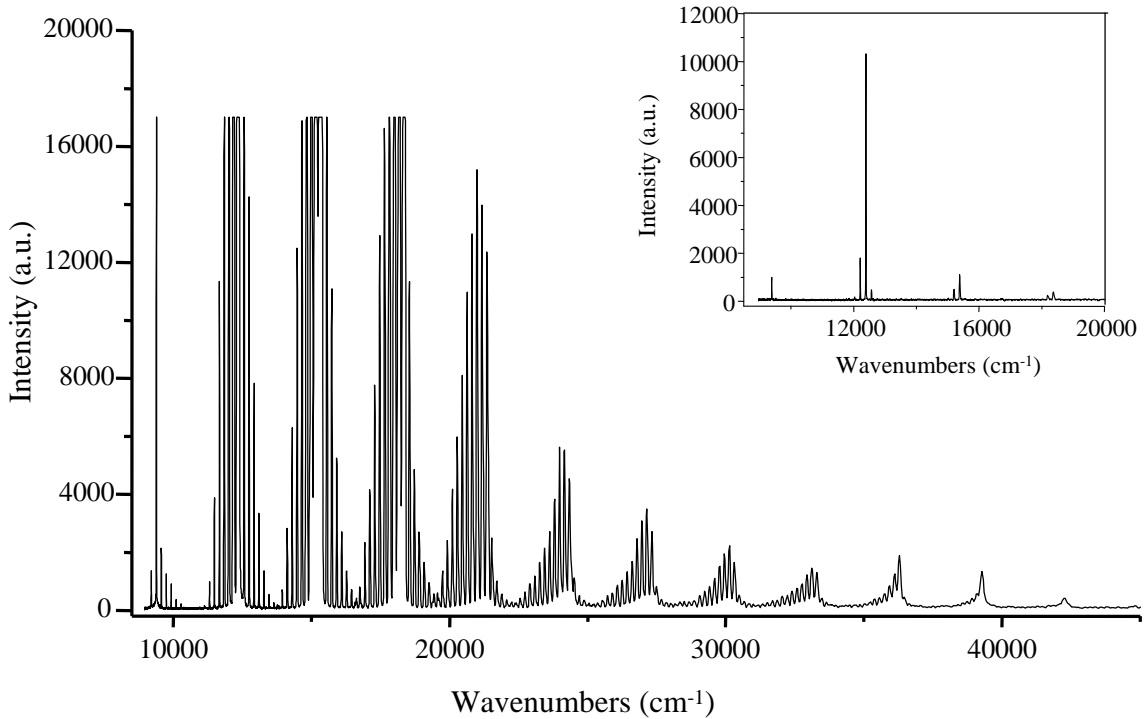
Fig. 50. D_2 spectrum obtained by a combination of molecular modulation as described in Ref. [24] (effectively driving Q_1 (0) vibrational transition) and SRS of S_0 (0) rotational transition. Detuning from Raman resonance is $\Delta\omega = 1.61$ GHz. 807 nm energy is 8 mJ/pulse, while energy of 1064 nm is 240 mJ/pulse at a pressure of 300 Torr. The insert shows the unsaturated spectrum obtained by reducing the intensity by a factor of 100.

$A = 0.12, x_1 = 30.25$, with a corresponding pump energy threshold of 160 mJ/pulse. As pressure is increased even further, a Stokes and anti-Stokes cascading process is observed. Due to the range of this spectrometer, Stokes cascading process is not observed fully, but an anti-Stokes SRS cascading spectrum is very well shown in Fig.52 at a pressure of 300 Torr and pump pulse energies of 240 mJ/pulse.

Going to even larger pressures results in an onset of SRS in the backward direction. For example at a pressure of 749 Torr, we observe that in addition to rotational Stokes at 1084 nm, stimulated vibrational line appears at a wavelength of 830 nm.
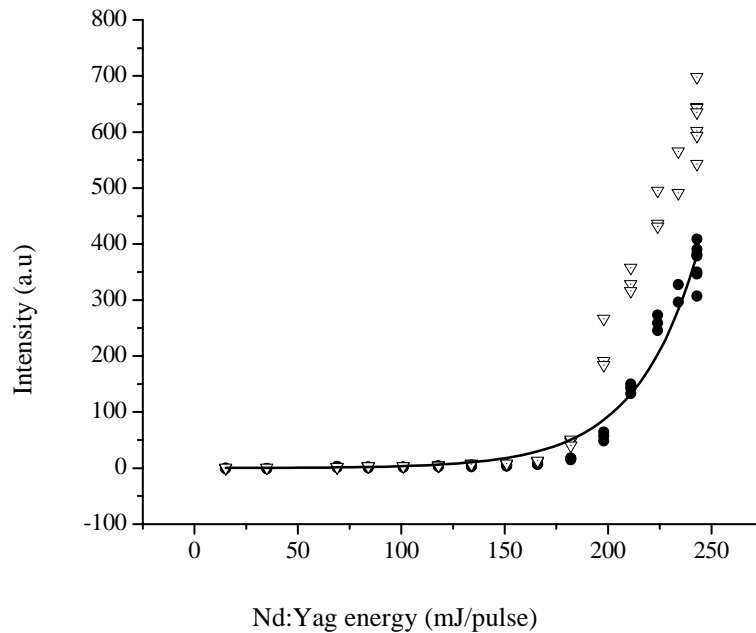
Fig. 51. First Stokes (filled circles points) and antiStokes (triangle points) intensities arising from $S_0(0)$ rotational transition as a function of the Nd:Yag 1064 nm pump energy. Intensities of Stokes and antiStokes fields are measured at the exit of cell by sending a small reflection to a HR 4000 spectrometer and subtracting the background. Pressure of gas is 300 Torr at a temperature of 77 K. Solid line represents the exponential growth fit of Stokes intensity $y = Ae^{\frac{x}{x_1}}$ with $A = 0.12, x_1 = 30.25$

.

This behavior is shown in Fig. 53. Rotational Stokes is indicated by $S(1)$, while vibrational rotational anti-Stokes is labeled as $AS_{vib-rot}(1)$. The corresponding vibrational rotational Stokes $S_{vib-rot}(1)$ should also be present in the backward direction, but is not observed within spectrometer's range. Cascading Stokes and anti-Stokes is observed forward corresponding to pure rotational transition $S_0(0)$. However, with time, the forward rotational SRS and backward rotational vibrational SRS stops, pump profile changes suddenly, showing a strong depletion with a somewhat steeper back edge temporal profile as shown in Fig.54. An additional side effect that occurs
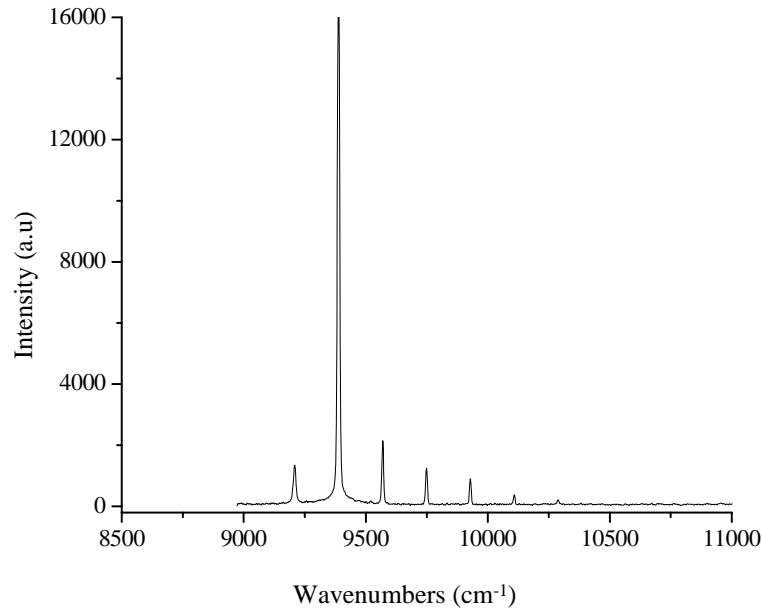
Fig. 52. Cascading anti-Stokes process due to FWM and SRS in D_2 at 300 Torr for a 1064 nm pump pulse energy of 240 mJ/pulse. Stokes cascading behavior is not shown here due to limited range of spectrometer.

.

at high pressure and high field intensities is gas breakdown due to efficient UV generation, which is observed during experiment. In order to avoid these side effects, we choosed to work at somewhat lower pressures of 300 Torr and lower pump pulse energies corresponding to threshold of forward rotational SRS process.

As mentioned in the brief introduction of this chapter, we have investigated the temporal, spatial, and angular beam overlaps, on both rotational and vibrational generation efficiency and transverse beam quality. We observed that for particular conditions of detuning, fixed pressure, and given energies of driving fields, rotational generation completely disappears. Therefore, as a first step we choose to investigate detuning dependence of rotational generation at a pressure of 300 Torr and energies corresponding to 8 mJ/pulse (807 nm laser), and 150 mJ/pulse (1064 nm laser).
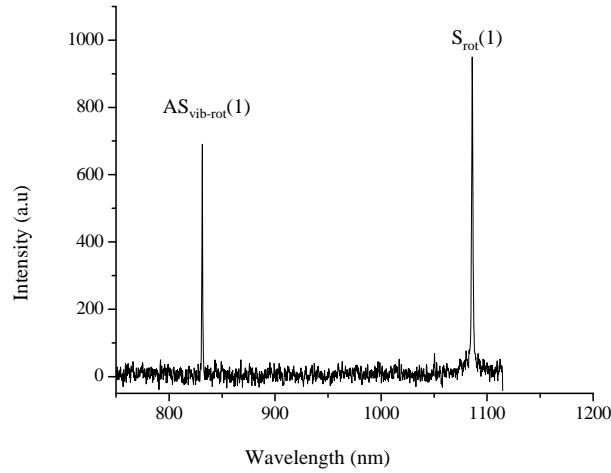
Fig. 53. Rotational Stokes $S(1)$ 1084 nm and rotational vibrational anti-Stokes $AS_{vib-rot}(1)$ 830 nm in the backward direction at a 749 Torr pressure and 220 mJ/pulse 1064 pump energy. Due to the FWM process, 1.6 μm rotational vibrational Stokes should also be present in the backward direction. This is not observed due to limited range of our spectrometer.

Measurement procedure is described below: at the output of the cell, a 1000 mm IR coated lens is used to focus the dispersed spectrum and project it onto a white screen placed at 3 m away from the exit window of the cell. The lens was slightly tilted in order to send a small reflection backwards to an aluminum foil where the fiber spectrometer was directed to. Due to different divergences of driving fields, main portion of 1064 beam was hitting the foil at a different angle than weaker 807 nm beam, and thus is displayed as attenuated beam on all following spectra. Aluminum foil was chosen instead of white paper because of better sensitivity to the ultraviolet beams. Spectrum was measured with a high resolution spectrometer equipped with 3648-element CCD-array detector with a detection range 200 nm-1100 nm. Each data point corresponds to an integration time of 3 s, and therefore represents the average of 30 shots.
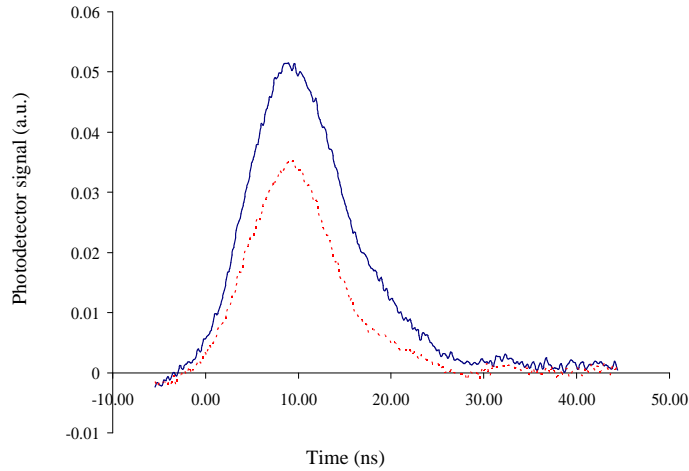
Fig. 54. Depletion of pump pulse in the forward direction as measured by a photode-
tector. This depletion coincides with suppression of forward and backward
SRS. Continuous line shows the temporal pump pulse profile during SRS pro-
cess, while dashed line indicates depleted pump.

The position of vibrational Raman resonance was established by measuring the small anti-Stokes gain of 650 nm beam at two different pressures with driving fields attenuated such that only red 650 nm beam is present.

We present in Figs.55 and 56 the two curves corresponding to 650 nm signal as measured by a fast photodector. The first measurement was taken at a pressure of 84 Torr and energies of driving fields 18 mJ/pulse (1064 nm) and 1.1 mJ/ pulse attenuated 807 nm beam. Solid continuous line indicates the lorentzian fit $y = y_0 + \frac{2A}{\pi} \frac{w}{\left(4(x-x_c)^2+w^2\right)}$ with fitting parameters $y_0 = 0.92, x_c = 807.21077, w = 0.00045, A = 0.00267$. Therefore, Raman resonance for this pressure was determined to correspond to a Ti:Sapphire wavelength of 807.2108 nm and is indicated as zero on the graph. Detunings are shown by keeping the convention that positive values correspond to longer Ti:sapphire wavelengths. The second Raman resonance was measured in a similar fashion, this time at a pressure of 170 Torr, with same energies of driving
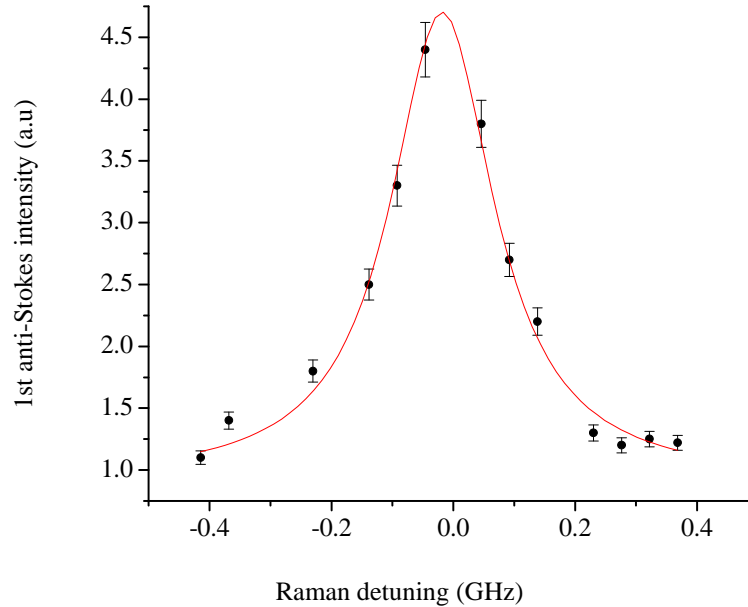
Fig. 55. First anti-Stokes 650 nm gain as a function of Raman detuning in deuterium at a pressure 84 Torr. Energies of driving fields were 18 mJ/pulse for 1064 nm beam, while 807 nm energy was attenuated to 1.1 mJ/pulse. Raman resonance was determined to be 807.2108 nm for the lorentzian fit $y = y_0 + \frac{2A}{\pi} \frac{w}{\left(4(x-x_c)^2 + w^2\right)}$ shown by continuous line. Here fitting parameters are $y_0 = 0.92, x_c = 807.21077, w = 0.00045, A = 0.00267$. Error bars correspond to 5% of data.

fields as in previous measurements. For this measurement the onset of generation of second anti-Stokes at 533 nm distorts a little bit the gain measurement. However, as indicated in Ref. [22], the generation is supposed to drop at Raman resonance, which was inferred to be 807.2113 nm. The linear shift of Raman resonance with pressure was determined then by extrapolation and used to calculate the Raman resonance at 300 pressure corresponding to a Ti:Sapphire wavelength of 807.2125 nm.

All spectra were taken while monitoring and recording the power transmitted through the cell and acoustic signal from a microphone placed inside the cell and connected to an oscilloscope. These two measurements represent an indication of
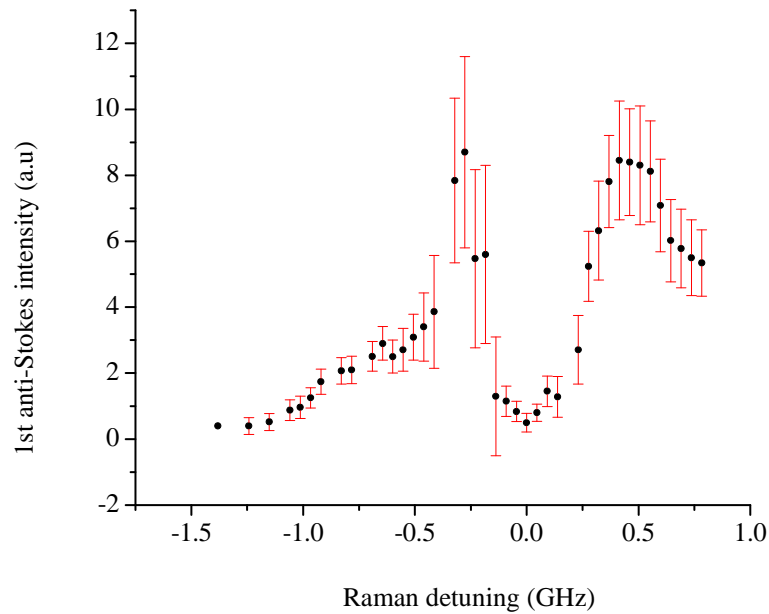
Fig. 56. First anti-Stokes 650 nm gain as a function of Raman detuning in deuterium at a pressure 170 Torr. Energies of driving fields were 18 mJ/pulse for 1064 nm beam, while 807 nm energy was attenuated to 1.1 mJ/pulse. Raman resonance was determined to be 807.2113 nm. Error bars correspond to 5% of data.

adiabatic behavior of the Raman process, as described also in Ref [22]. If the ensemble of molecules is prepared adiabatically into a single eigenstate which corresponds to an initial state in which all population is in the ground state, then we expect that after pulses are gone, all molecules return to ground state, meaning no energy is left in the system.
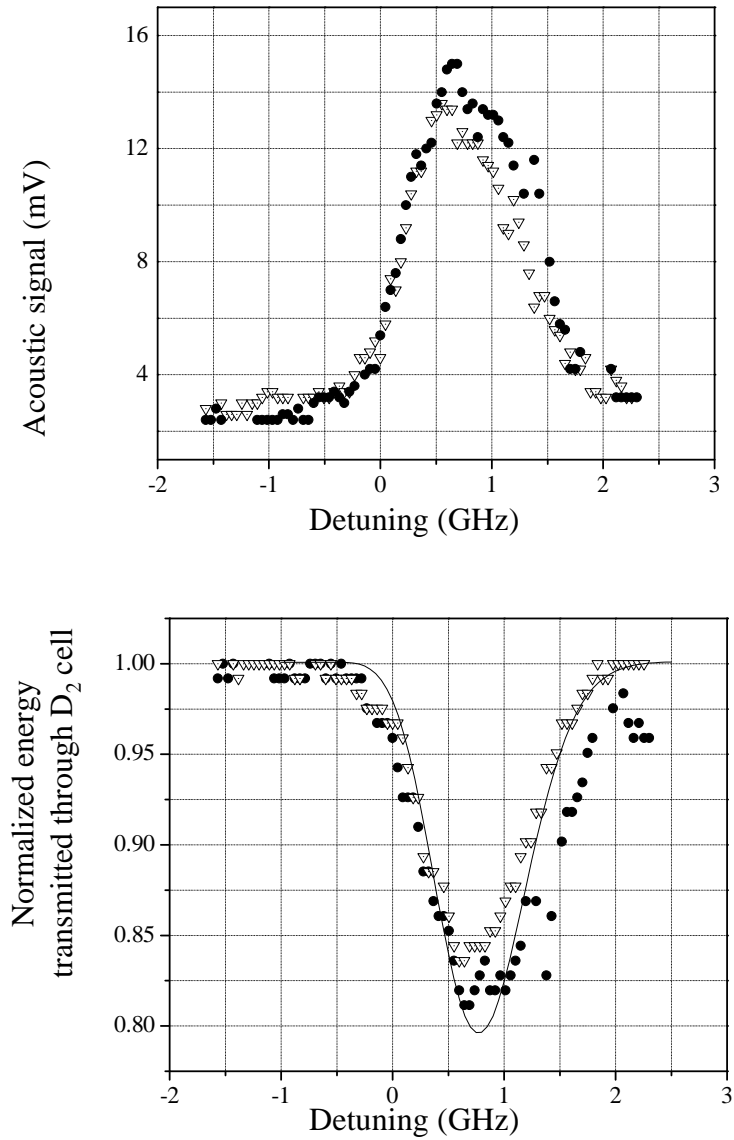
Fig. 57. Acoustic signal measured by a microphone placed inside the cell as a function of detuning (top figure). Normalized power transmitted through D₂ cell as measured by powermeter as a function of detuning from Raman resonance (bottom). Data was normalized to the power transmitted at large detunings. Filled circles data points correspond to first scan, while triangle points indicate a second scan taken at a later time. The continuous line indicates the calculated population of ground state 25 ns after pulses are gone.

Close to Raman resonance, the adiabaticity condition is not satisfied, and some of driving field energy will be absorbed by molecules, effectively exciting them to some states. To verify that indeed this energy is left in molecules, a microphone was placed inside of cell. The absorption of driving field energies by molecules was followed quickly by a relaxation process with strong shock waves as indicated by the microphone signal. These two measurements are shown in Fig. 57.

We observed that the dip in the transmitted energy is shifted from the Raman resonance due to different Stark shifts of ground and excited vibrational states. As it was pointed out in Ref. [96] the magnitude of the optical Stark effect on molecular vibrational - rotational frequencies (i. e. frequency shift of transition in the presence of nonresonant optical field) is proportional to the applied laser intensities. We performed a numerical simulation of population dynamics of ground state by solving time dependent Schrödinger equation with gaussian pulses of intensities 4.5 GW/cm^2 for Nd:Yag laser and 0.3 GW/cm^2 for 807 nm laser. We assume that 1084 nm SRS line is also present in the system, effectively driving the rotational transition together with 1064 laser and that its intensity is 1% of pump intensity. Pulse durations of applied fields were taken to be 2 ns FWHM for 807 nm laser, and 4 ns FWHM for 1064 and 1084 beams. The time dependent Schrödinger equation was solved with initial condition that all population is in the ground state. The results are indicated in Fig. 57(bottom) by the solid line.

We proceed to describe now the results of our scanning across Raman resonance in order to determine the conditions corresponding to enhancement, and suppression of rotational generation. To illustrate these two particular cases, we present two spectra, together with their corresponding pictures. First case, presented in Fig. 58 shows a pure vibrational comb, while Fig. 59 shows the rotational generation superimposed onto vibrational comb. The only difference between the two cases is
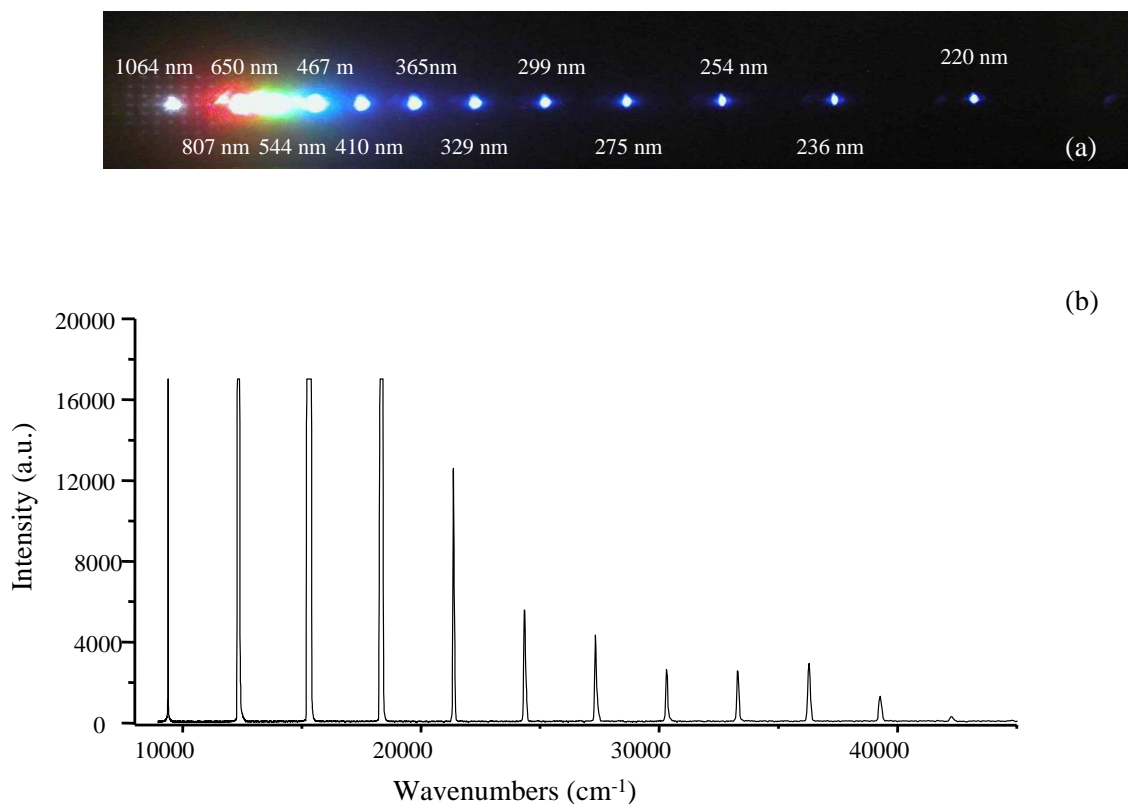
Fig. 58. Vibrational comb at 300 Torr pressure and 0 GHz detuning. (a) represents a picture taken with a digital camera of the dispersed spectrum, while (b) illustrates the same spectrum as recorded by spectrometer.

the detuning from Raman resonance (exact resonance in the first case, and 1.15 GHz positive detuning in the second case). Intensities of rotational Stokes and anti-Stokes in the vicinity of 1064 nm laser were monitored together with intensities of all other rotational and vibrational lines as the detuning from Raman resonance was changed.

These dependencies are shown in Fig. 60 top (rotational) and bottom (vibrational). Here the intensities of first rotational Stokes 1088 nm are represented by crosses, anti-Stokes 1044 nm by triangles and Ti:Sapphire first rotational anti-Stokes 795 nm by filled circles. Data was corrected for the background noise and intensities of Nd:YAG rotational Stokes and anti-Stokes multiplied by a factor of 25, for an
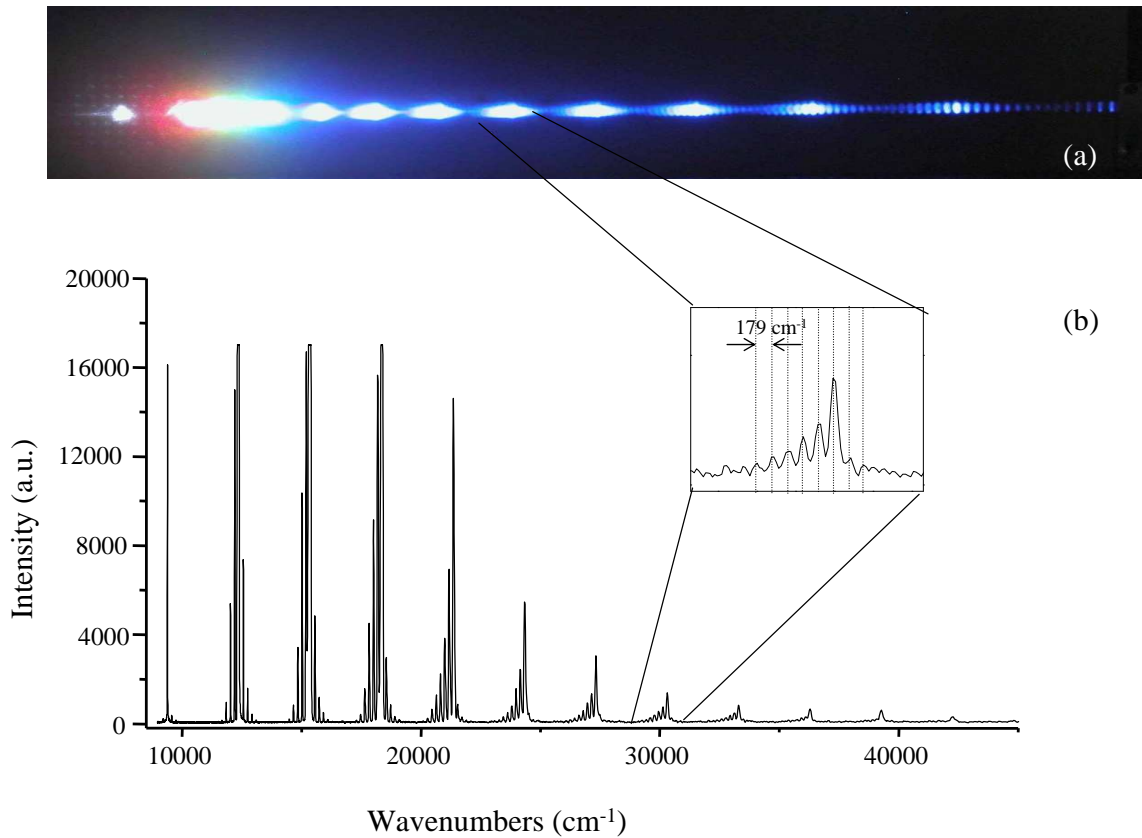
Fig. 59. Vibrational rotational comb at 300 Torr pressure and 1.15 GHz detuning. (a) represents a picture taken with a digital camera of the dispersed spectrum, while (b) illustrates the same spectrum as recorded by spectrometer. The insert shows the rotational comb spaced by 179 cm^{-1}.

easier comparison with intensity of Ti:Sapphire rotational anti-Stokes. Bottom figure indicates the Nd:YAG laser intensity (triangle points), Ti:sapphire (star filled points), blue 410 nm vibrational line (cross points), UV 366 nm vibrational line (filled circles). Intensities of driving fields are not saturated and shifted up by a factor of 40 for a better rendering. All other vibrational lines in the spectrum were saturated, and not presented in this picture.

The behavior of vibrational lines as a function of detuning is exactly as expected and observed for example in [22]. For negative detunings vibrational generation is

less efficient than for positive detunings, where it actually maximizes. On-resonance generation, is overall less efficient than off-resonance one [22]. A dip is observed at the Raman resonance, with a clear increase on the positive side of detunings. Overall, the shape indicated by vibrational line intensities resembles previous experimental data [22], but in our case this line shape is more sensitive to the nonadiabatic effects due to a larger laser line-width than previously employed. Figure 61 indicates percentage increase or decrease of driving fields as a function of detuning. Top figure indicates the change in Ti:Sapphire intensity as detuning is changed, while bottom figure shows the change in Nd:YAG laser intensity.

Rotational lines show same kind of behavior as vibrational ones. Close to Raman resonance, suppression of rotational Stokes anti-Stokes around 1064 indicate that rotational and vibrational generation processes are interconnected. A large dip that peaks off resonance is observed in the intensity of 1064 nm pump, which cannot explain the increase in the rotational Stokes and antiStokes corresponding to 1044 and 1084 nm beam. Correspondingly, the energy of 807 drops on Raman resonance and cannot be responsible for this enhancement.

Altough we are not certain which mechanism is exactly responsible for the enhancement and supression of rotational lines as Raman detuning is changed, there are several possibilities that may play a role.

As mentioned in the introduction, gain suppression was observed if phase matching conditions were met. As detuning is changed from negative to positive, refractive index of for example central sidebands increases by a factor of four [22]. We actually observed that simply changing the focusing of Nd:YAG laser, in particular its divergence, results in suppression of rotational gain even at large pump intensities and large gas pressure.
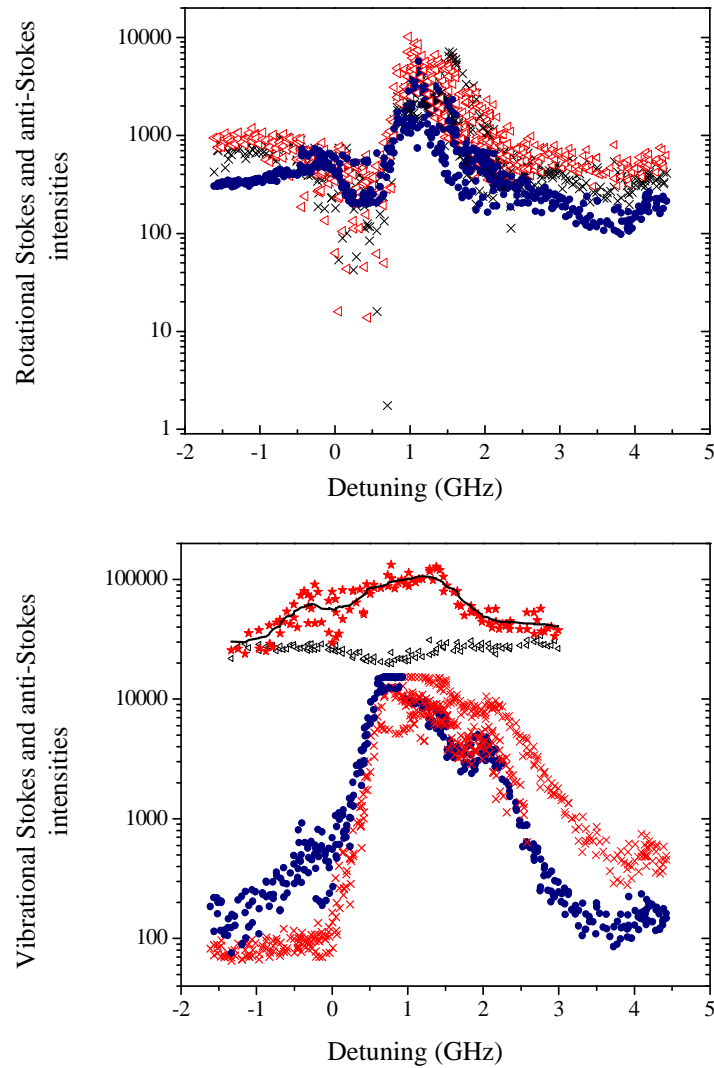
Fig. 60. Top figure indicates the intensities of Nd:Yag first rotational Stokes 1088 nm (cross points), anti-Stokes 1044 nm (triangle) and Ti:Sapphire first rotational anti-Stokes (filled circles) 795 nm as a function of detuning. Measurements were taken with HR 4000 spectrometer, with background noise subtracted from raw data, and intensities of Nd:Yag rotational Stokes and anti-Stokes multiplied by a factor of 25 for a better visualization of their behavior. Bottom figure indicates the Nd:YAG laser intensity (triangle points), Ti:Sapphire (star filled points), blue 410 nm vibrational line (cross points), UV 366 nm vibrational line (filled circles). Continuous line represents 15 point smoothing curve of Ti:Sapphire data points. Intensities of driving fields are not saturated and shifted up for a better visualization.
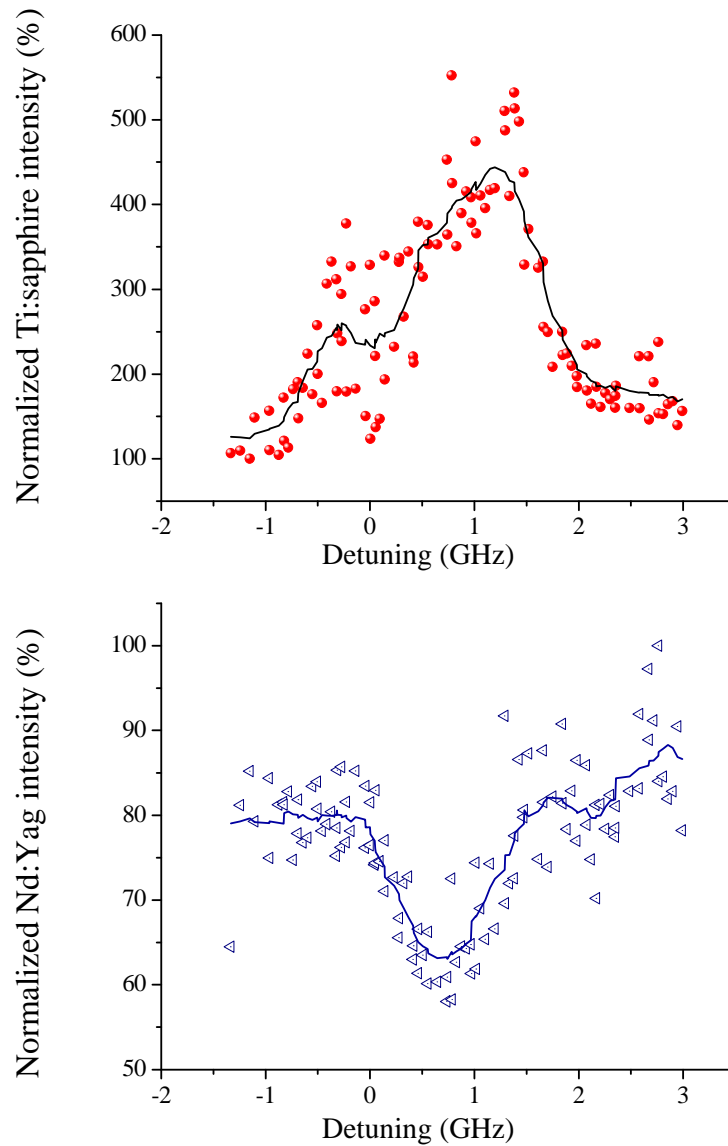
Fig. 61. Top figure indicates percentage increase in intensity of Ti:sapphire driving field as a function of detuning. Normalization is done with respect to initial intensity in absence of second driving field. Bottom figure indicates percentage decrease of Nd:YAG as a function of detuning. Both continuous lines represent 15 point smoothing of raw data.

Another possibility could be Raman self-focusing [97]. This kind of self-focusing occurs when two lasers drive a Raman transition with a frequency difference slightly different than Raman resonance frequency. If the prepared coherence reaches its maximum value of 0.5, then changes in refractive index result in changes of beam propagation, and therefore occurrence of self-focusing and defocusing. Experimental results using the rotational transition $S_1(0)$ in hydrogen [97] demonstrated that self focusing occurs at 0.6 GHz from Raman resonance, with a beam size changing by as much as 40% from antiphased to phased state. This self-focusing could reduce the gain of SRS, thus increasing the efficiency of rotational generation. As shown in the same experimental work [97], defocusing occurs at very small negative detuning from Raman resonance, and may contribute to the suppression of rotational lines.

D.   Conclusions

We have observed simultaneous rotational and vibrational Raman generation in deuterium gas, with only two laser pulses applied at the input of the molecular cell. Only the fundamental vibrational transition $Q_1(0)$ is driven strongly in this experiment. However, in addition to efficient vibrational Raman generation we observe generation of a large number of rotational sidebands corresponding to $S_0(0)$ transition. When detuning from Raman resonance is changed, either enhancement of rotational generation is observed (on both positive and negative detunings, but with a strong increase for positive detunings) or complete suppression. Phase matching, Raman self-focusing could play a role in the generation of rotational and vibrational combs, which were proven to be interconnected. The increase in spectral density of one order of magnitude could be used to extend the capabilities of pulse shaping.

CHAPTER VII

EIT IN MOLECULAR RAMAN DRIVEN SYSTEM

A.   Introduction

Electromagnetically induced transparency EIT has been the subject of numerous investigations due to its potentially large number of applications: from ultraslow light [98], laser cooling [99], nonlinear optics [31] to light storage [100]. EIT is essentially a phenomenon that occurs when, in a medium, the absorption of a probe laser light driving a particular transition in atoms or molecules is cancelled by turning on a second coupling field that is tuned to a neighboring transition. EIT has been demonstrated so far mostly in atoms, and only very recent experiments have shown that EIT is possible in a molecular system [33]. To our knowledge, no work has been done on studying interference effects in a molecular Raman system.

B.   Theoretical description

In our theoretical proposal, we show that EIT based ideas such as interference effects can be used to control the molecular motion in a Raman gas medium, with further implications such as selectivity of different degrees of freedom in such Raman driven system.

We begin by describing our system in Fig. 62. Two pairs of laser fields Ω_{p1}, Ω_{c2}, and Ω_{p2}, Ω_{c2} drive two Raman transitions in a molecular sytem. Here Ω indicates the Rabi frequency given by $\Omega = \frac{E\mu}{2\hbar}$, where E represents the electric field, and μ dipole moment. For a better understanding, let us assume that transition $a \rightarrow c$ corresponds to ro- vibrational Raman transition $v'' = 0, J'' = 0 \rightarrow v' = 1, J' = 2$ in molecular deuterium, while $b \rightarrow c$ represents pure vibrational transition $v'' = 0, J'' = 2 \rightarrow v' =$
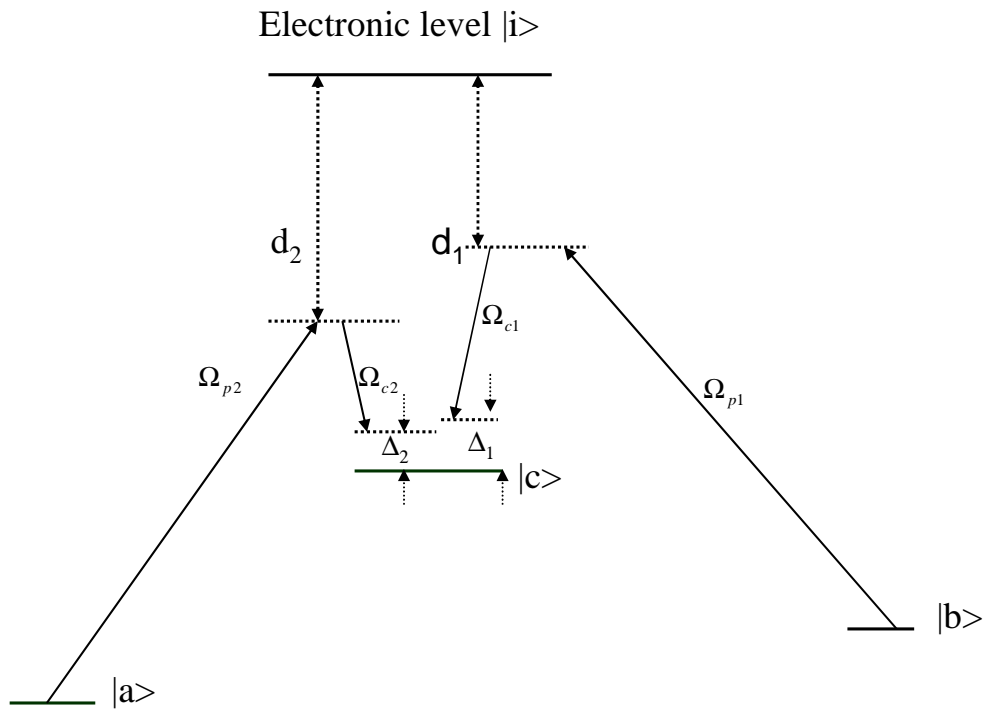
Fig. 62. Energy level schematic for establishing coherences ρ_{ac} and ρ_{bc}. Driving fields Ω_{p1}, Ω_{c1} are applied in such a way to drive $b \to c$ Raman transition in a molecular system, while transition $a \to c$ is driven by Ω_{p2}, Ω_{c2}. One photon detunings from electronic state $|i\rangle$ are indicated by d_1 and d_2 and large compared to two photon detunings indicated by Δ_1 and Δ_2

$1, J' = 2$.

For simplicity of our derivation, we assume that only one electronic state $|i\rangle$ is present in our system. Inclusion of all other electronic levels can be done without affecting our results, but the physics of the problem can be rendered and understood easier in the simpler case presented here. The hamiltonian of such a system is given in the dipole approximation by:

$$H = H_0 + H_{\text{int}}, \tag{7.1}$$

where hamiltonian H_0 is defined by:

$$H_0 = \hbar\omega_a \left|a\right\rangle \left\langle a\right| + \hbar\omega_b \left|b\right\rangle \left\langle b\right| + \hbar\omega_c \left|c\right\rangle \left\langle c\right| + \hbar\omega_i \left|i\right\rangle \left\langle i\right| \tag{7.2}$$

The interaction hamiltonian assumes the form:

$$
\begin{aligned}
H_{\mathrm{int}} = {} & 2\hbar\left[\Omega_{p2}\left(t\right)Cos\left(\omega_{p2}t\right)\left|a\right\rangle \left\langle i\right| + \Omega_{p1}\left(t\right)Cos\left(\omega_{p1}t\right)\left|b\right\rangle \left\langle i\right| + \right.\\
& \left. + \Omega_{c1}\left(t\right)Cos\left(\omega_{c1}t\right)\left|c\right\rangle \left\langle i\right| + \Omega_{c2}\left(t\right)Cos\left(\omega_{c2}t\right)\left|c\right\rangle \left\langle i\right|\right] + c.c
\end{aligned}
\tag{7.3}
$$

Frequencies of driving fields are defined in terms of detunings as: $\omega_{p1} = \omega_i - \omega_b - d_1$; $\omega_{p2} = \omega_i - \omega_a - d_2$; $\omega_{c1} = \omega_{p1} - \left(\omega_c - \omega_b + \Delta_1\right)$, and $\omega_{c2} = \omega_{p2} - \left(\omega_c - \omega_a + \Delta_2\right)$.

Following [21] and [36], we assume that one photon detunings from electronic level $\left|i\right\rangle$ are large compared to Rabi frequencies (d_1, d_2 approximately four orders of magnitude larger that effective Rabi frequencies), which implies that the probability amplitudes of electronic states are small compared to these one-photon detunings. In addition, decay of upper electronic states is negligible. After a unitary transformation of initial Hamiltonian in rotating frame of reference given by :

$$
U = \begin{pmatrix}
e^{it\omega_a} & 0 & 0 & 0 \\
0 & e^{it(\omega_a - \Delta_1 - \Delta_2)} & 0 & 0 \\
0 & 0 & e^{it(\omega_c + \Delta_2)} & 0 \\
0 & 0 & 0 & e^{it(-d_1 - d_2 + \omega_i)}
\end{pmatrix},
\tag{7.4}
$$

we obtain the following 3 X 3 effective Hamiltonian :

$$
H_{eff} = -\hbar \begin{pmatrix}
\frac{\Omega_{p2}^2(t)}{(d_1+d_2)} & 0 & \frac{\Omega_{c2}(t)\Omega_{p2}(t)}{(d_1+d_2)} \\
0 & \Delta_1 - \Delta_2 - \frac{\Omega_{p1}^2(t)}{(d_1+d_2)} & \frac{\Omega_{c1}(t)\Omega_{p1}(t)}{(d_1+d_2)} \\
\frac{\Omega_{c2}(t)\Omega_{p2}()}{(d_1+d_2)} & \frac{\Omega_{c1}(t)\Omega_{p1}(t)}{(d_1+d_2)} & \Delta_2 + \frac{\Omega_{c1}^2(t)+\Omega_{c2}^2(t)}{(d_1+d_2)}
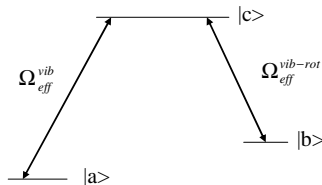\end{pmatrix}
\tag{7.5}
$$

Fig. 63. The Raman driven system by two pairs of fields can be reduced to a standard EIT *Lambda* scheme driven by two effective fields. Transition $a \rightarrow c$ corresponds to ro- vibrational Raman transition, while $b \rightarrow c$ represents a pure vibrational Raman transition.

The effective 3 X 3 Hamiltonian describes essentially a standard EIT *Lambda* scheme driven by two effective fields as shown in Fig. 63. However, depending on the initial choice of driving fields, one can realize a V or *Ladder* type of scheme.

Molecular modulation technique involves adiabatic preparation of molecular ensemble, in other words the evolution of Raman system follows a state that evolves smoothly from ground state $|a\rangle$. We are choosing to solve time dependent Schrödinger equation that satisfies the condition that all population initially is found in ground state. We are assuming gaussian pulses with FWHM of 4 nanoseconds for Ω_{p1}, Ω_{c1}, Ω_{p2} and 1 nanosecond for second coupling field Ω_{c2}, and values of 10^{13} Hertz at time $t = 0$ (at the peak of the pulse). Sum of one photon detunings $d_1 + d_2$ is taken to be equal to 10^{15} Hertz.

Dynamics of populations of each state is presented in Fig. 65. Both transitions are driven on exact resonance, with two-photon detunings Δ_1 and Δ_2 equal to zero. Time $t = 0$ corresponds to the peak intensity of applied pulses. One can see that populations of states $|a\rangle$ (continuous line) and $|b\rangle$ (small dashed line) reach a value of 0.5, corresponding to a maximum value of coherence ρ_{ab} of 0.5. Population of state $|c\rangle$ is virtually zero before and during the time that pulses are applied, and therefore is essentially decoupled from the rest of the system. Population of state $|a\rangle$ returns to
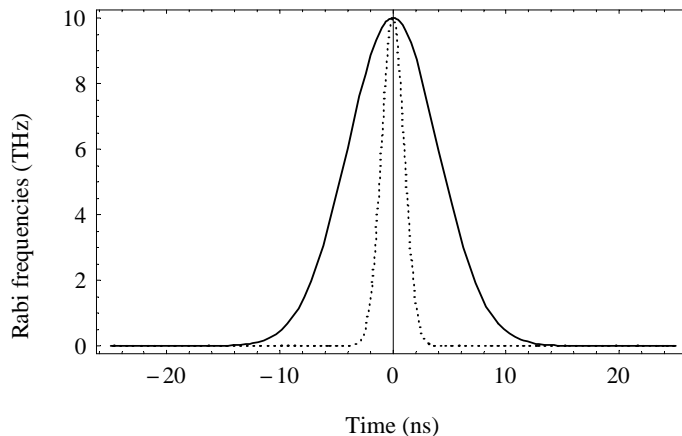
Fig. 64. Time dependent Rabi frequencies of the applied fields. Pulse shapes are assumed to be gaussian, with corresponding values of 10^{13} Hz at time $t = 0$. Three of the applied fields are identical Ω_{p1}, Ω_{c1}, Ω_{p2} with a FWHM of 4 nanosecond and represented by continuous line. Coupling field 2 (dashed line) Ω_{c2} has FWHM of 1 nanosecond.

its maximum value of 1 after pulses are gone, indicating that adiabaticity condition is clearly satisfied.

Decoupling of state $|c\rangle$ reduces to cancellation of driven ro-vibrational transition, and enhancement of pure rotational transition, with a maximum established coherence of 0.5 (Fig. 66). Changing second coupling field intensity Ω_{c2} with all applied fields on resonance affects only the efficiency of pure rotational Raman generation i.e. the value of coherence ρ_{ab} that can be established in the system. Increasing Ω_{c2} results in an increase of established rotational coherence ρ_{ab} up to its maximum value, followed by a slow decrease, as shown in Fig.67. Corresponding populations of all states are illustrated in Fig. 68.
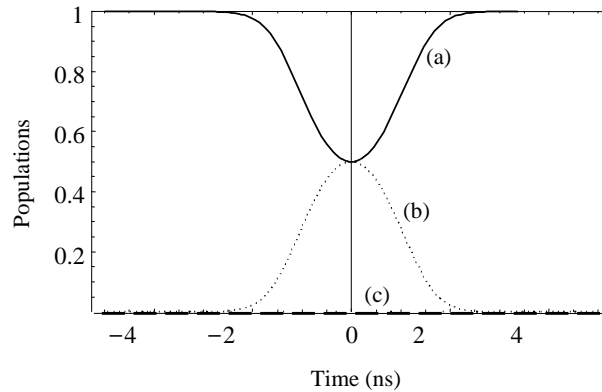
Fig. 65. Population dynamics during the time that pulses are applied. At peak pulse intensity corresponding to time $t = 0$, population of state $|a\rangle$ (continuous line indicated in (a)) reaches 0.5 value. Population in state $|b\rangle$ (small dashed line in (b))increases from a zero initial value to a 0.5 value at time $t = 0$. Population of state $|c\rangle$ is virtually zero before and during the time that pulses are applied.

C. Conclusion

In summary, we have shown that interference effects can take place within different rotational vibrational driven transitions in molecules. These interference effects do not result here in change of transmission of fields as in the standard EIT scheme, because our system does not exhibit absorption, but rather result in control of molecular motion for example switching from vibrational rotational motion to pure rotational.
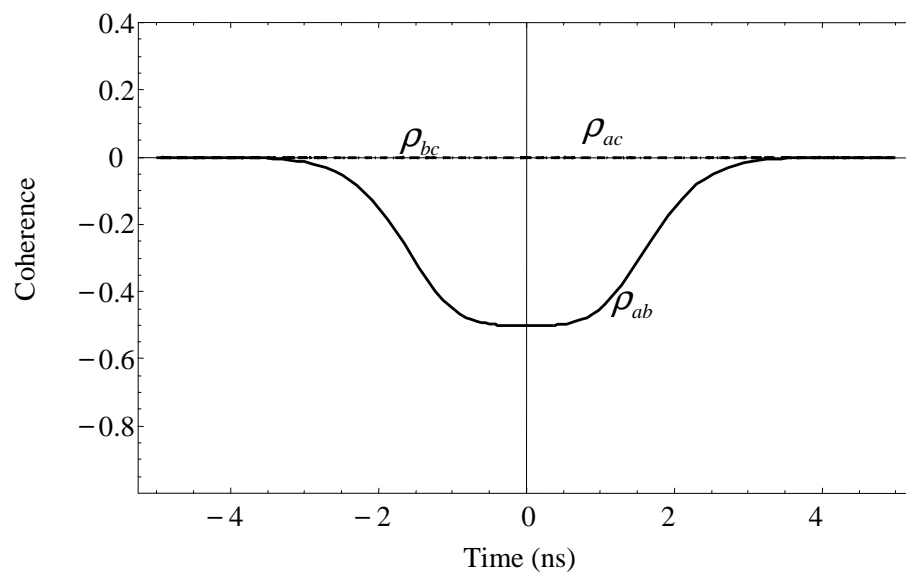
Fig. 66. Dynamics of Raman coherences with all fields on resonance and of equal Rabi frequencies. Coherence ρ_{ab} is maximum, while no coherence is established between initially driven transitions ρ_{ac} and ρ_{bc}.
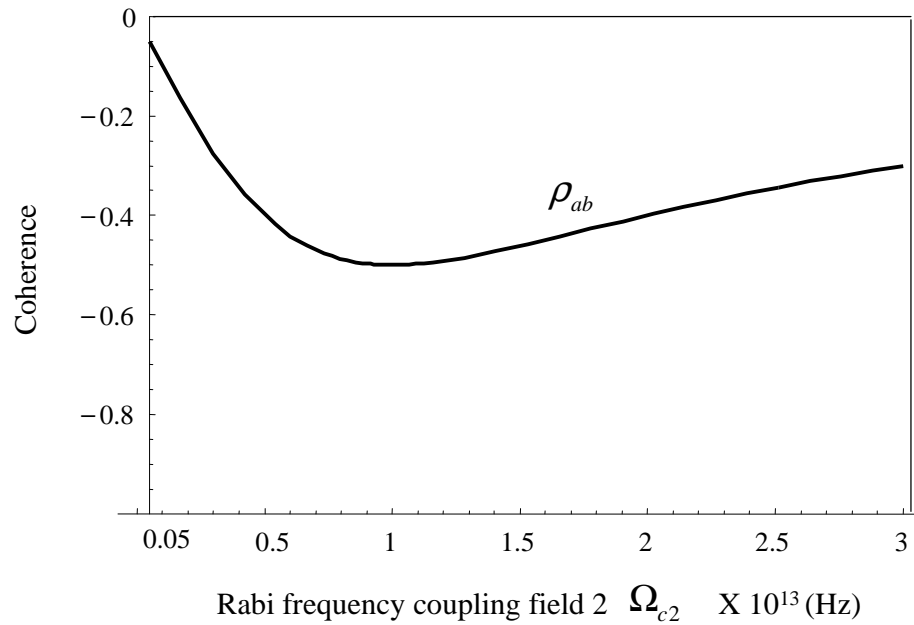
Fig. 67. Increasing Ω_{c2} results in an increase of established rotational coherence ρ_{ab} up to its maximum value, followed by a slow decrease. As pointed out in Ref. [22], efficient Raman generation requires maximization of established coherence. By keeping fields resonant with all transitions, and at the same time varying the strength of second coupling field Ω_{c2}, we will be able to change (enhance) the efficiency of rotational Raman generation.
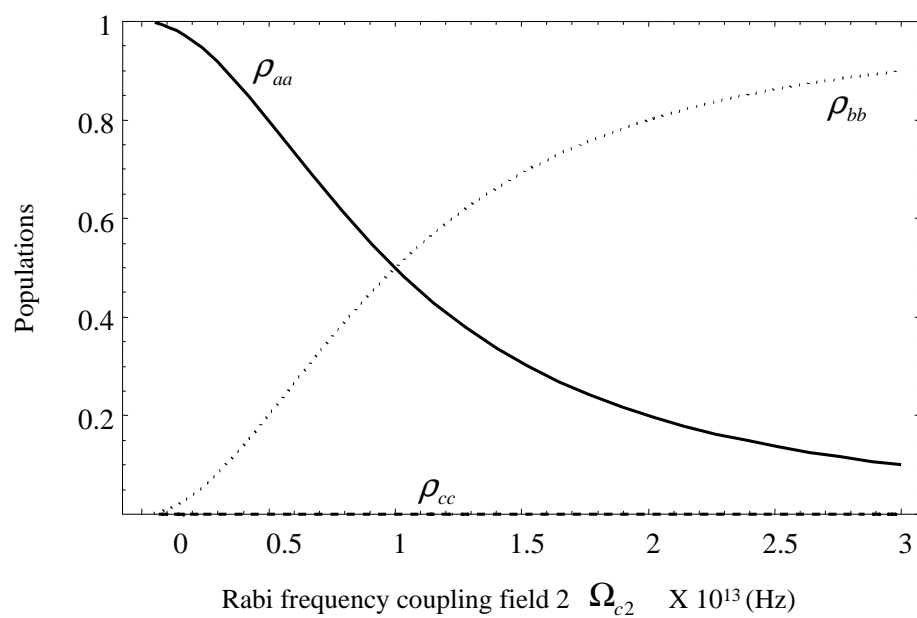
Fig. 68. Change in the populations of levels a and b as a function of Rabi field frequency Ω_{c2}. Fields are resonant with driven transitions.

CHAPTER VIII

CONCLUSION

The generation of reproducible attosecond pulses is an exciting goal in itself. In this dissertation, we have investigated from both theoretical and experimental point of view, methods that will allow improving one of the two main schemes of obtaining such ultrashort pulse: molecular modulation technique.

In a theoretical proposal called Raman additive technique, we have suggested a method that will allow (with a proper phase stabilization of generated sidebands) to obtain reproducible waveforms of arbitrary shape. An exciting range of possibilities could open up - not only for absolute phase control or sub-cycle shape control, but also for investigation of multiphoton ionization rates as a function of the sub- cycle shape.

We elaborated on the later subject in another theoretical project, where we exploited the unique features of such ultrasort laser pulses to be synchronized with molecular motion (rotational or vibrational) in order to investigate photoionization of molecules. We have found that different ionization rates can be achieved, simply by changing the delay time between the arrival of pulses and molecular motion, proving in effect the sensitivity of ionization process in molecules to the laser pulse shape.

From experimental point of view, improvements in the construction of driving lasers lead to establishment of larger molecular coherences at higher operating pressure than in previous experiments. This resulted in simultaneous driving of rotational and vibrational transitions with only two fields applied, in an experiment identical with previous work. As mentioned before, increase of spectral density of generated comb, keeping the same bandwidth represents the next step towards a better control of electric field under the envelope.

In another experimental proposal using rotational transition in deuterium we have shown that employing a hollow waveguide instead of normal Raman cell improves the efficiency of the generation process. By optimizing gas pressure and waveguide geometry to compensate the GVD, the method can be extended to efficiently generate Raman sidebands at a much lower energy of driving fields than previously employed.

In the last part of this dissertation, we have investigated theoretically a particularly exciting possibility for controlling the molecular motion in a Raman driven system. Based on interference effects (EIT like) that will take place inside of a molecule, selective excitation of different degrees of freedom can be achieved (for example switching from ro- vibrational motion to pure rotational). This last idea will be investigated experimentally in the near future.

REFERENCES

[1] A. L. Schawlow and C. H. Townes, Phys. Rev. **112**, 1940 (1958).

[2] T. H. Maiman, Nature **187**, 493 (1960).

[3] R. W. Hellwarth, Bull. Am. Phys. Soc. **6**, 414 (1961).

[4] A. J. D. Maria, Appl. Phys. Lett. **12**, 483 (1966).

[5] C. V. Shank and E. P. Ippen, Appl. Phys. Lett. **24**, 273 (1974).

[6] A. Siegman, *Lasers* (University Science Books, Mill Valley, CA, 1986).

[7] O. Svelto, *Principles of Lasers* (Plenum Press, New York, 1989).

[8] J.D.Simon, Rev. Sci. Instrum. **60**, 3597 (1989).

[9] A. Yariv, *Quantum Electronics* (Wiley, New York, 1975).

[10] D. von der Linde, Appl. Phys. **2**, 281 (1983).

[11] D. Spence, P. N. Kean, and W. Sibett, Opt. Lett. **16**, 42 (1991).

[12] K.F.Wall, R. L. Aggarwal, R. E. Fahey, and A. J. Strauss, IEEE J. of Quant. Electr. **24**, 1016 (1988).

[13] G. Steinmeyer, D. H. Sutter, L. Gallmann, N. Matuschek, and U. Keller, Science **286**, 1507 (1999).

[14] T. W. Hänsh, Opt. Commun. **80**, 70 (1990).

[15] S. E. Harris, Opt. Commun. **100**, 487 (1993).

[16] Z. Chang, A. Rundquist, H. Wag, M. M. Murnane, and H. C. Kapteyn, Phys. Rev. Lett. **79**, 2967 (1997).

[17] P. B. Corkum, Phys. Rev. Lett. **71**, 1994 (1993).

[18] A. Nazarkin, G. Korn, M. Wittman, and T. Elsaesser, Phys. Rev. Lett. **83**, 2560 (1999).

[19] A. E. Kaplan, Phys. Rev. Lett. **73**, 1243 (1994).

[20] S. E. Harris, Opt. Lett. **19**, 2018 (1994).

[21] S. E. Harris and A. V. Sokolov, Phys. Rev. A **55**, R4019 (1997).

[22] A. V. Sokolov and S. E. Harris, J. Opt. B **5**, R1 (2003).

[23] D. D. Yavuz, D. R. Walker, , G. Y. Yin, and S. E. Harris, Opt. Lett. **27**, 769 (2002).

[24] A. V. Sokolov, D. R. Walker, D. D. Yavuz, G. Y. Yin, and S. E. Harris, Phys. Rev. Lett. **85**, 562 (2000).

[25] J. Wu and H. Zheng, Phys. Rev. A **68**, 015802 (2003).

[26] H. R. Telle, G. Steinmeyer, A. E. Dunlop, J. Stenger, D. H. Sutter, and U. Keller, Appl. Phys. B **69**, 327 (1999).

[27] D. J. Jones, S. A. Diddams, J. K. Ranka, A. Stentz, R. S. Windeler, J. L. Hall, and S. T. Cundiff, Science **288**, 635 (2000).

[28] A. Apolonski, A. Poppe., G. Tempea, Ch.Spielmann, T. Udem, R. Holtzwarth, T. W. Hansch, and F. Krausz, Phys. Rev. Lett. **85**, 740 (2000).

[29] G. G. Paulus, F. Grasbon, H. Walter, P. Villoresi, M. Nisoli, S. Stagira, E. Priori, and S. DeSilvestri, Nature **414**, 182 (2001).

[30] S. E. Harris and A. V. Sokolov, Phys. Rev. Lett. **81**, 2894 (1998).

[31] M. Jain, H. Xia, G. Y. Yin, A. J. Merriam, and S. E. Harris, Phys. Rev. Lett. **77**, 4326 (1996).

[32] D. D. Yavuz, D. R. Walker, M. Y. Shverdin, G. Yin, and S. E. Harris, Phys. Rev. Lett. **91**, 23602 (2003).

[33] F. Benabid, P. Light, F. County, and P. S. J. Russell, Opt. Express **13**, 5694 (2005).

[34] A. M. Burzo and A. V. Sokolov, J. Modern Opt. **51**, 2665 (2004).

[35] A. V. Sokolov, D. D. Yavuz, and S. E. Harris, Opt. Lett. **24**, 557 (1999).

[36] F. L. Kien, J. Q. Liang, M. Katsuragawa, K. Ohtsuki, K. Hakuta, and A. V. Sokolov, Phys. Rev. A **60**, 1562 (1999).

[37] A. V. Sokolov, Opt. Lett. **24**, 1248 (1999).

[38] T. Baumert, T. Brixner, V. Seyfried, M. Strehle, and G. Gerber, Apply. Phys. B **65**, 779 (1997).

[39] C. W. Hillegas, J. X. Tull, D. Goswami, D. Strickland, and S. D. Warren, Opt. Lett. **19**, 2018 (1994).

[40] A. M. Weiner, Prog. Quant. Electr. **19**, 161 (1995).

[41] W. E. White, F. G. Patterson, R. L. Combs, D. F. Price, and R. L. Price, Opt. Lett. **18**, 1343 (1993).

[42] B. Broers, L. D. Noordam, and H. B. L. van Heuvall, Phys. Rev. A. **46**, 2749 (1992).

[43] W. S. Lee, T. B. Morris, A. Maslov, D. S. Citrin, J. Prineas, G. Khitrova, and H. M. Gibbs, Apply. Phys. Lett. **78**, 3941 (2001).

[44] S. A. Rice, Science **258**, 412 (1992).

[45] A. M. Weiner, J. P.Heritage, and J. A. Salehi, Opt. Lett. **13**, 300 (1988).

[46] A. Efimov, C. Shaffer, and D. H. Reize, JOSA B. **12**, 1968 (1995).

[47] A. Baltuška, T. Udem, M. Uiberacker, M. Hentschel, E. Goulielmakis, C. Gohle, R. Holwartz, V. S. Y. A. Scrinzi, T. W. Hänsch, and F. Krausz, Nature **421**, 611 (2003).

[48] T. Udem and R. H. T. W. Hänsch, Nature **416**, 233 (2002).

[49] A. V. Sokolov, D. R. Walker, D. D. Yavuz, G. Y. Yin, and S. E. Harris, Phys. Rev. Lett. **87**, 033402 (2001).

[50] A. V. Sokolov, Apply. Phys. B. **77**, 343 (2003).

[51] L. Keldish, Private communication (2003).

[52] L. Keldysh, Sov. Phys. JETP **20**, 1307 (1965).

[53] D. M. Volkov, Z.Phys. **94**, 250 (1935).

[54] W. Heitler and F. London, Zeit. f. Phys. **44**, 455 (1927).

[55] F. Hund and R. S. Mulliken, Phys. Rev. **32**, 186 (1928).

[56] E. A. Hylleraas, Zeit. für Physik **71**, 739 (1931).

[57] H. James and A. Collidge, J. Chem. Phys. **1**, 823 (1933).

[58] R. F. Wallis and H. M. Hulfurt, J. Chem. Phys. **22**, 774 (1954).

[59] E. Teller and H. L. Sahlin, *Physical Chemistry: An Advanced Treatise* (Academic, New York, 1970).

[60] V. Johnson, Phys. Rev. **60**, 373 (1941).

[61] A. V. Sokolov, M. Y. Shverdin, D. R. Walker, D. D. Yavuz, A. M. Burzo, G. Y. Yin, and S. E. Harris, J. Modern Opt. **52**, 285 (2005).

[62] T. D. Raymond and A. V. Smith, Opt. Lett. **16**, 33 (1991).

[63] C. E. Hamilton, Opt. Lett. **17**, 728 (1992).

[64] A. Kasapi, G. Y. Yin, and M. Jain, Appl. Opt. **35**, 1999 (1996).

[65] T. Walther, M. P. Larsen, and E. S. Fry, Appl. Opt. **40**, 3046 (2001).

[66] M. Miyagi and S. Kawakami, Appl. Opt. **29**, 367 (1990).

[67] E. A. Marcantili and R. A. Schmeltzer, Bell Sys. Tech. J. **43**, 1783 (1964).

[68] R. K. Nubling and J. A. Harrington, Opt. Eng. **37**, 2455 (1998).

[69] A. V. Sokolov, D. D. Yavuz, D. R. Walker, G. Y. Yins, and S. E. Harris, Opt. Lett. **24**, 557 (1999).

[70] K. D. V. den Hout, P. W. Hermans, E. Mazur, and H. F. P. Knaap, Physica A **104**, 509 (1980).

[71] C. S. Wang, Phys. Rev. **182**, 482 (1969).

[72] G. Eckhardt, R. W. Hellwarth, F. J. McClung, S. E. Schwartz, D. Weiner, and E. J. Woodbury, Phys. Rev. Lett. **9**, 455 (1962).

[73] M. Geller, D. P. Bortfeld, and W. R. Sooy, Apply. Phys. Lett. **3**, 36 (1963).

[74] G. Eckhardt, D. P. Bortfeld, and M. Geller, Apply. Phys. Lett. **3**, 137 (1963).

[75] R. W. Minck, R. W. Terhune, and W. G. Rado, Apply. Phys. Lett. **3**, 181 (1963).

[76] H. Otsuka and T. Imasaka, Opt. Comm. **237**, 417 (2004).

[77] T. Imasaka, S. Kawasaki, and N. Ishibashi, Apply. Phys. B **49**, 382 (1989).

[78] T. Imasaka, T. Higashijima, S. Kawasaki, and N. Ishibashi, Apply. Phys. B **52**, 311 (1990).

[79] S. Yoshikawa and T. Imasaka, Opt. Comm. **96**, 94 (1993).

[80] S. Yoshikawa, S. Kawasaki, T. Imasaka, and N. Ishibashi, Japan. J. of Appl. Phys. **30**, L (1991).

[81] S. Kawasaki, T. Imasaka, and N. Ishibashi, Apply. Phys. B **52**, 211 (1991).

[82] L. Schoulepnikoff and V. Mitev, Pure Appl. Opt. **6**, 277 (1997).

[83] E. E. Hagenlocker, R. W. Minck, and W. G. Rado, Phys. Rev. **154**, 226 (1967).

[84] L. Galatry, Phys. Rev. **122**, 1218 (1961).

[85] R. J. Heeman and H. P. Godfried, IEEE J. Quantum Electr. **31**, 358 (1995).

[86] J. Karlsten and R. G. Wenzel, IEEE J. Quantum Electr. **19**, 1407 (1983).

[87] F. Hanson and P. Poirier, IEEE J. Quantum Electr. **29**, 2342 (1993).

[88] B. N. Perry, P. Rabinowitz, and D. S. Bomse, Opt. Lett. **10**, 146 (1985).

[89] M. R. Perrone, V. Picino, G. D. Nunzio, and V. Nassisi, IEEE J. Quantum Electr. **33**, 938 (1997).

[90] M. R. Perrone, V. Picino, G. D. Nunzio, and V. Nassisi, IEEE J. Quantum Electr. **QE 11**, 287 (1975).

[91] M. R. Perrone, V. Picino, G. D. Nunzio, and V. Nassisi, Phys. Rev. A **33**, 1788 (1986).

[92] A. Flusberg and R. Holmes, Phys. Rev. Lett. **58**, 2039 (1987).

[93] D. J. Brink, H. P. Burger, T. N. de Knock, J. A. Strauss, and D. R. Preusller, J. Phys. D : Appl. Phys. **19**, 1421 (1986).

[94] C. G. Morgan, Rep. Prog. Phys. **38**, 621 (1975).

[95] A. H. Guenther and J. R. Bettis, IEEE J. Quantum Electr. **QE 3**, 581 (1967).

[96] L. A. Rahn, R. L. Farrow, M. L. Koszykowski, and P. Mattern, Phys. Rev. Lett. **45**, 623 (1980).

[97] D. R. Walker, D. D. Yavuz, M. Y. Shverdin, G. Y. Yon, A. V. Sokolov, and S. E. Harris, Opt. Lett **27**, 2094 (2002).

[98] L. V. Hau, S. E. Harris, Z. Dutton, and C. H. Behrooozi, Nature **397**, 594 (1999).

[99] A. Aspect, E. Arimondo, R. Kaiser, N. Vansteenkiste, and C. C. Tannoudji, Phys. Rev. Lett. **61**, 826 (1988).

[100] C.Liu, Z. Dutton, C. H. Behrooozi, and L. V. Hau, Nature **409**, 490 (2001).

VITA

Andrea Mihaela Burzo was born January 18, 1972 in Cluj- Napoca, Romania. Her parents are Emil Burzo and Virginia Burzo. She graduated from " Mathematics and Physics High School Number 4", Bucharest, Romania, in 1990, and received her Bachelor's degree in Physics from the University of Bucharest, Romania, in 1995. She received her Master's degree in Condensed Matter Theoretical Physics from Texas A&M University in 2001. Her permanent mailing address is Andrei Popovici Str.No. 3, Bl. 1, Apt 13, Bucharest, Romania.

The typist for this thesis was Andrea Mihaela Burzo.